The Effects of Ethanol/Gasoline Blends on Advanced Combustion Strategies in Internal Combustion Engines

by

Mohammad Fatouraie

A dissertation submitted in partial fulfillment
of the requirements for the degree of
Doctor of Philosophy
(Mechanical Engineering)
in The University of Michigan
2014

Doctoral Committee:

Professor Margaret S. Wooldridge, Chair
Professor André L. Boehman
Professor Ilya V. Kolmanovsky
Research Scientist George A. Lavoie
Steven T. Wooldridge, Ford Motor Co.

To my beloved parents; Laya and Masoud.

Acknowledgements

First and foremost, I would like to thank my parents, who have supported me in each and every step of my life. My accomplishments could not have been possible without their unconditional and infinite love and I am grateful for that.

I would like to specially thank Professor Margaret Wooldridge for giving me the opportunity to join her research group. Her mentorship and management of the research group have been invaluable lessons for me. I thank her for always making time to discuss the ideas and issues as needed.

I would also like to thank my other committee members for their insightful comments and feedbacks: Professor André Boehman, Professor Ilya Kolmanovsky, Research Scientist George Lavoie, and Dr. Steven Wooldridge.

The truly welcoming circle of friends and colleagues in our research group has been a vital part of my education. The scheduled and unscheduled discussions, at times very passionate, about technical and non-technical issues and challenges in the world has been an enjoyable part of my past few years. I have been very fortunate to work, live and have fun with them and I am appreciative for that. I thank the overlapping members of The Tea Party, Optical Research in Combustion Association (ORCA) and student section of the Sweet Friday. Without any particular order I thank: Darshan Karwat, for making the carpooling routine every morning pleasant with a hot mug of tea and passionate discussion about the soccer world, for his unlimited passion about the environment; Scott Wagnon, my office neighbor and volleyball buddy, for his limitless willing to help; Dimitris Assanis for sharing the passion of racing and cars; Andrew Mansfield for great discussions about history of science and also Saturday football games; W. Ethan Eagle for his wisdom and elaborate formulation of his thoughts and insightful feedbacks; Peter Keros for bringing another perspective to the political discussions, and Steven Morris, Paul Teini, Eric Bumbalough, Insu Lee (The wise River) and Siamak Riahi. I hope I am not forgetting anyone unlike DMAK.

I also want to acknowledge the financial and technical contribution of Ford Motor Company - Ford Research and Advanced Engineering. The operation of the two optical engine facilities could not have been possible without the support of Dr. Steven Wooldridge. I would also like to thank Dr. Benjamin Peterson for the collaboration and support in the final stages of my degree and I would like to thank Mr. Joseph Schim for the hardware support of the DISI project. I would also want to thank Dr. James Yi and Dr. Brad VanDerWege for the insightful comments and feedbacks on the projects.

Table of Contents

List of Figures

List of Tables

List of Abbreviations

a. u. – arbitrary unit
AFR – air to fuel ratio
aTDC – after top dead center
bTDC – before top dead center
CA – crank angle
CA50 – crank angle at 50% of heat release
CAD – crank angle degree
CAFÉ – corporate average fuel economy
CMOS – complementary metal–oxide–semiconductor
CO – carbon monoxide
COV – coefficient of variation
DAQ – data acquisition system
DI – direct injection
DISI – direct injection spark ignition
DPF – diesel particulate filter
E0 – neat gasoline
E100 – neat ethanol
E50 – 50% blend of ethanol in gasoline (by volume)
EOI – end of injection
EVC – exhaust valve close
EVO – exhaust valve open
ϕ – fuel/air equivalence ratio
fps – frames per second
FRP – fuel rail pressure
FSN – filter smoke number
γ – specific heat ratio
GDI – gasoline direct injection
HCCI – homogeneous charge compression ignition
HRR – heat release rate
IC – internal combustion
IMAP – intake manifold absolute pressure
IMEPn – net indicated mean effective pressure
IVC – intake valve close
IVO – intake valve open
λ – air/fuel equivalence ratio
LIL – line integrated luminosity
MFB – mass fraction burnt
MON – motor octane number
NOX – nitrogen oxides
PFI – port fuel injection
PM – particulate matter
PW – pulse width
RGB – red, green, and blue
RON – research octane number
RPM – revolutions per minute
σ – standard deviation
SA – spark advance
SA-HCCI – spark assisted homogeneous charge compression ignition
SIC – spatially integrated chemiluminescence
SIL – spatially integrated luminosity
SINL – spatially integrated natural luminosity
SOI – start of injection
TDC – top dead center
UHC – unburnt hydrocarbon

Abstract

The Effects of Ethanol/Gasoline Blends on Advanced Combustion Strategies in Internal Combustion Engines

By

Mohammad Fatouraie

Chair: Margaret S. Wooldridge

This dissertation presents the effects of blending ethanol with gasoline on advanced combustion strategies in internal combustion engines. The unique chemical, physical and thermal properties of ethanol/ gasoline blends can be used to improve the performance and emissions of advanced engine technologies like gasoline direct injection (GDI) also called direct injection spark ignition (DISI), homogenous charge compression ignition (HCCI) and spark assisted homogenous charge compression ignition (SA-HCCI).

This work used experimental studies to understand the impact of ethanol and ethanol/gasoline blends on advanced engine strategies and on understanding which of the fundamental properties of ethanol and ethanol blends control engine performance. The technical approach leveraged high speed imaging to study the fuel spray, combustion, ignition, and sooting

(where appropriate) properties of the fuels using different optically accessible engine hardware, including HCCI and GDI configurations. The results of the HCCI work indicated stable operating conditions could be extended to leaner mixtures using the ethanol blends, if the effect of charge cooling due to fuel vaporization was anticipated. Ethanol also improved the stability of flame initiation and growth in SA-HCCI, which affected the global autoignition and performance of the engine. The effect of ethanol on these chemically-controlled engine modes was dominated by the impact of the fuel on thermal stratification. Ethanol combustion chemistry appeared to have little impact.

Significant reduction in soot formation was observed in the DISI engine studies using ethanol blends compared to a baseline of reference grade gasoline. This was due to combined effects of ethanol on combustion chemistry, where oxygenated fuels suppress the formation of soot precursors, and of ethanol on increasing evaporation and reducing liquid fuel on the piston, where ethanol changed the fuel spray cone angle and spray collapse. In particular, fuel impingement and wetting of the piston surface dominated in-cylinder soot formation, thus the ethanol fuel spray characteristics that reduced interaction of the fuel spray with the piston and enhanced fuel mixing led to less soot formation.

Chapter 1

Introduction

As of 2010, world energy consumption was estimated to be 524 quadrillion BTU and is projected to increase to 630 quadrillion Btu by 2020 and petroleum and other liquid fuels remain the largest source of energy (a third of the global energy) [1]. As energy demands continue to climb, concern over climate change associated with increasing global emissions increases as well. In response, a target atmospheric concentration of 445-490 ppm CO_2-eq has been agreed upon by the global community to limit potential anthropogenic climate change effects [2]. To achieve such targets and address the clean energy problem various renewable energy sources must be considered. In more recent years, U.S. policies such as the Energy Improvement and Extension Act [3], Energy Independence and Security Act [4], Energy Policy Act [5], and Food, Conservation, and Energy Act [6] have incentivized and mandated the production of advanced biofuels. In the United States, ethanol is the most widely produced biofuel with an annualized total of 13.8 billion gallons and the production is expected to grow in the future [7].

Ethanol has been blended with gasoline in the United States and Europe to increase the biofuel share of the energy portfolio and to reduce dependence on crude oil. In countries such as Brazil, with significant biofuel production infrastructure, ethanol is being used in vehicles as a neat fuel, i.e. without blending with gasoline. Some methods to produce ethanol, including cellulosic and algae derived, are making the fuel more attractive as a sustainable transportation fuel that may reduce life cycle carbon emissions and not compete with food crops. Ethanol may provide some CO_2 emissions benefit depending on the fuel processing and feed stocks used. Hill et al. [8] quantified and monetized the life cycle climate change and health effects of greenhouse gas and PM emissions from gasoline and advanced bio-ethanol. For each billion ethanol-equivalent gallons of fuel produced and combusted in the U.S., the combined climate-change and health costs are 469 million U.S. dollars for gasoline, but only 123–208 million U.S. dollars for cellulosic ethanol depending on feed stock (prairie biomass, miscanthus, corn stover, or switchgrass).

Some important thermo-physical properties of ethanol differ from the properties of gasoline, impacting internal combustion (IC) engine performance. Ethanol has a higher laminar flame speed compared to iso-octane [9], [10] which results in shorter combustion duration and therefore higher thermodynamic efficiency [11], [12]. Ethanol as an oxygenate has a high adiabatic peak combustion pressure to temperature ratio due to higher molar expansion ratio which increases the thermal efficiency and decreases the heat losses compared to alkanes [13]. Caton [12] also indicated that the less complex chemical structure of ethanol compared to iso-octane results in lower exergy destruction. Lower NOx and unburned hydrocarbon (UHC) emissions have been demonstrated using ethanol as well [14], [15], outcomes which are attributed to lower combustion temperatures and a lower boiling point compared to gasoline.

Improving IC engine efficiency is an important goal to meet emissions standards like the U.S. corporate average fleet economy (CAFE) regulations. Multiple strategies, like gasoline direct injection (GDI) and down-sizing engines using turbo- and superchargers to boost energy density, are currently in production. Other strategies which have high potential for further improving thermal efficiencies are still in the research and development stage like homogeneous charge compression ignition (HCCI). Advanced engine strategies like GDI and HCCI are sensitive to fuel properties and, in particular, ethanol offers opportunities and challenges to optimizing engine performance. This thesis focuses on understanding the impact of ethanol and ethanol/gasoline blends on advanced IC engine strategies and on understanding which of the fundamental properties of ethanol and ethanol blends control engine performance. The technical approach leverages high speed imaging to study the fuel spray, combustion, ignition, and sooting (where appropriate) properties of the fuels using different optically accessible engine hardware, including HCCI and GDI configurations. The experimental hardware is described in detail in Chapter 2. In the following paragraphs, the challenges of the different engine operating modes and the approach used to evaluate the effects of ethanol are briefly presented.

Homogeneous charge compression ignition is one of the promising advanced combustion methods, benefiting from the advantages of lower temperature, premixed, and fuel lean combustion, which can yield higher thermal efficiencies than spark ignition engines, while achieving significant NO_x emission reduction compared to diesel engines [16–18]. HCCI operates in the lean equivalence ratio regime to achieve the desired combustion timing. This and the mixture homogeneity result in elimination of local rich zones which reduce the particulate emissions significantly. However, due to the dependence on chemical kinetics for controlling ignition rather than a traditional control strategy such as spark ignition or fuel injection timing, accurate control of the temperature, pressure and fuel/air mixture composition is required to stabilize HCCI operation and combustion phasing. The load range over which HCCI operation is viable is currently small compared to the urban driving cycle. At the low load limit, the low energy content of the charge can lead to misfire, while at the high load limit, high peak pressures and heat release rates can result in increased NO_x emissions and damage to the engine.

HCCI technology is flexible in terms of fuels that are acceptable, but combustion characteristics can vary considerably depending on the fuel properties and the operating conditions of the engine [19–23]. While there has been considerable progress in understanding the mechanisms important to successfully implementing HCCI strategies for single fuels, the effects of fuel blends on HCCI are less well understood [24], [25]. Studies have shown that, compared with iso-octane, ethanol advances HCCI timing [26], [27]. Further, Xie et al. [28] found high concentrations of ethanol (E50 and E100) expanded the stable HCCI operating range for fuel equivalence ratio. Extending the operating range is critical to successfully capturing the potential of HCCI to improve engine efficiencies and reduce exhaust emissions. Fuel blends present new challenges and opportunities to improve HCCI performance. The objective of the HCCI study was to characterize the effects of different ethanol-gasoline blends at HCCI operating conditions on the single cylinder port-fuel injection (PFI) research engine. The results are presented in Chapter 3.

One of the promising strategies which has been proposed to extend these limits and improve the viability of HCCI is spark assist [29–32]. Spark assist allows a portion of the fuel/air charge to be consumed by flame propagation prior to auto-ignition, and generally spark assist advances ignition compared to a baseline HCCI operating condition [32]. The timing of auto-ignition is dependent in part on the properties of the fuel.

Studies of SA-HCCI using optically accessible engines have revealed key insights into the combustion phenomena important during SA-HCCI [33], [34]. At the University of Michigan, Zigler et al. have contributed to the understanding of SA-HCCI through the use of a single cylinder optically accessible research engine [35]. Initial work used high-speed imaging of three fuels (iso-octane, pump gasoline, and indolene) to compare combustion characteristics during HCCI operation [36]. A multi-axis imaging study of

SA-HCCI recorded planar and axial views of the ignition and combustion events [37] and demonstrated flames initiated by the spark were approximately spherical. In the most recent work by Zigler et al. [32], imaging data were evaluated quantitatively to determine the effects of spark assist on marginally stable, low-speed, low-load HCCI conditions and showed the limits of spark assist at different preheat conditions and the effects of spark timing. This work and others showed spark assist is only effective as a control variable within maximum and minimum in-cylinder temperature limits.

The objective of the SA-HCCI study was to compare the effects of spark assist on the ignition and combustion properties of gasoline-ethanol blends minimizing the effects of temperature by controlling the end of compression temperature of the fuels. High-speed imaging of the combustion chamber was used to identify the relationship between engine performance metrics and the location and propagation rate of flames initiated by the spark for the fuels at different stoichiometries. Chapter 4 presents the results and discussion of the SA-HCCI study.

Fuel economy and CO_2 emissions advantages make gasoline direct injection engines attractive for passenger car and light duty truck fleets, which has resulted in increased market share [38] of these direct injection spark ignition (DISI) engines. The technology is considered one of the pathways to meet CAFÉ targets. Direct injection of the fuel into the combustion chamber decreases the charge temperature and thus increases the volumetric efficiency of the engine and reduces the knock potential at higher compression ratios [39]. Therefore, DI engines have higher thermal efficiency and higher power output than the port fuel injected gasoline counterparts. DI also improves the transient response of the engine; however, particulate matter (PM) emissions of DISI engines have become a concern. Studies have shown that PM emissions of DISI engines are an order of magnitude higher than the PM emissions of port fuel injected gasoline engines or diesel engines equipped with diesel particulate filters [40–42]. Important factors affecting soot formation are the local equivalence ratio, temperature, chemical structure and thermo-physical properties of the fuel [43]. Methods to reduce PM emissions from DISI engines are important, and ethanol fuel blends may be a means to reduce PM emissions, while maintaining DI engine performance.

Ethanol has been demonstrated to feature reaction chemistry which is intrinsically less likely to produce PM. Kasper et al. [44] investigated differences in ethanol versus hydrocarbon combustion chemistry and observed a strong ability of ethanol to suppress the formation of benzene as well as some higher aromatic species; species considered precursors or building blocks for PM. Barrientos et al. [45] measured the sooting tendency of a range of fuels and fuel blends and showed ethanol leads to a decrease in the sooting tendency of ethanol/gasoline blends. The addition of alcohols to diesel fuel can considerably decrease the PM emissions of diesel engines [46], [47], but the effects of ethanol blends in DISI engines are less well understood and some results are contradictory. Chen et al. [48] concluded that an increase in ethanol addition leads to an increase in PM both in particle number and mass, but a decrease in PM emissions has been demonstrated by Francqueville [49] and Ericsson et al. [40] over the entire driving cycle for higher (E85) content of ethanol in the fuel. Storey et al. [50] showed decreased PM emissions for lower content of ethanol in the fuel (E10-E20), while He et al. [51], [52] concluded that low ethanol content in fuel exhibits almost the same particle emissions as gasoline.

Experiments to capture time resolved in-cylinder imaging of the fuel spray properties and the corresponding soot formation were conducted for ethanol/gasoline fuel blends to understand the fundamental effects of ethanol blends on fuel spray properties and in-cylinder soot formation. The optically accessible single cylinder DISI engine was used to acquire high speed imaging data of fuel spray and PM formation in the engine as a function of the ethanol content in the fuel, the fuel injection timing, and engine coolant temperature. These data provided the first direct insight into the physical mechanisms controlling PM formation in ethanol fuel blends in DISI engines. Chapter 5 includes the results and conclusions based on this DISI study.

The next part of the study investigated 100% anhydrous ethanol and imaging from the direction orthogonal to the axis of the fuel injector. The change in imaging orientation allowed direct imaging of the fuel spray interaction with the piston surface, which the previous part of the work identified as critical to understanding the effects of ethanol on in-cylinder soot formation. Engine-out smoke measurements were also performed to link the in-cylinder PM imaging to the PM exhaust measurements. The results of this study are presented in Chapter 6.

Other factors are important in creating the local conditions which lead to high soot formation rates in DISI engines. The fuel properties affecting charge preparation, in particular spray break-up, atomization, and vaporization, play important roles on fuel impingement on combustion chamber surfaces and on thermal and compositional charge stratification. The higher kinematic viscosity of ethanol results in lower Reynolds numbers, therefore affects the turbulence induced by the spray and spray break-up. The lower specific heating value of ethanol compared to results in a larger volume of ethanol injected in each cycle to output equivalent power. These properties coupled with the significantly higher enthalpy of vaporization and lower boiling point of ethanol affect the spray pattern, spray tip penetration and mixing [53].

Temperature also affects the spray characteristics of the fuel. The azeotropic behavior of the gasoline-ethanol blend lowers the initial distillation temperature of the mixture [54], [55], therefore increasing the initial volatility which affects the spray vaporization characteristics of the blends. Differences in the spray pattern of different fuels have been demonstrated by Serras-Pereira et al. [56] in a motoring engine. However, the effects of residual heat from combustion were not identified in the study. The timing of the fuel injection also affects the homogeneity of the charge. Earlier start-of-injection (SOI) enhances the mixing and vaporization, but earlier SOI can increase fuel impingement on the piston bowl and thereby produce a film of liquid fuel on the piston top which can become a significant source of PM emissions [57],[58]. Moreover, Barone et al. [59] concluded that DISI particle morphology was a function of fuel injection timing, with fewer liquid droplets and more single solid sub-25 nm spheres generated by retarded injection, and PM morphology affects fate and transport in the environment. For this study, experiments were conducted to capture the full view of the fuel spray interaction with the cylinder and piston. The optically accessible single cylinder DISI engine was equipped with a full length transparent liner to acquire high speed imaging data of fuel spray and impingement as a function of fuel blend, the fuel rail pressure, and engine coolant temperature. A retarded fuel injection timing was chosen to isolate the effects of cylinder wall impingement. The results and analysis details of this study are presented in Chapter 7.

The overall conclusions of the effects of ethanol on advanced IC engine performance and suggestions for future work are provided in Chapter 8.

Chapter 2

Experimental Setup

Investigation of the effects of different gasoline and ethanol fuel blends on charge preparation, combustion and emission characteristics were performed using two optical engine facilities at the University of Michigan. The kinetically controlled combustion studies were performed using a port fuel injection (PFI) optical engine with early fuel injection to enhance the charge homogeneity. The in-cylinder formation studies of particulate matter emissions were being performed using a direct injection spark ignition (DISI) gasoline engine, also with optical access. Based on the objective of each study, the data acquisition systems were modified, and the different components and features of the experimental systems are presented in this chapter.

2.1 PFI Optical Research Engine

A detailed description of the experimental facility is provided in [35]. The engine schematic is shown in Figure 2-1. Briefly, a base Ford Zetec-SE 1.25 L engine was modified to utilize one of the four cylinders. The aluminum cylinder head was equipped with fixed dual overhead cams with twin intake and exhaust valves. The engine bore of Ø71.9 mm, equipped with flat-top piston, with the stroke of 76.5 mm provided 0.31 L of displacement and a compression ratio of 10:1. The piston was modified to include a fused silica disc insert of Ø48.5 mm for optical access.

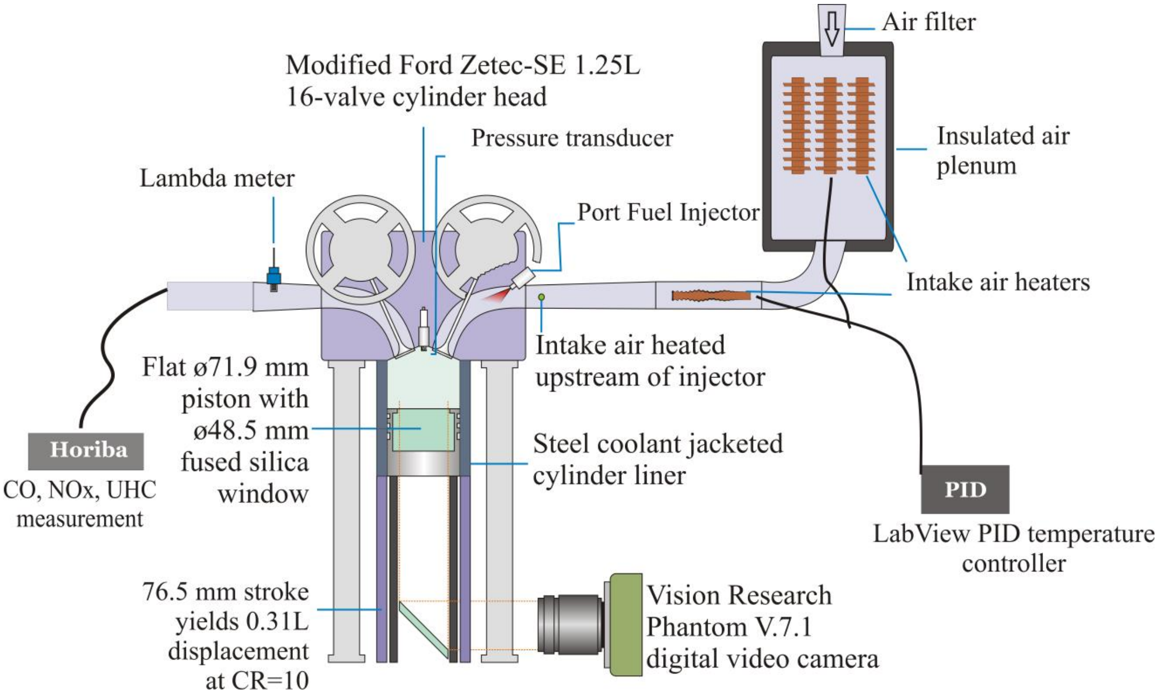

Figure 2-1. PFI single cylinder optical engine schematic.

The valve timing used for all experiments was intake valve opening (IVO) at 2° before top dead center (bTDC) with duration of 224 CAD and exhaust valve closing (EVC) at 10 °aTDC with duration of 224 CAD. The PFI engine cam timing events are presented in Figure 2-2.

In-cylinder pressure was measured using a piezoelectric transducer (Kistler 6125A) and charge amplifier (Kistler 5010B), and intake pressure was monitored using an absolute pressure sensor in a water cooled fitting (Kistler 4045A2) and amplifier (Kistler 4618). The in-cylinder pressure and the piston phasing data were acquired after the engine was thermally equilibrated and was in stable firing operation for approximately 5 seconds in each experiment.

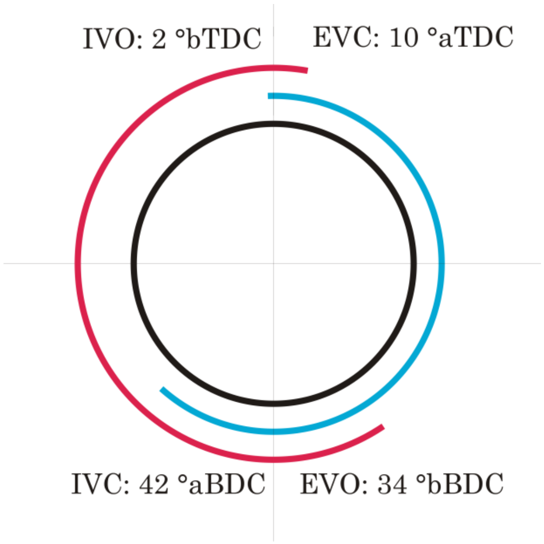

Figure 2-2. PFI engine intake and exhaust cam timing.

The engine was driven by a hydraulic dynamometer (Micro-Dyn 35) equipped with a control system which regulates the engine speed by compensating between providing a load or absorbing net power output. The engine control module for spark and fuel injection is integrated with the dynamometer control system. Fuel equivalence ratio was controlled by varying the fuel injector driver pulse width (PW) duration while setting a constant fuel rail pressure of 25 psi. Fuel was port injected slightly upstream of the twin intake ports at 172 kPa (Siemens DEKA II dual conical jet injector) at the top dead center timing of the previous cycle (to ensure good fuel/air mixing prior to introduction into the cylinder). All experiments in the study were operated naturally aspirated at wide open throttle.

The intake air preheat system consisted of a primary heating tank and a secondary flow torch. A 30 liter insulated tank was equipped with 3 strip heaters providing 1.5 kW of total heat to increase the intake air temperature to 250 °C. The final temperature of the intake air was controlled by a 2 kW flow-torch air heater (Flow Torch™ 200) located before the intake runner, achieving the accuracy of ±1 °C of the target temperature. The air intake temperature was measured upstream of the fuel injection location.

2.2 DISI Optical Research Engine

The DISI engine cylinder head hardware was based on a 4-valve gasoline direct injection engine geometry. Axial and orthogonal optical access was available through piston window inserts and transparent cylinder liners. For this study, side-view imaging through the transparent cylinder liner was used with a metal piston (with no optical window) that included realistic production bowl geometry. The aluminum cylinder head featured a side-mounted fuel injector with dual overhead camshafts and 4 valves around a centrally mounted spark plug. The engine geometry used a ø89.0 mm bore and 81.4 mm stroke, yielding 0.51 L displacement with nominally 9.4:1 compression ratio. The single cylinder engine design is capable of replicating intake and exhaust valve event timings consistent with a twin-independent variable camshaft timing system, and the valve timing used for all experiments was intake valve opening (IVO) at 11° after top dead center (aTDC) with duration of 236 CAD and exhaust valve closing (EVC) at 38 °aTDC with duration of 224 CAD. The DISI engine cam timing events are presented in Figure 2-3.

Cylinder pressure was measured using a piezoelectric transducer (Kistler 6052A) and charge amplifier (Kistler 5010B). Absolute manifold pressure was measured using a Druck PMP-2060 transducer and the intake pressure was measured at the intake runner with a Kistler 4045A2 transducer and a Kistler 4618 amplifier.

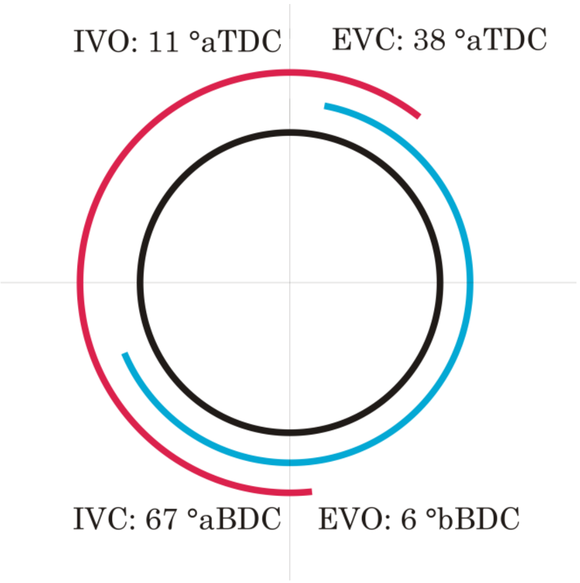

Figure 2-3. DISI engine intake and exhaust cam timing.

2.3 Data Acquisition System

The data acquisition system was structured for Labview software using National Instruments devices. The National Instruments Compact Data Acquisition chassis NIcDAQ-9174 USB was used with an NI-9401 card for digital input/output, an NI-9215 card for analog input and an NI-9213 card for thermocouple input. Analog signals include the intake plenum and intake runner pressure, in-cylinder pressure, λ value, and the emission values from the Horiba gas analyzer for CO, HC, and NO_x. Digital input signals include the top dead enter (TDC) marker, spark and fuel signals, and a digital output signal is generated to trigger the high-speed camera. Intake and exhaust plenum and runner temperatures as well as coolant in and out and oil temperatures were measured using thermocouples.

The data acquisition code was designed in Labview for synchronization of the data, display while executing the experiments and recording the desired data. The sample rate was 60 kHz. For the HCCI experiments the intake temperature controller was added to the Labview code.

The crank angle was encoded using a BEI encoder with 360 signals per revolution. This signal was used for the fuel injection and spark timing. The timing of top dead center (TDC) was measured with a TDC marker sensor. Both of these signals were used with the engine control unit to generate the fuel and spark signal.

The fuel/air equivalence ratio was measured based on the oxygen concentration in the exhaust using a lambda meter (ETAS LA4) with a broadband lambda sensor (Bosch LSU 4.9). The lambda meter settings were changed for each fuel using the appropriate C/O and C/H ratios. The exhaust gas emissions (CO, UHC, CO_2, and NOx) were measured using an automotive emissions analyzer (Horiba MEXA-584L).

For the DISI experiments, the engine-out particulate matter (PM) emissions were measured using an opacity meter (AVL 415 smoke meter) with a 6 s sample duration (sample volume of 1080 cm3) and a filter smoke number (FSN) was calculated based on the blackening index of the filter. Exhaust plenum temperature significantly affected the smoke meter reading (probably due to oxidation of the particles). The sensitivity of paper blackening to exhaust temperature is well known [60]. Therefore, the exhaust plenum temperature was controlled to ~80°C for these experiments. This was achieved by operating the engine at a lean condition and retarding injection timing (to suppress sooting) until the exhaust plenum was stable at 80°C, then switching to the actual test conditions. The temperature of the bottom surface of the piston was measured using an Omega OS101 infrared transmitter. The emissivity calibration was performed using a precision fine wire thermocouple mounted on the bottom surface of the piston while the piston temperature was controlled using the coolant temperature (while the engine was not running) from 15° C to 95° C. The emissivity value of ε=0.645 was used for the temperature measurements. The accuracy of the measurements are ±2% with 100 ms response time. High thermal conduction of aluminum results in a small temperature drop across the piston top, which has been demonstrated by Steeper et al [61].

2.4 High Speed Imaging

For the experimental results presented in Chapter 4, the combustion chamber was imaged through the piston window using a high-speed color digital video camera (Vision Research Phantom v7.1, color). A fast 50 mm lens (f/0.95 Nikkor TV lens) and C-mount extension tubes were used with the camera to adjust the focal length and to reduce the focal depth along the cylinder axis. In this study, the camera was focused at a plane coinciding with the spark plug ground electrode. Visible chemiluminescence emission was recorded at 3000 frames per second (fps) with 309 μs exposure time and 320 x 320 pixels resolution. No additional spectral filters were used other than the inherent spectral characteristics of the camera and the supporting optics. The diameter of the piston window was 48.5 mm, which partially occluded the valves. Recall, the total piston diameter was 71.9 mm. Thus, 45.5% of the projected area of the combustion chamber was imaged near TDC. Camera images were time sequenced to a common trigger signal with the in-cylinder pressure data. The imaging data were synchronized with the pressure data with an uncertainty of ~ 1–2 CAD.

For the experimental results presented in Chapters 5, 6 and 7, the combustion chamber was imaged through the fused silica cylinder liner using a high-speed color digital video camera with a widescreen CMOS array (Vision Research Phantom v7.11, color). A macro 105 mm lens (af micro Nikkor 105mm f2.8 d) was used with the camera to adjust the focal length and a setting of f4.0 was selected to optimize the focal depth and light exposure. Two high intensity LED arrays (1 × 3 array of 3-watt cool white LEDs) were installed to visualize the spray. The position and angle of the LED lights were adjusted based on the orientation of the camera. The camera was focused at a plane coinciding with the spark plug ground electrode. The camera settings were fixed at 9000 frames per second (corresponding to 1 frame/CAD at engine speed of 1500 RPM) with 100 μs exposure time. Non-filtered emission was recorded via the high-speed color digital camera and time-sequenced with the crank-angle resolved pressure data. The imaging data captured flame propagation (via chemiluminescence), soot formation (via incandescence/thermal emission of the soot particles) and scattering of the LED light by the fuel spray.

2.5 Fuel Specifications

The baseline gasoline used in this study was Indolene (EPA Tier II EEE) which is a research grade gasoline. The fuel specifications provided by the supplier (Haltermann) are presented in Table 2-1.

Table 2-1. EPA Tier II EEE specifications of Indolene provided by Haltermann

Parameter	Unit	Specification Min	Specification Max	Result
Distillation- Initial Boiling Point	°C	24	35	29
5%	°C			44
10%	°C	49	57	52
50%	°C	93	110	105
90%	°C	152	163	159
95%	°C			168
Distillation- End Point	°C		213	200
Recovery	vol %			97.7
Residue	vol %			1.1
Loss	vol %			1.2
Gravity	°API	58.7	61.2	59.2
Density	kg/l	0.734	0.744	0.741
Reid Vapor Pressure	kPa	59.98	63.43	61.36
Carbon	wt fraction			0.8646
Hydrogen	wt fraction			0.136
Hydrogen/Carbon Ratio	mole/mole			1.881
Stoichiometric Air/Fuel Ratio				14.628
Oxygen	wt %		0.05	<0.01
Sulfur	wt %	0.0025	0.0035	0.0034
Composition, aromatics	vol %		35	28
Composition, olefins	vol %		10	0
composition, saturates	vol %			72
Particulate Matter	mg/l		1	0.7
Research Octane Number		96.0		97.2
Motor Octane Number				89.0
Net Heating Value	MJ/kg			43.012

The ethanol used in the experiments was Ethyl Alcohol USP 200 Proof from Sigma Aldrich. The fuel specifications provided by the supplier are presented in Table 2-2.

Table 2-2. Ethyl Alcohol USP 200 Proof specification

		Specification		
Parameter	Unit	Min	Max	Result
Purity	vol %	99.9		100.0
Boiling Point	°C			78
Density	kg/l	0.790	0.793	0.791
Reid Vapor Pressure	kPa			44.6
Carbon	wt fraction			0.521
Hydrogen	wt fraction			0.131
Oxygen	wt fraction			0.347
Hydrogen/Carbon Ratio	mole/mole			3
Stoichiometric Air/Fuel Ratio				9
Water	vol %		< 0.10	0.0
Non Volatile Residue	ppm		< 25	0.0
Sum of Acetal & Acetaldehyde	ppm		< 10	2
Benzene	ppm		< 2	0.0
Methanol	ppm		< 100	27

The indolene was mixed with anhydrous ethanol to produce each fuel blend. Each fuel blend was measured and poured into a glass container which was pre-rinsed with ethanol and then dried. The container was shaken vigorously to mix the fuels initially and again before adding to the engine fueling system. Between each blend, the fuel system was purged once using a small amount of the new blend.

Chapter 3

Homogeneous Charge Compression Ignition Studies of Ethanol and Gasoline Blends

3.1 Objective

Fuel blends present new challenges and opportunities to improve HCCI performance. The objective of this study was to characterize the effects of different ethanol-indolene blends at HCCI operating conditions on a single cylinder research engine. Specifically, the sensitivity of the engine performance characteristics such as maximum in-cylinder pressure, combustion phasing, heat release rate and net indicated mean effective pressure ($IMEP_n$) to the volume-percentage of ethanol in a gasoline fuel blend was investigated. The results are considered in the context of the effects of ethanol on in-cylinder temperatures and ignition delay times. A model to estimate ignition delay time is developed to interpret the trends observed in the experimental data.

Most of the content of this chapter has been published as a SAE Technical Paper [62].

3.2 Experimental Approach

This study was conducted using the PFI single cylinder optical research engine facility of the University of Michigan, which is described in section 2.1.

For all experiments, the engine coolant was maintained at 90°C and oil temperature at 60°C. The engine was motoring for 30 minutes at the oil and coolant temperatures before data acquisition. Fuel was port injected slightly upstream of the twin intake ports at 172 kPa at the top dead center timing of the previous cycle (to ensure good fuel/air mixing prior to introduction into the cylinder). Indolene was used as the baseline fuel and it was mixed with anhydrous ethanol to produce E10, E20 and E30.

All experiments were conducted at an engine speed of 700 RPM and the in-cylinder pressure and the piston phasing data were acquired at 60 kHz to determine the maximum pressure (P_{cyl}), rate of pressure rise ($dP/d\theta$), phasing of maximum rate of pressure rise, heat release rate ($dQ/d\theta$), 50% of the total heat release (CA50) and the average net indicated mean effective pressure (IMEP, 720 CAD). For the first set of experiments, the intake air temperature and fuel/air equivalence ratio (Φ) were varied to study the effects of different indolene-ethanol blends (E0, E10, E20, and E30) on the engine performance during HCCI operation. The experimental strategy was to identify the low temperature range of stable HCCI operation for each fuel blend, then increase the temperature in 10°C increments. For each temperature setting, three fuel injection duration levels (i.e. pulse widths) were applied to study the effects of different equivalence ratios at the same intake temperature. Approximately the same volume of fuel blend was injected per cycle for each pulse width setting. Ethanol, like any oxygenated fuel, has a fuel-leaning effect when mixed in this way. However, ethanol has a slightly higher density and significantly lower molecular weight than indolene. The net effect is that a larger amount of fuel is injected per cycle on a per mole basis with increasing ethanol content in the blend. This slightly offsets the fuel leaning effects of adding ethanol to the fuel blend.

A second set of experiments was designed to minimize the thermal effects introduced by the fuel blends and to study the engine performance during

HCCI operation while targeting the same end of compression temperature (T_{EOC}) for each fuel/air mixture. For these experiments, the charge cooling due to fuel evaporation and the effects of the fuel/air mixture properties on compression heating were estimated using the fuel properties and thermodynamic relations. Specifically, the intake charge temperature decreases due to the heat transfer required to evaporate the injected fuel blend. The amount of heat loss is determined by the injected fuel mass and the enthalpy of vaporization of the fuel blend. Higher fuel equivalence ratios lead to more charge cooling of the fresh air. The specific enthalpy of vaporization of ethanol (h_{vap} = 919 kJ/kg) is significantly higher than that of indolene (h_{vap} = 380.5 kJ/kg). Therefore, higher concentrations of ethanol in the fuel lead to more charge cooling for the same fuel injector pulse width and for fuel blends with the same equivalence ratio. The highest equivalence ratio of E30 studied in this work can lead to ~30 K decrease in air intake temperature due to fuel evaporation alone. Changes in the mixture composition also impact the amount of compression heating of the fuel/air mixture via changes in the ratio of specific heat of the mixture, γ. The higher equivalence ratio conditions experience less compression heating, which further leads to cooler temperatures at the end of compression compared to lower equivalence ratio conditions. Thermodynamic relations were used to estimate the effects on T_{EOC} for each fuel/air mixture, and the intake air temperature and the fuel injection duration were then set to target the same T_{EOC} for all indolene-ethanol blends and equivalence ratios. Changes in the heat transfer in the intake manifold that occur due to the different fuel blends were not considered in these experiments.

3.3 Experimental Results

Effects of Fuel Blend and Intake Air Temperature

The intake air temperature (T_{intake}) and the fuel injection pulse width (PW) were varied to characterize the effect of different fuel blends on the combustion properties and engine performance. The engine operating conditions for this set of experiments are listed in Table 3-1. The listed values are the average of ~30 combustion cycles, where the data have been acquired after the engine was thermally equilibrated and firing. Recall, the engine was fired for short periods of time to preserve the optical components and limit thermal drift. The instability of the peak pressure data was significantly higher at the lowest T_{intake}. This was even more notable at low equivalence ratios and higher ethanol content of the fuel. Higher unburned hydrocarbon (UHC) concentrations and retarded phasing make these operating conditions inefficient. CO emissions were higher because of weak combustion despite operating at fuel lean conditions. At the other extreme, at higher T_{intake} and higher equivalence ratio conditions, very advanced phasing resulted in engine knocking and unacceptably high levels of NO_x emissions.

Table 3-1. Engine operating conditions and performance results as a function of fuel blend and intake air temperature for HCCI studies

Fuel	T_{in} [°C]	PW [ms]	φ	NO_x [ppm]	HC [ppm]	CO [%]	P_{max} [bar]	COV_{Pmax} [%]	θ_{Pmax} [CAD]	$\sigma_{\theta Pmax}$ [CAD]	HRR_m [J/CAD]	IMEP [bar]	COV_{IMEP} [%]
E0	290	3.0	0.60	540	260	0.11	31.4	0.56	-1.0	0.79	52.17	1.38	2.80
E0	300	3.0	0.60	580	400	0.12	31.7	0.45	-3.8	0.48	57.08	1.31	2.59
E0	310	3.0	0.60	850	300	0.12	31.4	0.51	-5.1	0.69	58.63	1.18	3.32
E0	320	3.0	0.60	370	1125	0.16	30.8	0.73	-6.3	0.46	60.54	1.07	3.78
E0	290	2.5	0.52	12	580	0.10	25.0	2.97	7.0	1.33	25.09	1.25	2.98
E0	300	2.5	0.53	15	520	0.12	27.7	0.91	2.7	0.58	33.14	1.19	2.04
E0	310	2.5	0.53	32	480	0.13	28.5	0.67	-0.4	0.62	36.99	1.08	2.90
E0	320	2.5	0.53	11	650	0.16	27.8	1.22	0.6	0.73	36.07	1.11	2.52
E0	290	2.0	0.45	19	730	0.16	20.0	7.27	10.9	5.25	11.69	0.98	4.64
E0	300	2.0	0.46	0	715	0.14	21.9	3.55	8.6	1.22	14.30	0.95	2.91
E0	310	2.0	0.45	0	570	0.14	24.8	1.50	2.8	0.79	21.17	0.83	2.76
E0	320	2.0	0.45	0	570	0.16	24.3	2.12	2.8	0.89	20.18	0.78	3.12
E0	330	2.0	0.47	0	620	0.14	26.0	0.62	0.3	0.60	26.82	0.94	2.92
E10	290	3.0	0.54	22	540	0.17	26.8	2.33	6.0	1.31	30.16	1.45	2.73
E10	300	3.0	0.55	13	680	0.16	28.6	1.04	2.8	0.83	37.12	1.49	2.61
E10	310	3.0	0.56	230	600	0.16	30.0	0.69	-1.0	0.60	45.42	1.45	2.33
E10	320	3.0	0.58	270	560	0.17	30.4	0.53	-3.5	0.53	51.43	1.31	3.02
E10	290	2.5	0.48	3	780	0.18	23.1	2.65	8.9	0.96	18.13	1.29	2.17
E10	300	2.5	0.49	0	720	0.16	25.2	2.22	5.6	0.90	23.43	1.25	2.36
E10	310	2.5	0.50	4	750	0.15	26.8	1.12	2.4	0.79	29.55	1.22	2.54
E10	320	2.5	0.51	2	670	0.15	26.9	0.86	1.4	0.69	30.72	1.18	2.52
E10	330	2.5	0.52	5	560	0.14	28.1	0.46	-1.2	0.43	36.84	1.10	2.21
E10	300	2.0	0.43	0	800	0.16	22.6	2.62	6.8	1.07	14.81	1.00	2.74
E10	310	2.0	0.44	0	790	0.15	23.1	1.86	5.4	0.93	16.53	0.95	2.63
E10	320	2.0	0.44	0	780	0.15	23.6	2.18	4.4	0.96	18.07	0.94	2.34
E10	330	2.0	0.45	0	700	0.14	25.6	0.65	0.9	0.53	24.13	0.88	2.17
E20	290	3.0	0.56	0	700	0.14	25.0	4.75	8.9	1.72	24.76	1.49	2.12
E20	300	3.0	0.55	10	660	0.13	25.7	2.86	7.4	1.16	26.99	1.43	1.79
E20	310	3.0	0.56	40	580	0.13	26.9	1.97	4.9	1.04	31.34	1.34	2.84
E20	320	3.0	0.58	400	460	0.14	29.8	0.65	-1.1	0.77	46.44	1.16	3.30
E20	330	3.0	0.58	480	400	0.15	29.7	1.29	-2.6	1.07	47.97	1.19	3.16
E20	290	2.5	0.49	0	850	0.18	18.4	8.40	14.6	1.75	10.99	1.19	3.91
E20	300	2.5	0.49	0	760	0.14	23.3	4.56	8.4	1.63	18.89	1.20	2.36
E20	310	2.5	0.49	0	730	0.14	24.5	3.14	5.9	1.16	22.32	1.09	2.81
E20	320	2.5	0.51	0	600	0.13	26.6	1.06	2.6	0.66	29.30	1.10	2.94
E20	330	2.5	0.52	30	550	0.13	28.1	0.61	-1.1	0.51	35.29	1.04	3.08
E20	300	2.0	0.43	1	820	0.18	18.3	7.77	11.4	1.43	8.44	0.83	5.17
E20	310	2.0	0.43	0	850	0.15	22.1	2.34	6.7	0.89	14.37	0.83	2.16
E20	320	2.0	0.44	0	670	0.16	21.0	3.19	6.9	1.02	13.24	0.71	2.60
E20	330	2.0	0.45	0	750	0.14	24.6	0.73	1.8	0.46	21.51	0.67	3.19
E30	290	3.0	0.54	0	700	0.18	18.7	10.21	14.8	4.09	12.47	1.40	3.46
E30	300	3.0	0.53	0	690	0.17	22.8	3.19	9.3	1.42	19.71	1.31	2.69
E30	310	3.0	0.53	7	590	0.17	25.1	1.77	4.9	0.95	25.96	1.12	2.22
E30	320	3.0	0.53	10	540	0.17	25.2	1.22	4.0	0.88	25.84	1.05	3.07
E30	330	3.0	0.53	20	760	0.18	26.2	0.90	1.5	0.79	31.07	1.05	4.31
E30	300	2.5	0.47	0	850	0.16	21.0	3.82	9.8	1.43	13.48	1.06	3.06
E30	310	2.5	0.48	0	610	0.17	21.3	3.49	8.7	1.44	15.11	0.96	4.15
E30	320	2.5	0.48	0	779	0.16	23.7	1.64	4.7	0.93	20.43	0.86	2.92
E30	330	2.5	0.49	0	770	0.16	23.7	1.17	3.8	0.80	20.93	0.92	3.13
E30	300	2.0	0.42	2	960	0.21	17.5	5.54	11.6	1.20	7.21	0.72	4.76
E30	310	2.0	0.42	0	800	0.20	17.6	6.65	11.1	1.54	7.38	0.69	5.64
E30	320	2.0	0.43	0	840	0.16	20.7	2.73	6.9	1.10	11.88	0.67	3.97
E30	330	2.0	0.43	0	845	0.16	21.6	1.26	4.7	0.70	13.39	0.67	3.64

Experimental results for the average maximum in-cylinder pressure and the corresponding average phasing of peak pressure are shown in Figure 3-1 as a function of the intake air charge temperature for a fixed fuel injection pulse width of PW=2.50 ms. Note the intake temperatures have been corrected for charge cooling, but they do not reflect the heat losses that occur in the intake manifold or changes in compression heating that occurs with changing the composition of the mixture. As noted above, increasing the ethanol content of the fuel blend for fixed fuel pulse width slightly decreases the equivalence ratio of the fuel/air mixture. For the data shown in Figure 3-1, Φ varies from 0.53 (E0) to 0.48 (E30). The error bars in the figure represent the standard deviation of the data over the ~30 combustion cycles and, hence, the stability of the engine at each operating point. As expected, the peak pressures increase with increasing charge temperature for all ethanol blends. At the highest intake temperatures considered, the mixtures are igniting advanced of TDC for all blends except E30. The advanced phasing attenuates the response of the peak pressure to increasing T_{intake}. For blends at the same intake charge temperature, i.e. the temperature after fuel evaporation, the data show the peak pressures of the fuel blends are lower than neat indolene and there is higher variability in the magnitude and timing of the peak pressures of the ethanol blends. The addition of ethanol also retards combustion phasing, which is consistent with the lower equivalence ratio of the blends with higher ethanol concentrations and the lower end of compression temperatures. Similar trends were observed for the higher and lower fuel pulse widths considered (PW = 3.00 ms and PW = 2.00 ms). The data demonstrate the stable operating limit for the engine shifts to higher intake temperatures and equivalence ratios as the ethanol content of the fuel increases. The transition to the unstable regime is indicated by the much higher cycle-to-cycle variation of the peak pressure at lower intake charge temperatures. At the lowest temperature condition of E30 the data point is missing because stable combustion could not be achieved.

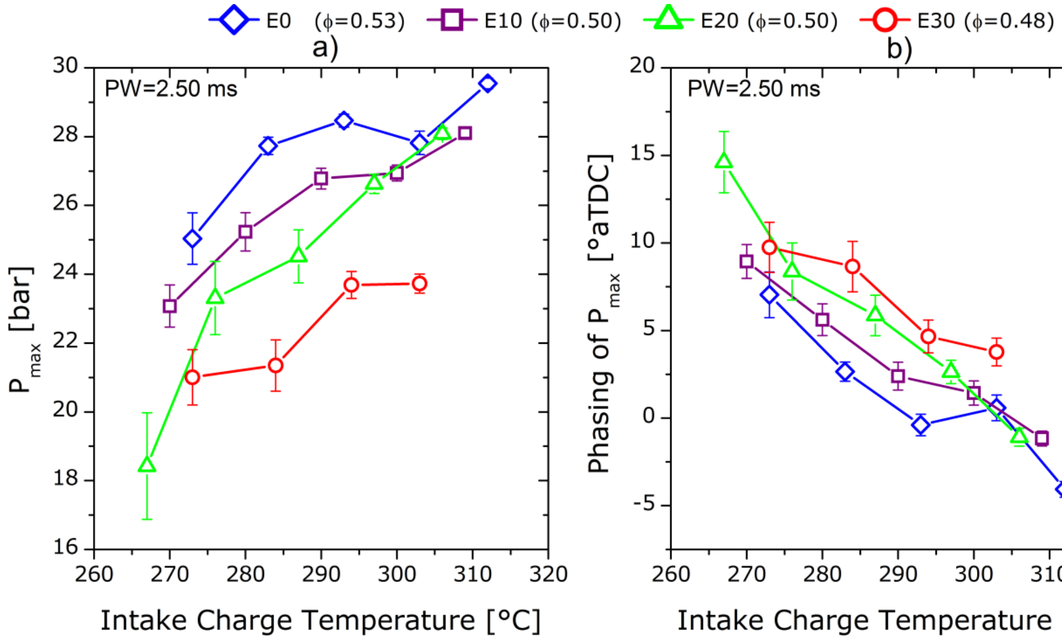

Figure 3-1. Experimental results for (a) average maximum in-cylinder pressure and (b) average phasing of the maximum pressure of indolene-ethanol blends as a function of intake charge temperature for a fuel pulse width of PW=2.50 ms.

Experimental results for the average $\mathrm{IMEP_n}$ for the PW=2.50 ms condition are presented in Figure 3-2 as a function of the peak cylinder pressure and the phasing of the 50% of heat release (CA50). The data presented are for the same experimental conditions shown in Figure 3-1. As seen in Figure 3-2, $\mathrm{IMEP_n}$ values comparable to neat indolene can be achieved with the E10 blend, despite the lower in-cylinder pressures compared to neat indolene. This is due to the increase in ignition delay time which retards ignition to more optimal phasing. Further increase in the ethanol content retards the combustion, lowering peak pressures and increasing the cycle-to-cycle variability of $\mathrm{IMEP_n}$ for the E20 and E30 blends. The lower stability is attributed to the high levels of charge cooling that occurs with the addition of ethanol and fuel leaning effects which simultaneously retard ignition. The reaction chemistry of ethanol may also contribute to the observed stability limits.

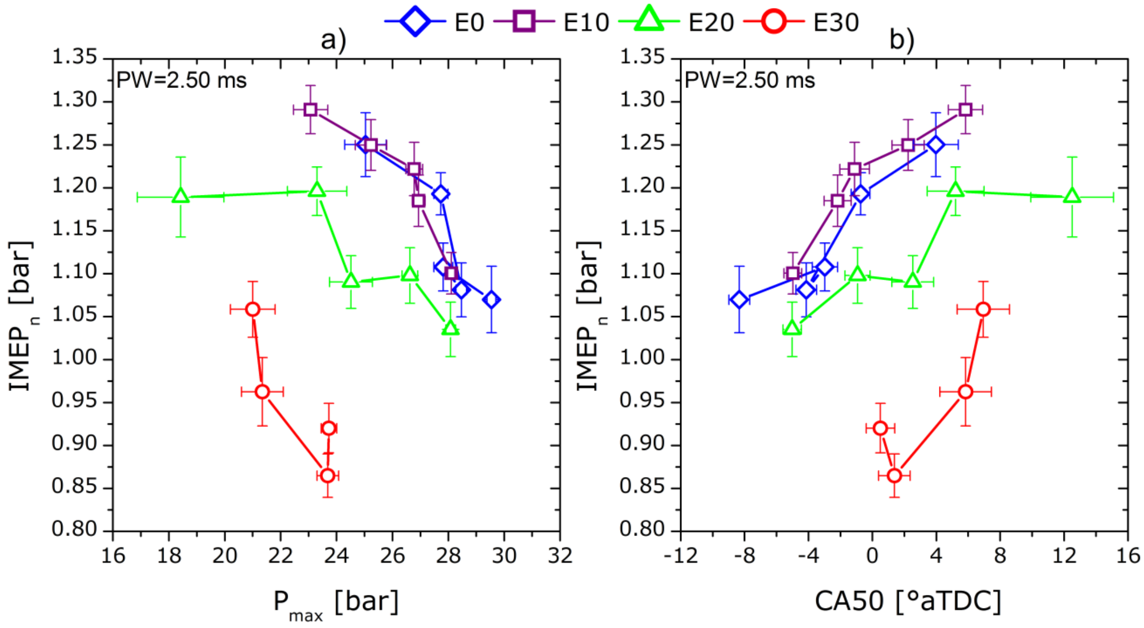

Figure 3-2. Average IMEPn as a function of (a) maximum average cylinder pressure and (b) phasing of the maximum average cylinder pressure for indolene-ethanol blends with fuel pulse width of PW=2.50 ms.

As seen in Table 3-1, the experimental results for NO_x emissions correlate well with maximum in-cylinder pressure. Specifically, significant reduction in NO_x emissions were observed as ethanol content increased, from 2360 ppm for E0 to 20 ppm for E30, at PW=3.00 ms and T_{intake}=330 °C. This effect is more significant at conditions with higher equivalence ratios.

A model was used to interpret the trends observed in the experimental data as a function of the fuel blends. Specifically, the model estimated the ignition time (θ_{ign}) for each fuel blend and engine operating condition and assigned an ignition delay time (τ_{ign}) for each case. The details of the ignition model are described in [62]. The instantaneous in-cylinder temperature was estimated using the in-cylinder pressure time history, the thermodynamic properties of the fuel/air mixture, and assuming isentropic compression of ideal gases. The calculation uses the temperature-dependent ratio of the specific heats, γ, of the different fuel/air mixtures. The model does not consider changes in the heat transfer that occurs due to difference in the fuel blends.

The model for ignition timing can be used to explain the trends observed in engine performance. In particular, estimated values for the ignition delay time, τ_{ign}, in units of crank angle degrees are presented in Figure 3-3 as a function of intake charge temperature for the three fuel pulse widths considered in the current work. The ignition delay of zero corresponds to the crank angle at which the charge reaches the trigger temperature (T_{trig}), which is the temperature threshold that the ignition delay times are on the order required for phasing near TDC and 1020 K was chosen as an estimate for T_{trig} based on fundamental and applied engine studies of the ignition properties of iso-octane [63]. The trends in the model predictions are in excellent agreement with the experimentally observed trends in the engine data. The data show an increase of the ignition delay time as the ethanol content of the fuel increases for the same intake charge temperature. The longer ignition delay times at the same charge temperatures are due to the fuel leaning effects of the higher ethanol blends. The longer ignition delay times retard ignition phasing, decreasing $IMEP_n$ and engine stability. The model estimates also indicate little difference between the E0 and E10 fuels. Note that at lower fuel injection pulse widths there are fewer estimated points. This is because of the divergence of the ignition delay after TDC and never reaching the ignition point at the model.

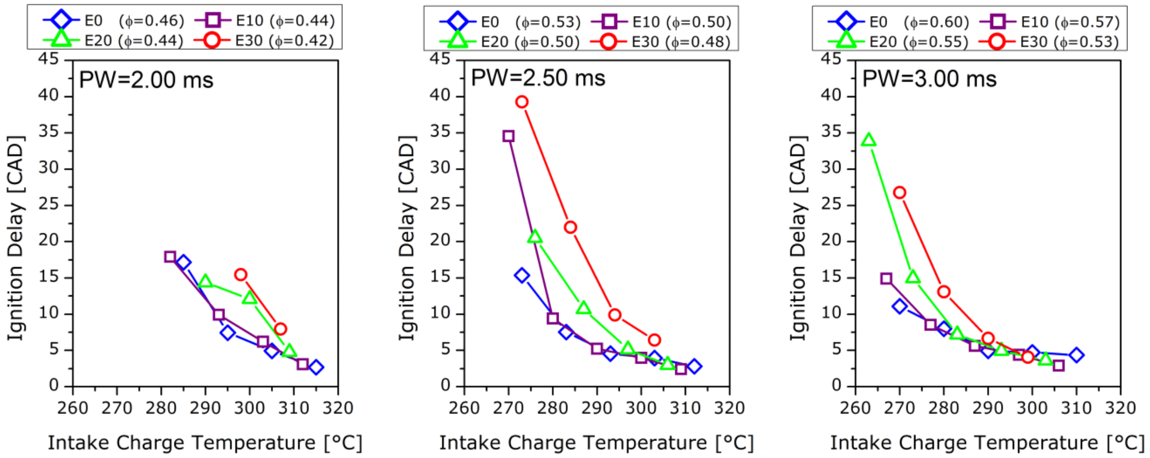

Figure 3-3. Estimated ignition delay times of indolene-ethanol blends as a function of intake charge temperature for three fuel injection pulse widths.

Effects of Fuel Blend for Constant End of Compression Temperature

As described earlier, in order to isolate the effects of fuel blends from temperature effects, additional experiments were designed to target the same end of compression temperature. This was achieved by setting the intake air temperature and fuel pulse width for each blend to achieve comparable end of compression temperatures anticipating the effects of charge cooling by fuel evaporation and the effects on the ratio of specific heats and compression heating. The temperature target for this study was T_{EOC} = 1150 K. The engine operating conditions and results are listed in Table 3-2. As seen in Table 3-2, the intake temperature varied from 570 K (E0, $\Phi = 0.43$) to 604 K (E30, $\Phi = 0.63$) over the range of conditions studied to maintain the target end of compression temperature. Similar to the previous data set, conditions with high intake temperatures and equivalence ratios resulted in extremely advanced ignition and high heat release rates and led to unacceptably high levels of NO_x emissions.

The experimental results for the average peak pressure and average phasing of the peak pressure as a function of the equivalence ratio are presented in Figure 3-4. As seen in the figure, increasing the ethanol content of the fuel blend reduces the peak pressure and retards the combustion phasing at same equivalence ratio, although the phasing data show relatively weak sensitivity to the fuel composition compared to Φ. Despite the pressure decrease, the higher ethanol content extends the lean limit of the stable HCCI.

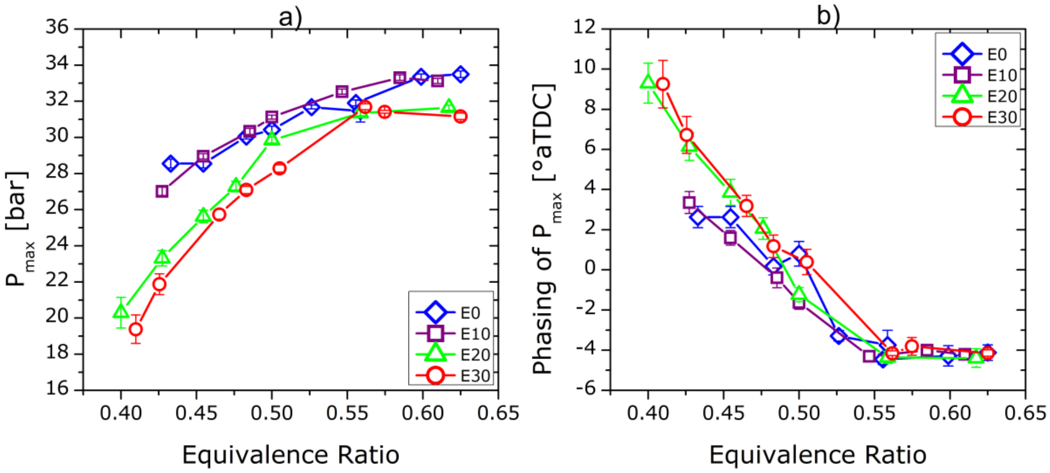

Figure 3-4. Experimental results for (a) average maximum in-cylinder pressure and (b) average phasing of the maximum pressure of indolene-ethanol blends as a function of equivalence ratio at TEOC=1150K

The engine $IMEP_n$ as a function of equivalence ratio, average in-cylinder peak pressure and CA50 are presented in Figure 3-5. The heat release rate as a function of equivalence ratio for the different blends is also presented in Figure 3-5. The IMEP values decrease as the ethanol content increases, with more significant differences observed between the fuel blends at lower equivalence ratios. The decrease in IMEP is despite having similar maximum heat release rates at equivalent values of Φ and Pmax is attributed to the retarded phasing that occurs with increasing ethanol content and lower Φs. As observed in the study of temperature effects, the IMEP results for the E10 blends are comparable to neat indolene.

Table 3-2. Engine operating conditions and performance results as a function of fuel blend for HCCI experiments targeting the same end of compression temperature.

Fuel	**Tin** [°C]	**PW** [ms]	**φ**	**NOx** [ppm]	**HC** [ppm]	**CO** [%]	**P_{max}** [bar]	**COV_{Pmax}** [%]	**θPmax** [CAD]	**HRR_{max}** [J/CAD]	**IMEP** [bar]	**COV_{IMEP}** [%]	**CA50** [CAD]
E0	322	3.36	0.63	4746	258	0.06	33.5	0.54	-4.1	78.55	1.37	4.53	-17.4
E0	318	3.15	0.60	3520	254	0.06	33.4	0.48	-4.3	74.22	1.40	3.33	-16.1
E0	315	3.01	0.56	986	347	0.15	31.9	0.51	-4.5	58.18	1.45	3.10	-12.2
E0	315	3.01	0.56	980	454	0.16	31.5	1.92	-3.7	51.43	1.45	3.63	-10.8
E0	310	2.66	0.53	302	345	0.15	31.7	0.33	-3.3	51.85	1.44	1.92	-9.3
E0	306	2.45	0.50	51	399	0.11	30.4	0.64	0.8	38.11	1.64	2.44	-3.4
E0	304	2.31	0.48	33	390	0.10	30.0	0.44	0.2	37.43	1.47	2.18	-4.3
E0	301	2.18	0.45	2	504	0.11	28.6	0.86	2.6	29.16	1.50	1.85	-1.6
E0	297	1.97	0.43	1	566	0.11	28.6	0.86	2.6	29.16	1.50	1.85	-1.6
E10	323	3.34	0.61	5013	257	0.06	33.1	0.42	-4.2	76.59	1.30	3.91	-17.7
E10	320	3.20	0.58	4137	412	0.06	33.3	0.45	-4.0	73.96	1.28	4.56	-17.6
E10	313	2.86	0.55	1174	266	0.09	32.5	0.44	-4.3	59.97	1.50	2.46	-12.1
E10	308	2.51	0.50	103	380	0.11	31.1	0.34	-1.6	42.32	1.57	1.46	-6.4
E10	305	2.37	0.49	39	416	0.11	30.3	0.54	-0.4	37.28	1.52	2.23	-5.0
E10	301	2.16	0.45	4	496	0.10	28.9	0.48	1.6	29.99	1.43	1.56	-3.0
E10	296	1.96	0.43	2	534	0.11	27.0	0.83	3.4	22.57	1.30	1.48	-1.0
E20	325	3.19	0.62	3904	325	0.10	31.6	0.43	-4.4	70.87	1.25	2.55	-16.4
E20	318	2.84	0.56	990	278	0.12	31.3	0.47	-4.4	58.01	1.27	3.45	-12.2
E20	311	2.50	0.50	52	379	0.10	29.9	0.56	-1.2	38.77	1.29	2.59	-6.0
E20	309	2.36	0.48	7	499	0.11	27.3	1.07	2.1	29.45	1.15	1.98	-2.0
E20	305	2.15	0.45	3	520	0.10	25.6	1.36	3.9	22.40	1.05	2.54	0.0
E20	300	1.95	0.43	2	660	0.13	23.3	1.84	6.1	16.67	0.90	1.89	2.5
E20	297	1.81	0.40	4	740	0.15	20.3	4.20	9.3	10.65	0.76	4.24	6.7
E30	331	3.34	0.63	4033	206	0.09	31.2	0.58	-4.1	69.86	1.16	3.74	-18.0
E30	324	3.00	0.57	1370	265	0.09	31.4	0.25	-3.8	58.92	1.31	1.98	-13.1
E30	324	3.00	0.56	1889	207	0.06	31.7	0.52	-4.2	62.50	1.16	3.28	-14.7
E30	316	2.66	0.51	20	406	0.16	28.3	0.73	0.4	35.86	1.27	2.29	-3.6
E30	313	2.52	0.48	4	589	0.12	27.1	0.75	1.2	30.21	1.13	1.86	-3.1
E30	309	2.31	0.47	1	584	0.12	25.7	1.05	3.2	23.77	1.05	2.02	-0.7
E30	304	2.11	0.43	1	802	0.15	21.9	2.63	6.7	14.49	0.80	2.59	3.7
E30	301	1.97	0.41	0	892	0.16	19.4	4.06	9.3	10.01	0.72	3.53	7.5

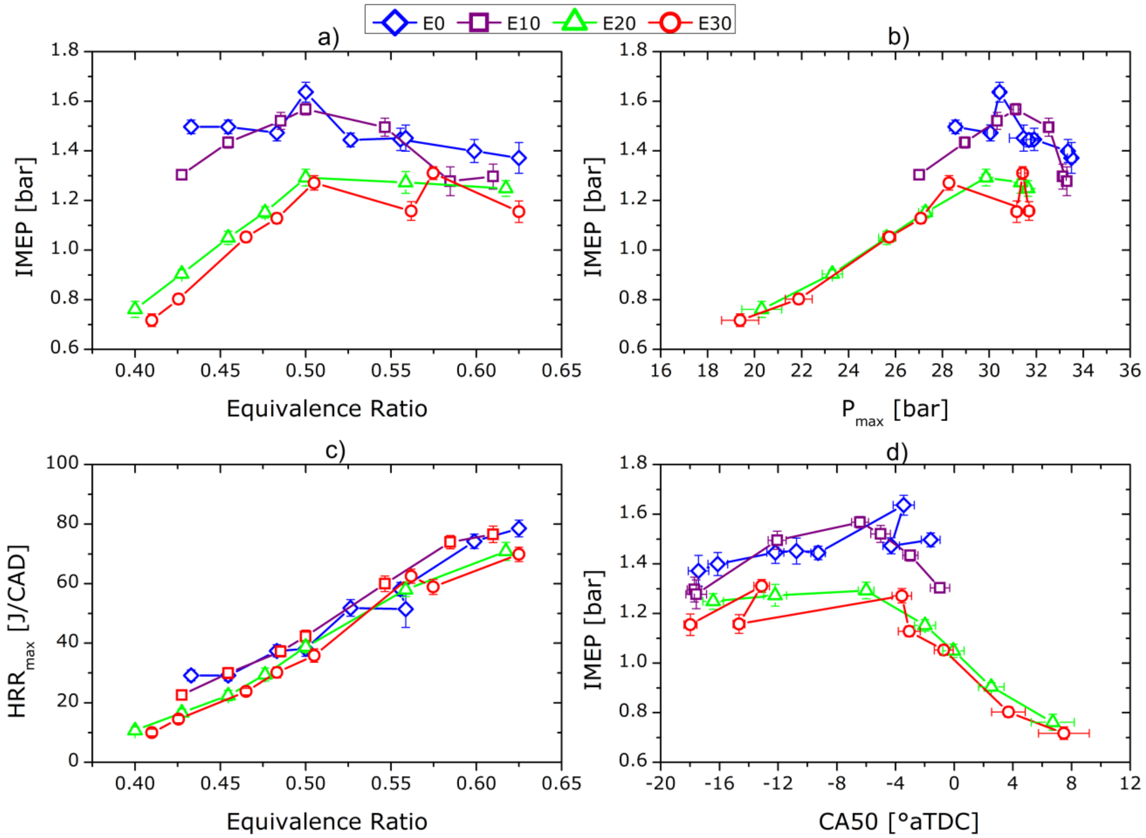

Figure 3-5. IMEP as a function of (a) equivalence ratio, (b) maximum average cylinder pressure and (d) phasing of the maximum average cylinder pressure; (c) maximum heat release rate as a function of equivalence ratio for indolene-ethanol blends at TEOC=1150K.

The heating value of ethanol is significantly lower than the heating value of indolene (LHV_{eth}=26.9 MJ/kg and LHV_{ind}= 44.4 MJ/kg), therefore the heating value decreases by approximately 15% for E30 compared to neat indolene. However, at the same equivalence ratio more fuel is injected to offset the fuel leaning effect of the ethanol. For example, at T_{intake}=573 K an increase of approximately 16% in fuel mass is needed for E30 compared to E0 to achieve Φ = 0.5, which results in a 2% increase in the energy content of the charge.

NO_x emissions levels as a function of equivalence ratio, maximum in-cylinder pressure and CA50 are shown in Figure 3-6. Hydrocarbon levels are also presented as a function of equivalence ratio in the figure. NO_x levels generally increase and HC levels decrease as equivalence ratio increases for all blends. Although NO_x emissions decrease with higher ethanol content of the fuel at the same equivalence ratio, HC emissions increase. The NO_x emissions show very weak sensitivity to the fuel composition as a function of equivalence ratio or CA50. However, for equivalent peak pressure, NO_x emissions are higher with higher ethanol content. The trends for maximum in-cylinder pressure are good global indicators of the trends for maximum in-cylinder temperatures, and the logarithmic dependence of the data support the hypothesis that the thermal NO_x mechanism dominates. The difference in NO_x emissions for equivalent P_{max} indicates that the higher ethanol content either causes local variations in the in-cylinder flow field or the chemical pathways are affected by increasing the ethanol in the fuel blend.

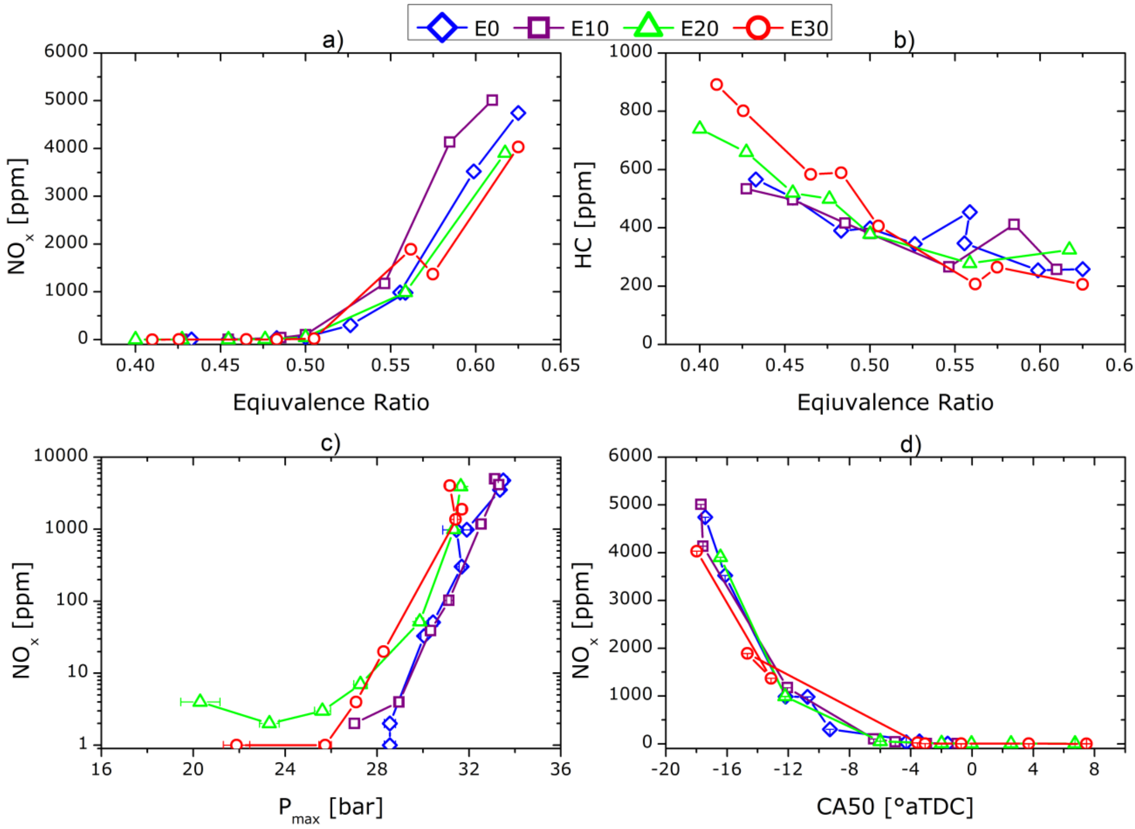

Figure 3-6. NO$_x$ emission as a function of (a) equivalence ratio, (c) maximum in-cylinder pressure, (d) phasing at the 50% of heat release; (b)HC emission as a function of equivalence ratio for indolene-ethanol blends at T_{EOC}=1150 K.

The trends in the engine data can be considered in the context of the model estimates for ignition delay. Figure 3-7 presents the estimates for ignition delay time [CAD] as functions of equivalence ratio, average peak pressure, maximum heat release rate and CA50. The ignition delay generally decreases for comparable P_{max}, HRR, and CA50 as the ethanol content increases. However there are conditions where there is weak sensitivity to the fuel composition; for example, higher equivalence ratios, higher heat release rates and higher maximum pressures.

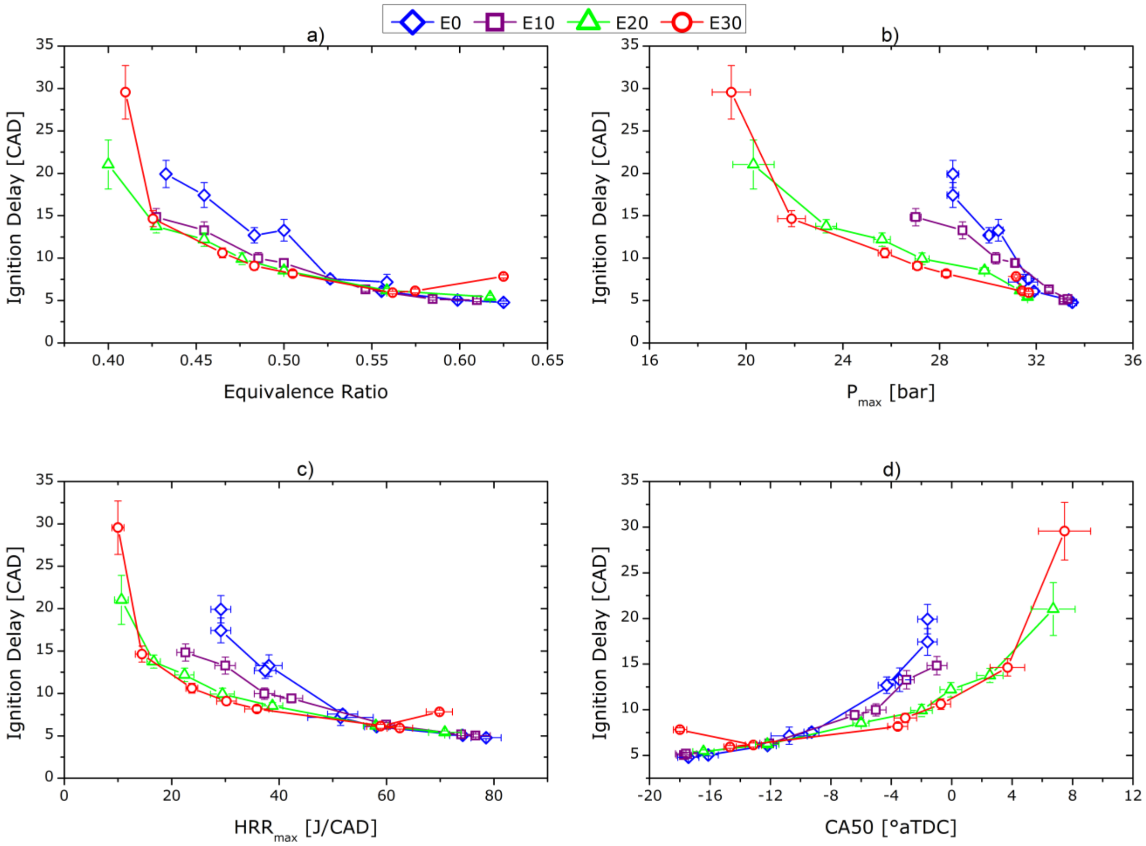

Figure 3-7. Ignition delay as a function of (a) equivalence ratio, (b) maximum in cylinder pressure, (c) maximum heat release rate, and (d) phasing of 50% of heat release for indolene-ethanol blends at T_{EOC}=1150K.

The results of the current work provided new information on the HCCI performance of ethanol/indolene fuel blends. Some of the observed trends are in good agreement with previous studies. For example, the current work agrees well with the previous work by Xie et al. [28] who also found the lean operating limit for HCCI was extended with increasing ethanol content in gasoline/ethanol blends. However, in the current work, extending the lean limit was only observed after anticipating and compensating for the evaporative cooling effects of the ethanol.

Contrary to the study by Gnanam et al. [27] where some ethanol blends advanced ignition, ignition timing was systematically retarded, with lower peak pressures, with higher ethanol content in this study even for the experiments targeting the same end of compression temperatures. Moreover, the effects of ethanol on engine performance were often non-linear, such as the impact of ethanol on indicated thermal efficiency. The first order effect of ethanol on indolene/gasoline fuel blends during HCCI operating is thermal, i.e. dominated by the evaporative cooling requirements of the ethanol; however, the results of the current work support that the chemical and physical properties of ethanol are also apparent on the key performance metrics of power, efficiency and emissions.

3.4 Conclusions

The results of this experimental study support the following conclusions regarding the effects of indolene-ethanol blends on engine performance during HCCI operation of single cylinder engine.

- Higher ethanol content in the fuel blends limits the stable HCCI operation to higher intake temperatures due to the effects of ethanol on lowering charge temperatures (due to a combination of charge cooling and lower compression heating).
- When compensating for the effects of charge cooling (e.g. increasing air preheat), increasing the ethanol content of the fuel blend can extend the stable HCCI lean operating limit.
- E10 blends can perform comparably to neat indolene in terms of power and stability; however, lower equivalence ratios are required with E10 blends compared to E0 to maintain low NO_x emissions.
- Increasing ethanol content of the fuel blends did not systematically improve or reduce engine stability in terms of cycle-to-cycle variation regardless of the compensation for end of compression temperatures.
- The model used to estimate the ignition delay time of the fuel blends reproduces the experimentally observed trends for the tested mixtures and engine conditions, indicating the model can be used to develop fuel blend strategies at similar conditions using either active or passive control of charge cooling effects.

Chapter 4
Spark Assisted-HCCI

4.1 Objective

The objective of this work was to compare the effects of spark assisted HCCI on the ignition and combustion properties of 100% indolene and 70% indolene/30% ethanol blends. This blend ratio was used because of the significant chemical effects of blends observed around this blend ratio [64]. A challenge of isolating fuel effects of ethanol blends on HCCI and SA-HCCI studies is the high enthalpy of vaporization of ethanol compared to gasoline [65]. In the previous chapter it was shown that the temperature effects can dominate the HCCI behavior. In this work, the experimental method was designed to minimize the effects of temperature by controlling the air preheat to achieve the same end of compression temperature for both fuels. High-speed imaging of the combustion chamber was used to identify the relationship between engine performance metrics and the location and propagation rate of flames initiated by the spark for the fuels at different stoichiometries.

Most of the content of this chapter has been published in the proceedings of the ASME 2013 ICED [66].

4.2 Experimental Approach

This study was conducted using the PFI single cylinder optical research engine facility of the University of Michigan, which is described in section 2.1.

Fuel equivalence ratio was controlled by varying the pulse width of the fuel injector driver, holding fuel pressure constant at 25 psi. Equivalence ratio was measured using a lambda sensor located in the exhaust, which is described in Section 2.3. All experiments in this study used unthrottled air with the fuel injection pulse width varied to control the overall equivalence ratio of the fuel/air mixture. No external EGR was used for the experiments and the internal EGR for the engine at the specified valve timing was estimated to be less than 8%. With the air flow fixed, higher equivalence ratios yielded higher engine loads. Nitrogen oxides (NOx), carbon monoxide (CO) and unburned hydrocarbon (UHC) emissions were measured using the exhaust gas analyzer. The exhaust gases were sampled from the exhaust manifold approximately 3 cm from the exit of the exhaust valves.

In this study, the engine operating conditions were controlled to minimize differences in the bulk temperature of the fuel/air charge between the two fuels. Specifically, the intake air temperature was controlled to target the same bulk or average temperature at the end of compression for each fuel based on the thermocouple measurement of the intake air temperature, the fuel composition and the energy required to vaporize the fuel. The process to set the air preheat temperatures has been described in detail in Section 3.2. Differences in the heat transfer of the charge in the intake manifold that occur due to the different fuel blends were not considered in the control algorithms. Fuel was injected very early onto a closed intake valve, at top dead center (TDC) during the compression stroke of the preceding cycle, to assist fuel vaporization and mixing with the intake air.

The baseline fuel was indolene, a reference grade gasoline (EPA Tier II EEE: US Federal Emission Certification Gasoline), and it was blended with anhydrous ethanol to produce a 30% ethanol/70% indolene volumetric blend. The properties of the fuels are shown in Table 4-1.

Table 4-1. Fuel properties of E0, E30 and E100.

Fuel Property	**E0/indolene**	**E30**	**E100/ethanol**
Density [kg/m^3]	0.755	0.765	0.789
Kinematic viscosity [cSt]	0.67–0.84	0.97	1.36–1.57
Latent heat [kJ/kg]	380.5	547.1	919
Latent heat/kg mixture @ stoich. [kJ/kg mixture]	24.36	39.42	91.9
Lower heating value [MJ/kg]	44.41	39.01	26.94
Stoichiometric AFR (mole basis)	14.62	12.88	9
H/C (mole basis)	1.88	2.12	3
O/C (mole basis)	0	0.11	0.5
Flammability Limits @25°C [vol%] [67]	1.2–7.1	–	3.3–19
Lean flammability limit (ϕ_L) @ 25°C	0.62	–	0.50
Minimum Autoignition Temperature [°C] @ 1 atm [67]	470	–	365

4.3 Image processing

The combustion chamber was imaged through the piston window using a high-speed color digital video camera (Vision Research Phantom v7.1, color). A fast 50 mm lens (f/0.95 Nikkor TV lens) and C-mount extension tubes were used with the camera to adjust the focal length and to reduce the focal depth along the cylinder axis. In this study, the camera was focused at a plane coinciding with the spark plug ground electrode. Visible chemiluminescence emission was recorded at 3000 frames per second (fps) with 309 µs exposure time and 320 x 320 pixels resolution. No additional spectral filters were used other than the inherent spectral characteristics of the camera and the supporting optics. Emission in the visible wavelength region from hydrocarbon and ethanol flames is generally attributed to chemiluminescence of C_2, CH, CHO, and OH [68]. C_2 and CH are short-lived intermediate species which are considered indicators of high temperature reaction zones.

As noted earlier, the diameter of the piston window was 48.5 mm, which partially occluded the valves. Recall, the total piston diameter was 71.9 mm. Thus, 45.5% of the projected area of the combustion chamber was imaged near TDC. Camera images were time sequenced to a common trigger signal with the in-cylinder pressure data. The imaging data were synchronized with the pressure data with an uncertainty of ~ 1–2 CAD.

The imaging data were used to quantify some of the in-cylinder features such as flame initiation and propagation prior to autoignition in SA-HCCI mode. Two methods for image processing were used to analyze the different combustion characteristics. As the piston moved the field of view changed, but the magnitude of change in field of view near TDC was negligible.

In the first method, the color images were converted from three red/green/blue (RGB) hexadecimal matrices to a single binary (monochrome) matrix by applying a threshold. The pixels with brightness values above the threshold were defined as white, while pixels below the threshold were defined as black. Then all the white pixels were counted to form an equivalent area using a constant radius disc for each frame. The rate of change of the disc radius was used as an estimate of flame speed. A detailed description of this image processing method can be found in [69], and an example of the image processing steps is shown in Figure 4-1. The green circle represents the limit of the viewing area through the transparent window insert of the piston. The threshold used for this case was 1%. Keros et al. [70] explored the sensitivity of the image analysis to the image intensity, contrast and threshold values. Nominal settings for the image values were used in this work based on the results of Keros et al. [70].

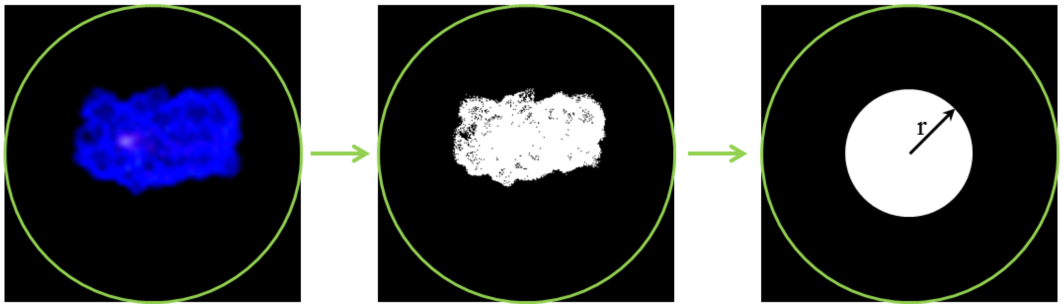

Figure 4-1. Example of one of the imaging processing methods used in the current work. From left to right: 1. The original color image, with color enhanced for clarity; 2. The image after conversion to monochrome; and 3. The equivalent area of the monochrome image represented as a disc.

The rationale for approximating the projected area of the flame as a circle or disc is based on previous imaging studies using the same engine in HCCI and SA-HCCI operating modes. In Zigler et al. [32], manual analysis of the HCCI and SA-HCCI images was used. The location of the flame front was measured along fixed polar coordinates for each frame. Such methods were time consuming, and consequently, a small subset of the imaging data were characterized quantitatively in the study. While not always circular, the results showed the flame shapes formed during SA-HCCI operation were typically irregular ovals, with no statistically preferred orientation or direction of propagation. Thus, the flame shapes were approximated as discs in the current work to simplify and expedite automated image analysis.

The timing of autoignition in spark assist experiments was detected using the maximum of the first derivative of the radius data ($dR/d\theta|_{max}$) in each combustion cycle. To validate this approach, visual detection of the autoignition event was done for multiple cycles of experimental conditions and the uncertainty was within the bounds of the frame rate precision (1–2 CAD).

As seen in the original color frame image presented in Figure 4-1, there were areas with higher chemiluminescence intensity than the others, but the application of the threshold eliminates differences in intensity and spatial features are not retained with this method. Therefore, a second method was used to quantify the chemiluminescence intensity and to study the spatial features of ignition and combustion. In the second method, the color images were converted to grey scale with an associated intensity value for each pixel. A low pass filter was applied to the images. An intensity range of 0-5 (arbitrary units) was selected for the filter as this intensity range resulted in good resolution of the local features of the flames initiated by the spark plasma. All pixels with values above the threshold were reset to the maximum value, and a false color scale was applied to the intensity range of 0 (blue) to 5 (red). The images were averaged over the 30 combustion cycles at the same crank angle to generate time histories of average intensity maps. The image processing steps for method 2 are shown in Figure 4-2.

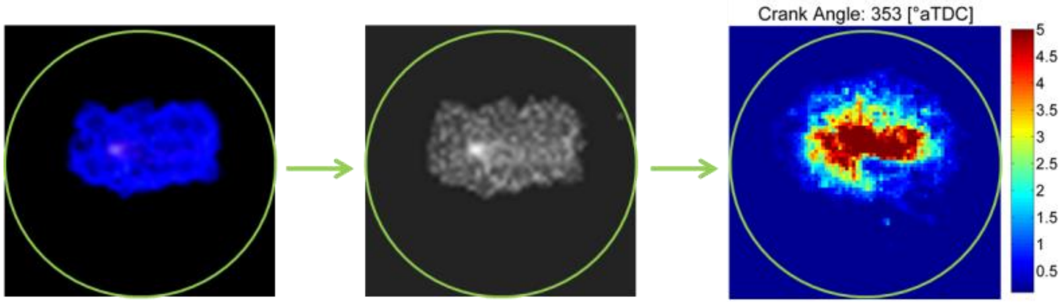

Figure 4-2. Example of the second image processing method used in the SA-HCCI imaging study. From left to right: 1. The original color image, with color enhanced for clarity; 2. The image after conversion to grey scale; and 3. The result of averaging the intensity values of 30 consecutive combustion cycles at the same crank angle after applying a low pass filter to the intensity. The range of the false color scale is 0 to 5 [a.u.].

The spatially integrated value of the average intensities was also determined; providing a single numerical metric for each frame during the ignition and combustion time histories. The spatially integrated chemiluminescence (SIC) was of interest for comparison with the heat release rate determined from the pressure data.

4.4 Experimental Results

Engine Performance

For each experiment, the fuel injection pulse width was set to target equivalence ratios from $\phi = 0.4$ to 0.5. The air preheat was then adjusted based on fuel composition to achieve the same end of compression temperature of $T_{EOC} = 1085$ K for all the experiments. The lower heating value of the ethanol blends required more mass and therefore longer pulse durations compared to indolene at the same equivalence ratio (e.g. at $\phi = 0.50$ the injection pulse width for E30 was ~14% longer than the fuel pulse width for indolene). However, the total energy of the fuel/air charge was within 3% between the E0 and E30 for all conditions. The air preheat temperatures and fuel pulse width data are provided in Table 4-2.

At each equivalence ratio HCCI, SA at 20° bTDC (SA20), 40° bTDC (SA40) and 60° bTDC (SA60) conditions were studied. The spark assisted conditions were only executed if the phasing of the in-cylinder peak pressure (θ_{Pmax}) was after TDC. Experiments with higher equivalence ratios were also performed ($\phi = 0.6$), but at the targeted end of compression temperatures, the high equivalence ratio conditions resulted in knocking and unacceptable NO_X emission levels. Consequently, the $\phi = 0.6$ conditions represented the upper bound of acceptable HCCI operating conditions for this engine at the level of preheat considered.

Imaging, pressure, and emissions data were collected for 5 seconds at each condition. The in-cylinder pressure time histories were analyzed to determine the maximum cylinder pressure (P_{max}), phasing of maximum cylinder pressure (θ_{Pmax}), heat release rate (HRR), phasing or crank angle timing of 50% of heat release (CA50), and net indicated mean effective pressure ($IMEP_n$). The experimental results are reported in Table 4-2 and Table 4-4 where the values are averaged over ~30 cycles for experiments conducted at 700 RPM and ~50 cycles for 1200 RPM experiments. The coefficient of variation (COV) or standard deviation (σ) of each metric are also reported.

Figure 4-3 presents the results for P_{max}, and $\theta_{Pmax.}$ The experiments were performed at 700 RPM for each fuel targeting three equivalence ratios (ϕ = 0.40, 0.45 and 0.50). The error bars are the standard deviations of the data and represent the cycle-to-cycle variation. The fuels exhibited similar changes in peak pressure and phasing as a function of ϕ. However, E30 yielded consistently higher average peak pressures compared to indolene. Spark assist at 40^{o} bTDC advanced peak pressure compared to HCCI at all conditions for both fuels. Spark assist at 20^{o} bTDC advanced peak pressure at some conditions, and reduced cycle-to-cycle variability at some conditions.

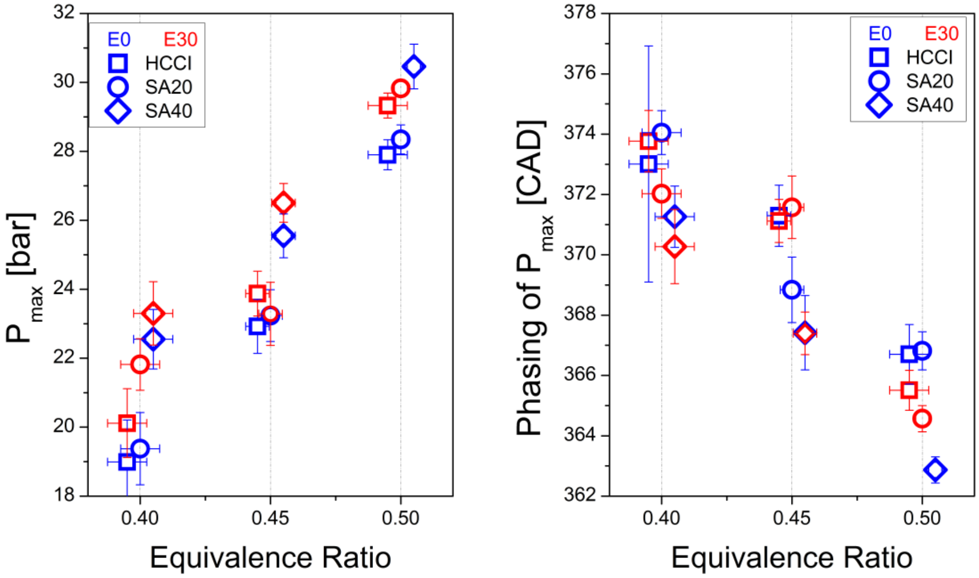

Figure 4-3. Average maximum in-cylinder pressure and average phasing of P_{max} as a function of ϕ. The data have been offset from the nominal ϕ values for clarity. The error bars are the standard deviations of the measured data

The peak pressure was more sensitive to spark assist at lower equivalence ratios. At higher equivalence ratios, combustion was more stable in the HCCI mode, and introduction of the spark did not positively or adversely affect the combustion stability. On the other hand, the introduction of spark at the leaner conditions improved combustion and advancing spark assist increased P_{max} nonlinearly. This is consistent with the observations made by Hyvönen et al. [29] and Manofsky et al. [71] in their studies of spark assisted HCCI using gasoline.

Table 4-2. Experimental results for engine and emission of HCCI and SA-HCCI data at 700 RPM.

Fuel	HCCI/SA	ϕ	P_{max}	COV_{Pmax}	$IMEP_n$	COV_{IMEPn}	CA50	σ_{CA50}	T_{in}	PW_{fuel}	E_{cycle}	NO_x	UHC	CO
-	[°bTDC]	-	[bar]	[%]	[bar]	[%]	[°aTDC]	[°aTDC]	[°C]	[ms]	[J]	[ppm]	[ppm]	[%]
E0	HCCI	0.50	27.90	1.56	1.48	9.9	362.4	0.89	266	251	239	1	407	0.12
E30	HCCI	0.50	29.33	1.24	1.94	1.6	360.6	0.76	272	284	235	0	566	0.11
E0	SA20	0.50	28.35	1.48	1.67	2.4	362.3	0.59	266	251	239	3	445	0.12
E30	SA20	0.50	29.83	0.85	1.94	1.4	359.7	0.50	272	284	235	3	557	0.11
E0	SA40	0.50	30.46	2.13	1.24	8.3	358.5	0.74	266	251	239	4	363	0.11
E0	HCCI	0.45	22.92	1.46	1.38	5.2	364.7	1.14	260	216	225	3	565	0.16
E30	HCCI	0.45	23.88	3.41	1.73	2.2	366.6	0.84	264	229	219	1	688	0.14
E0	SA20	0.45	23.24	2.72	1.15	3.1	364.7	1.22	260	216	225	5	522	0.16
E30	SA20	0.45	23.29	3.23	1.68	2.2	367.3	1.31	264	229	219	2	717	0.13
E0	SA40	0.45	25.55	3.93	1.29	10.5	362.8	1.27	260	216	225	2	499	0.14
E30	SA40	0.45	26.50	2.49	1.68	1.5	362.3	0.83	264	229	219	3	638	0.13
E0	HCCI	0.40	18.99	2.12	1.25	10.6	372.1	2.14	256	195	207	6	899	0.23
E30	HCCI	0.40	20.12	6.42	1.45	3.9	370.4	1.42	261	202	211	3	883	0.19
E0	SA20	0.40	19.38	4.96	1.35	6.7	371.4	1.41	256	195	207	5	860	0.22
E30	SA20	0.40	21.82	5.40	1.51	2.7	367.9	1.02	261	202	211	0	746	0.17
E0	SA40	0.40	22.55	3.43	1.47	2.4	367.2	1.24	256	195	207	4	652	0.17
E30	SA40	0.40	23.30	3.83	1.50	2.1	365.8	1.49	261	202	211	0	675	0.15
E0	SA60	0.40	23.19	5.10	1.41	2.5	366.1	1.77	256	195	207	2	635	0.16
E30	SA60	0.40	25.36	2.78	1.49	1.7	362.5	1.23	261	202	211	1	650	0.13

Figure 4-4 presents the results for combustion phasing, $IMEP_n$, and thermal efficiency as a function of spark assist timing for the two fuels at the different equivalence ratios. The $IMEP_n$ values were systematically higher for the E30 blend. This is the result of the higher P_{max} and higher heat release rates. The higher $IMEP_n$ levels for E30 were coupled with significantly lower variability (i.e. lower COV_{IMEPn}) despite the fact that similar COV values were observed for the combustion phasing of both fuels. The results for thermal efficiency separated the performance of two fuels further, with E30 outperforming E0 at all conditions except the SA40, $\phi = 0.4$ operating point.

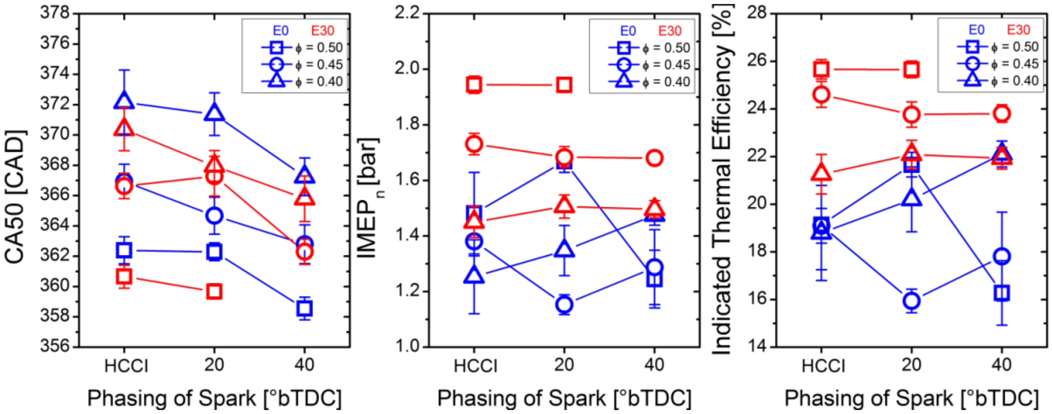

Figure 4-4. Experimental results of the effects of SA on CA50, $IMEP_n$ and the indicated thermal efficiency of the two fuel blends at 700 RPM. The error bars are the standard deviations for the cycle averaged data.

The differences in the performance of E30 compared to E0 at 700 RPM are attributed to changes in thermal stratification created by the differences in the fuel spray characteristics. Chemistry is not considered a factor, as ethanol blends have been shown to have slower ignition kinetics compared to iso-octane [72], which is expected to be less reactive than indolene. As noted earlier, the E30 blends required longer injection duration due to the lower energy content of ethanol, which may have considerable impact on the fuel/air and thermal mixing of the charge. Differences in the level of air preheating used may also introduce differences in the local temperature field in-cylinder. At the higher engine speed (data presented below), the differences between the E0 and E30 $IMEP_n$ and thermal efficiency data are significantly reduced, indicating that increased turbulence is counteracting the beneficial flow conditions created by the E30 at lower engine speeds.

The emissions data are provided in Table 4-2. UHCs were systematically reduced as ϕ increased from ~900 ppm to less than 600 ppm for both fuels. SA improved UHC emissions at the most lean operating conditions, but otherwise had little effect on UHC or CO emissions. The same trend was observed at the high engine speed conditions. For all the experimental conditions, NO_X emissions were at single digit [ppm] levels and no significant changes were observed between the operating conditions.

The leanest conditions of ϕ=0.40 are considered in greater detail in Figure 4-5. The retarded combustion phasing of these conditions enabled a larger range of advanced spark timings. Normalized pressure, heat release rate, and mass fraction burned are presented in the figure as a function of SA timing for both fuels. In Figure 4-5, the SA pressure data are normalized to the HCCI conditions of each fuel to demonstrate the sensitivity to SA. Combustion phasing advanced progressively for each advanced spark timing, and the combustion phasing of E30 was more advanced compared to equivalent SA timing of E0.

As seen in Figure 4-4, the two fuels exhibited different sensitivity to SA. For example, the E0-SA20 data led to a small increase in peak pressure and little change in combustion phasing, HRR, and mass fraction burned compared to the base case E0-HCCI, whereas E30-SA20 led to significant shifts from the E30 HCCI baseline peak pressure, combustion phasing, HRR, and mass fraction burned. Comparing the effects of SA60 for the two fuels, E30 still exhibited strong sensitivity to the change in spark timing, whereas

E0 showed little change in peak pressure, combustion phasing, HRR and mass fraction burned compared to SA40. In summary, the E0 exhibited more non-linear and less responsive behavior compared to E30 at these lean conditions. This may be due in part to the wider flammability limits of ethanol compared to gasoline (see Table 4-1). SA at 60° bTDC may be approaching the local flammability limit, where E30 may be capable of sustaining flames at these cooler conditions during the cycle.

Another observation based on the results presented in Figure 4-5 is the similarity of the E0-SA60 and E30-SA40 in heat release rate data. The results indicate SA can be used to compensate for the differences in fuel properties to match the heat release rate and combustion phasing of another fuel.

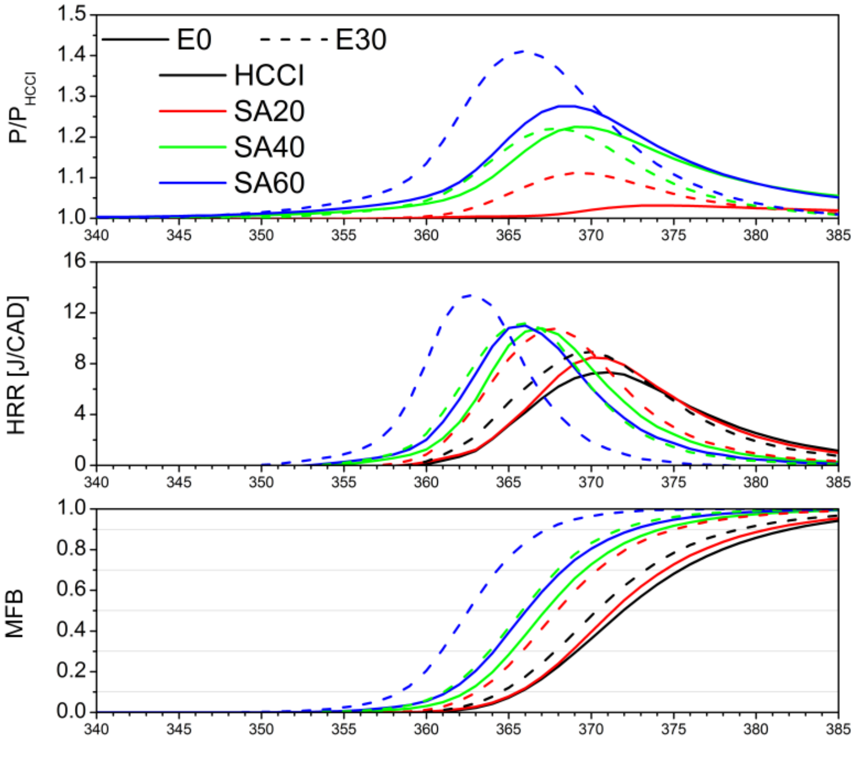

Figure 4-5. Normalized pressure, heat release rate, and mass fraction burned as a function of SA timing and fuel for $\phi = 0.4$.

Cycle-to-cycle Variation

Analysis of the engine and imaging data was performed to identify if there were features in the imaging data that could be linked to cycle-to-cycle variability in the combustion performance. Figure 4-6 shows the results for the time histories of the effective radius determined from the imaging data and of the HRR determined from the in-cylinder pressure data. All cycles for the E30-SA60, $\phi=0.40$, 700 RPM condition are presented. The cycles with the lowest (cycle 7) and highest (cycle 10) HRR_{max} as well as the two cycles between these limiting cases are highlighted in the figure. Autoignition is indicated by rapid and large increases in effective radius and HRR. Autoignition is well synchronized between the results and starts around 358^o for this condition. The flame propagation phase that occurs after spark ignition and before autoignition is characterized by the moderate increase in the effective radius data that occurs between approximately 340^o and 357^o. The effective radius data indicate flames were initiated and propagated for all conditions. Comparing the effective radius and the HRR data clearly indicates negligible heat release occurred during the flame propagation phase. The results indicate the compression heating of the unburned charge by the flames was sufficiently small that the compression heating was a negligible contribution to the pressure time history and thereby a negligible contribution to the HRR. (Note the direct energy injected by the spark is generally considered negligible relative to the energy of the fuel/air charge which these data confirm.) However, the compression heating is sufficient to accelerate autoignition by several CAD compared to HCCI (by as much as ~5 CAD for 700 RPM and ~10 CAD for 1200 RPM).

Figure 4-6 further shows that although there is some range in the timing of when flames first become observable in the imaging data, the start of flame propagation does not appear to be linked with maximum HRR. For example, even though flame propagation started later in cycle 7 compared to cycle 10, cycle 7 had a higher indicated flame speed (assuming dR/dt is an indicator of flame speed). Further, there are cycles where flame propagation started much later than cycle 7 and which had lower indicated flame speeds; yet these cycles also had higher maximum HRRs compared to cycle 7. Further, considering the two consecutive cycles 7 and 8, cycle 8 started flame propagation much earlier, but the combustion phasing was similar to cycle 7. So while the effective radius and HRR data were well correlated with the timing of autoignition, the flame portion of the effective radius data, specifically the start of flame propagation and the rate of flame propagation, did not correlate with HRR_{max} and the phasing of HRR. This conclusion may be due to the lack of spatial fidelity of the effective radius data, as discussed next.

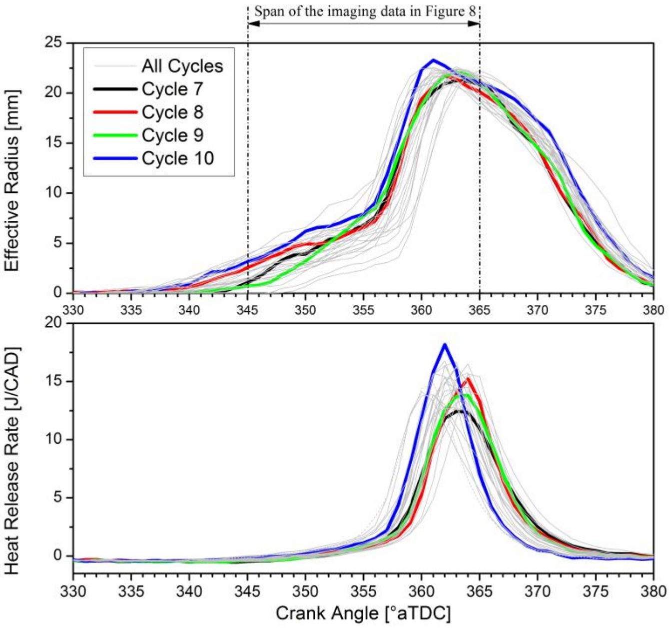

Figure 4-6. Cycle-to-cycle variation of effective radius and heat release rate for E30-SA60 and ϕ=0.40 at 700 RPM. Cycles 7 and 10 exhibited the minimum and maximum HRRs at these operating conditions, respectively.

The imaging maps provide spatially and temporally resolved information about spark ignition, autoignition and flame propagation, and the imaging maps were also evaluated to determine links between the local ignition and combustion events and the HRR and IMEP data. Figure 4-7 presents the chemiluminescence maps corresponding to the data presented in Figure 4-6 for cycles 7-10. Recall, cycles 7 and 10 exhibited the minimum and maximum HRRs at these operating conditions. When the images of cycles 7 and 10 are compared, it would appear that the high heat release rate of cycle 10 might be due to flame spread across a larger projected area of the combustion chamber, compared to the more compact flame formed during cycle 7. However, the images from the intermediate cycles 8 and 9 show similar flame progress to cycle 10 with lower HRR_{max}. Thus, the geometric features of the flame do not appear to correlate well with HRR_{max} and the phasing of HRR for these operating conditions. However, the image maps do provide insight into engine stability as discussed next.

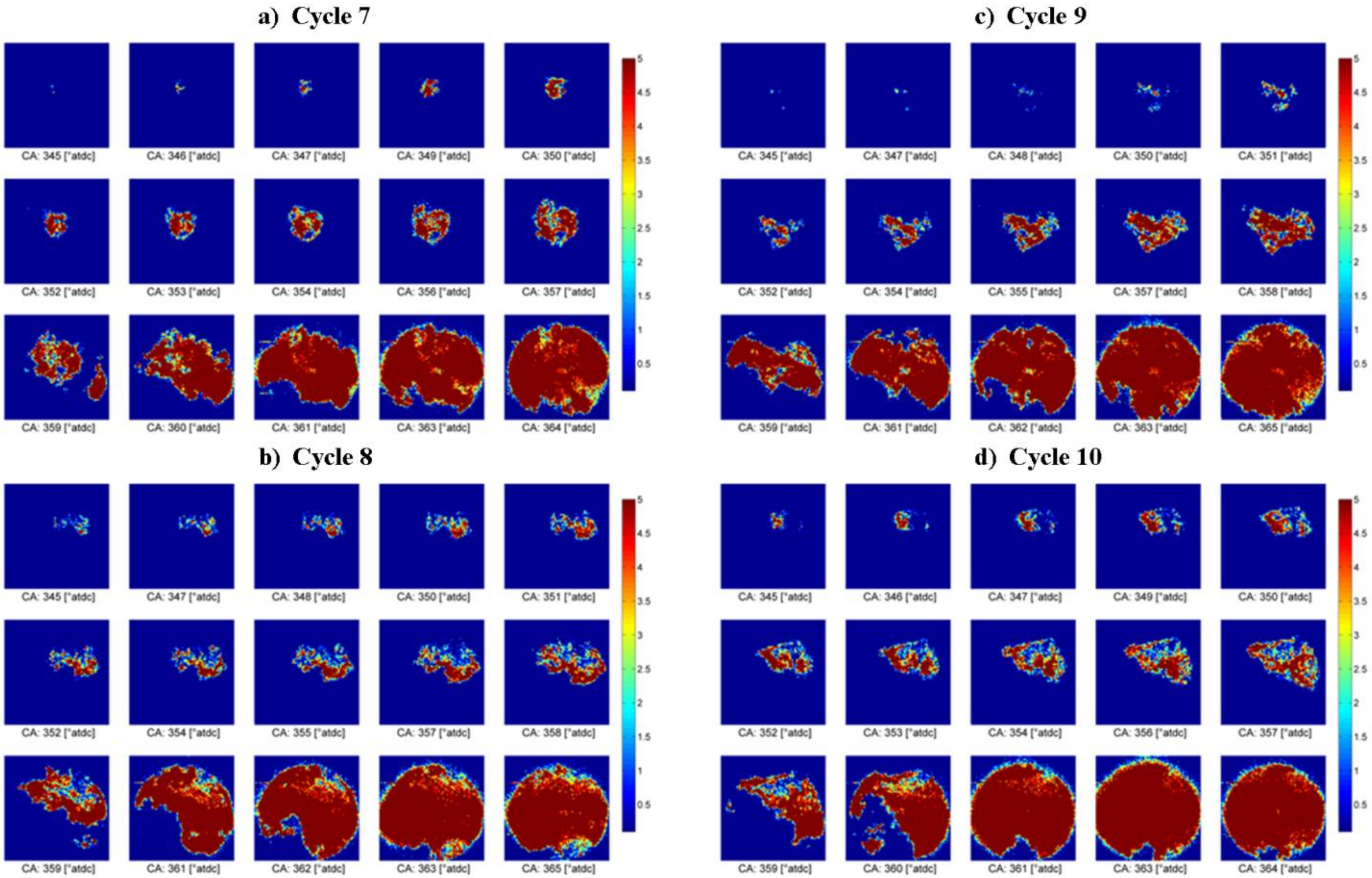

Figure 4-7. Results of imaging data from four cycles for E30 with SA at 60° bTDC and $\phi = 0.40$ at 700 RPM. Results for cycle 7 with $IMEP_n = 1.46$ bar and $HRR_{max} = 12.6$ J/CAD are presented in (a), results for cycle 8 with $IMEP_n = 1.49$ bar and $HRR_{max} = 15.2$ J/CAD are presented in (b), results for cycle 9 with $IMEP_n = 1.49$ bar and $HRR_{max} = 14.0$ J/CAD are presented in (c), and results for cycle 10 with $IMEP_n = 1.52$ bar and $HRR_{max} = 18.2$ J/CAD are presented in (d).

As seen in Figure 4-4, SA decreased the engine stability, i.e. increased the COV of $IMEP_n$, of E0 at some conditions. Figure 4-8 shows the chemiluminescence intensity maps for two cycles for E0 with SA at 40° bTDC and $\phi = 0.45$. The average $IMEP_n$ for the experimental condition was 1.29 bar with an unacceptable COV of 10%. Cycles 8 and 27, with $IMEP_n$ values of 1.43 bar and 1.03 bar respectively, highlight the variability in the imaging characteristics associated with the variability in $IMEP_n$. In both cycles, the first local autoignition site was observed at 360° aTDC (highlighted in the figures).

In cycle 8, the first local autoignition site was located at 4 o'clock, and global autoignition did not happen until ~4 CAD later, resulting in CA50 = 364.0° aTDC. In cycle 27, the first local autoignition sites were located at 4 and 9 o'clock positions and global autoignition happened much earlier compared to cycle 8, resulting in CA50=361.0° aTDC. The presence of multiple autoignition sites is associated with higher rate of heat release in cycle 27; however, it is not clear if the additional autoignition sites are the cause or the effect of higher heat release rates.

a) Cycle 8

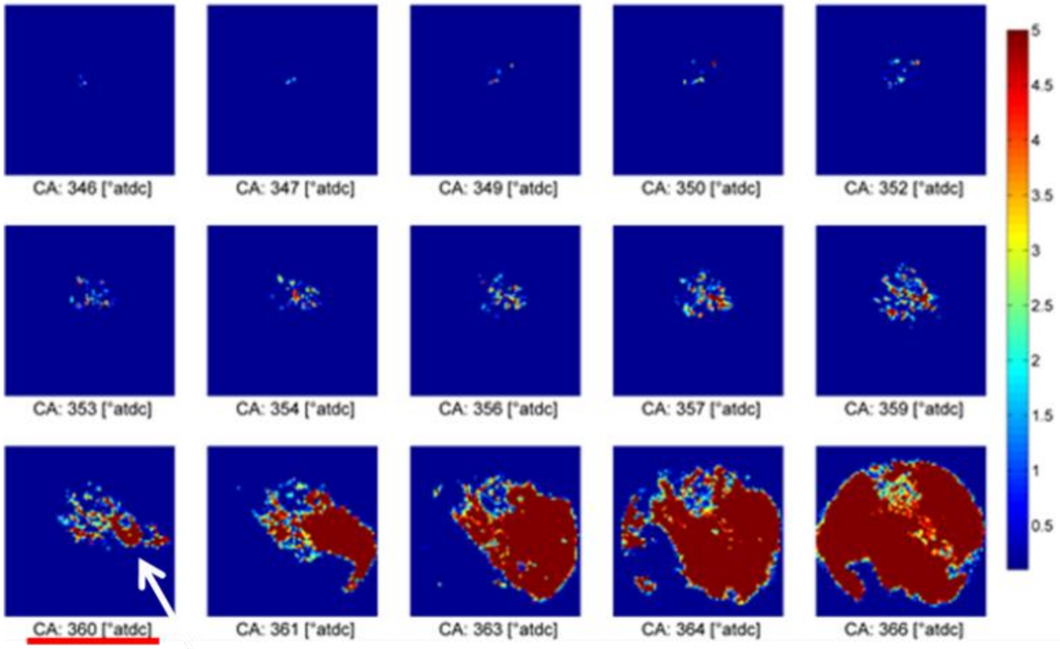

b) Cycle 27

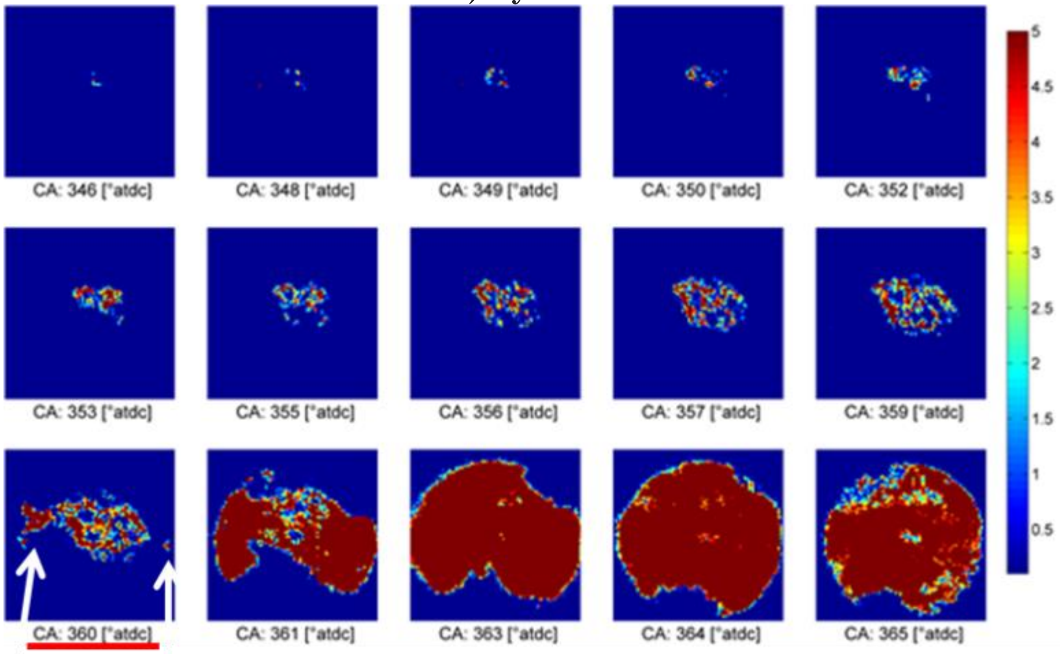

Figure 4-8. Results of imaging data from two cycles for E0 with SA at 40° bTDC and ϕ=0.45 at 700 RPM. Results for cycle 8 data with $IMEP_n$ = 1.43 bar and HRR_{max} = 15.1 J/CAD are presented in (a), and results for cycle 27 data with $IMEP_n$ = 1.03 bar and HRR_{max} = 20.2 J/CAD are presented in (b). The location of the first local autoignition sites are highlighted in the panels.

In contrast to E0, E30 exhibited low COV for IMEP$_n$ (COV$_{IMEPn}$=1.5%) at SA of 40° bTDC and ϕ = 0.45. Figure 4-9 shows the chemiluminescence intensity map for a typical cycle of E30. The main difference between the imaging data of the two fuels is the initiation of a more well defined flame structure which also occurred earlier after the spark discharge for E30. The more robust flame structure for E30 may be due to the wider flammability limits of ethanol compared to gasoline (see Table 4-1). The more well-defined flame structure may be due in part to higher chemiluminescence signals due to the higher densities of the E30 results. As seen in Figure 4-8, local autoignition sites were also observed for E30 immediately prior to global autoignition.

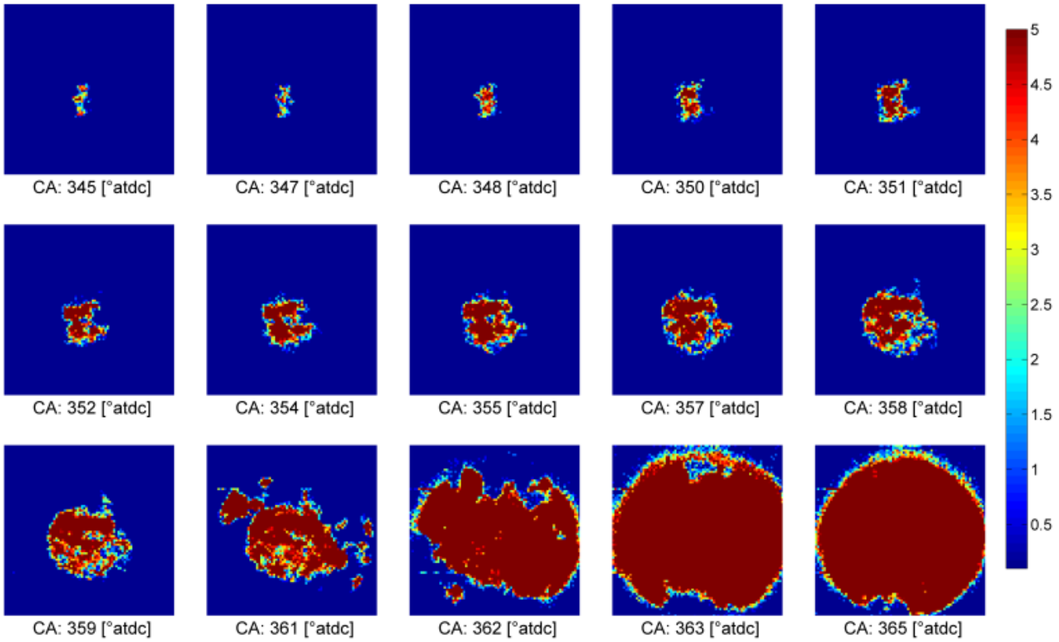

Figure 4-9. Results of imaging data from for E30 with SA at 40° bTDC and ϕ=0.45 at 700 RPM for cycle 10 with IMEP$_n$ = 1.75 bar and HRR$_{max}$ = 19.6 J/CAD.

Cycle Averaged Results

Imaging results for the averaged time histories are presented in Figure 4-10 for a baseline HCCI operating condition for E0 and ϕ=0.45 at 700 RPM. In HCCI mode, both fuels consistently started autoignition at the 3 and 9 o'clock locations of the combustion chamber near the outer radius of the imaging area and between the two valves. The data indicate a butterfly pattern due to the temperature stratification in the combustion chamber of this engine, which has been observed previously by Zigler et al. [7,15]. As seen in Figure 4-10, the local autoignition zones started at ~362° aTDC and after a few crank angle degrees, global autoignition occurred at ~366° aTDC.

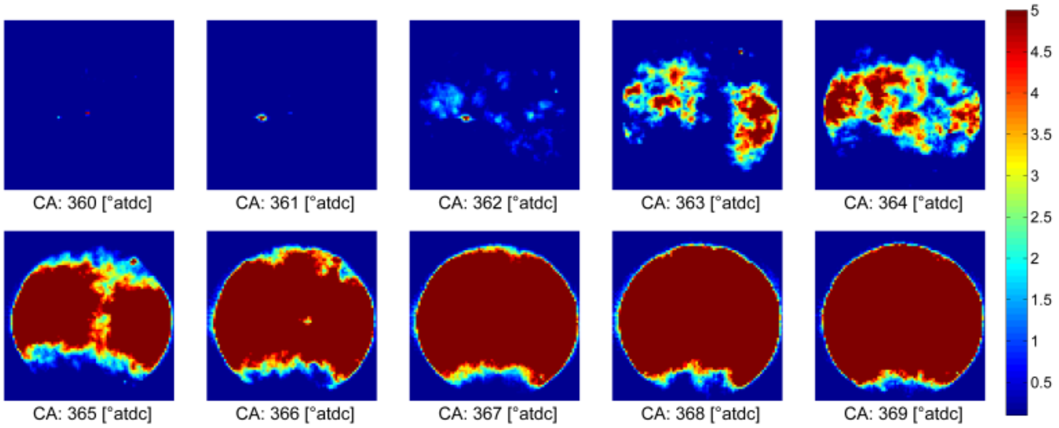

Figure 4-10. Results for average chemiluminescent intensity for E0 HCCI and ϕ=0.45 at 700 RPM.

Analysis of the averaged image maps highlights differences in the flame propagation phase of the two spark timings considered in the study. Figure 4-11 and Figure 4-12 show the time histories of the image maps from 351° to 365° aTDC for E0 with ϕ=0.45 and SA at 20° and 40° bTDC, respectively. The spark events happened earlier than the frames shown in the figures; thus the maps are of flame data only.

The later SA timing yielded more compact flames that were more consistent in location compared to the earlier SA timing. The local autoignition events induced by the later SA were also more consistent in timing and location for SA at 20° bTDC compared to SA 40° bTDC and compared to the baseline HCCI. The first observation of local autoignition sites was similar to the HCCI case, with autoignition zones clearly present at 362°aTDC for SA 20° bTDC.

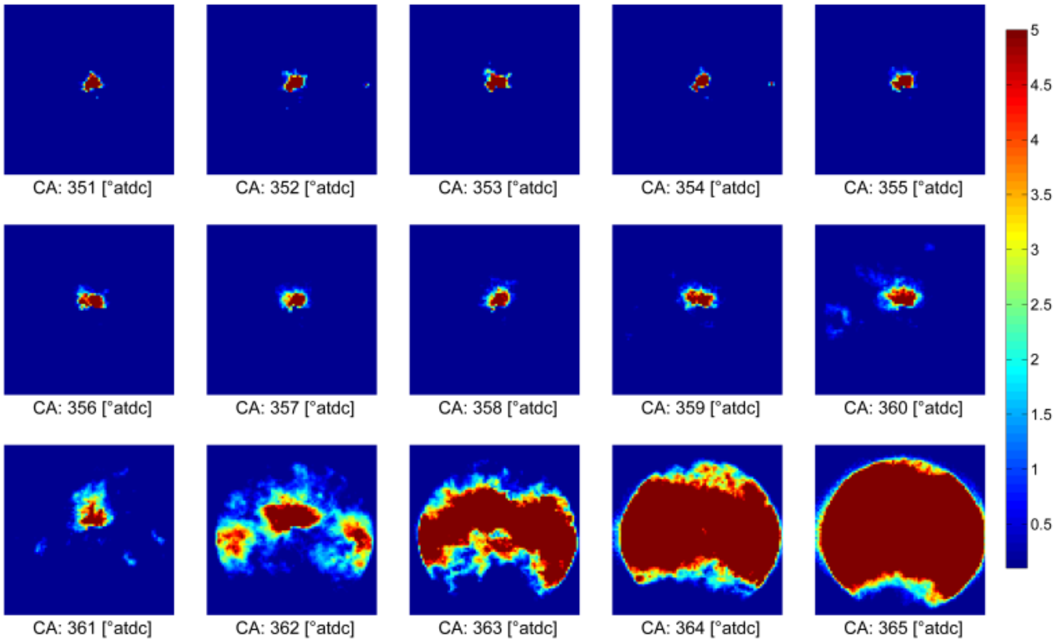

Figure 4-11. Results for average chemiluminescent intensity for E0 with SA at 20° bTDC and ϕ=0.45 at 700 RPM.

As seen in Figure 4-12, the more advanced SA resulted in more diffuse flame structure compared to SA 20, and the flames propagated further in the combustion chamber prior to autoignition. The local autoignition started about 1° earlier for the SA 40 conditions compared to SA 20 and HCCI for E0 with ϕ=0.45.

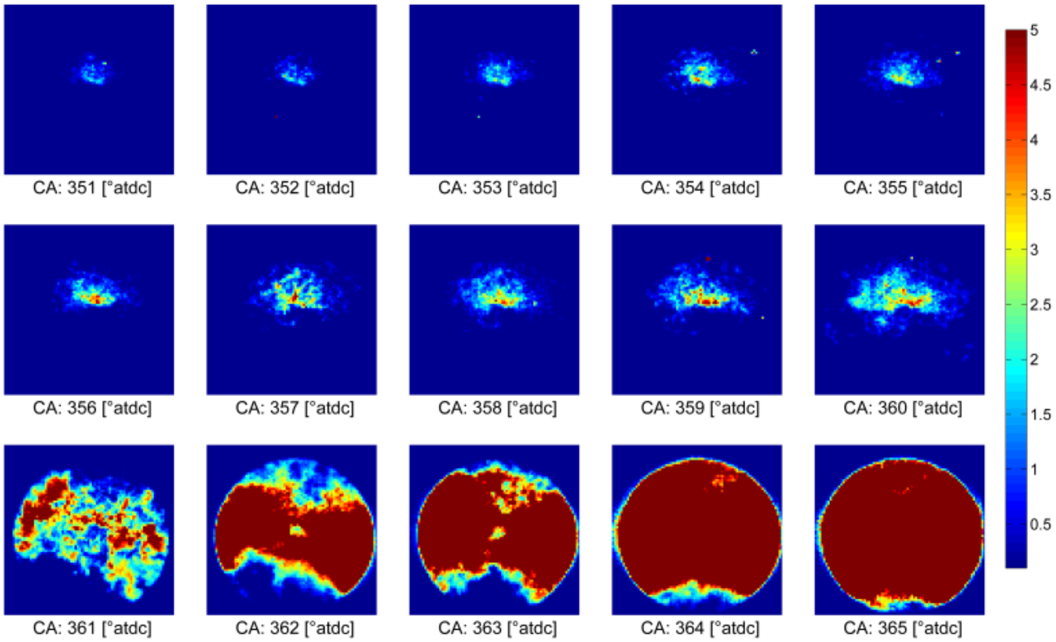

Figure 4-12. Results for average chemiluminescent intensity for E0 with SA at 40° bTDC and ϕ=0.45 at 700 RPM.

The lowest equivalence ratio of the study (ϕ=0.40) represented the lean operating limit for the engine at the preheat conditions considered. E0 exhibited poor stability in HCCI mode (COV_{IMEPn}=10.6%) at ϕ=0.40. When SA was applied at the lean limit, combustion phasing was advanced and stability was improved for E0; however, no flames were observed with the imaging system. The imaging results are presented in Figure 4-13 for E0 with SA at 40° bTDC and ϕ=0.40. As seen in the previous SA imaging data, thermal stratification resulted in preferred localized ignition between the intake and exhaust valves, but unlike the previous spark assist data, the region near the spark plug (the center of the viewing area) did not ignite until much later.

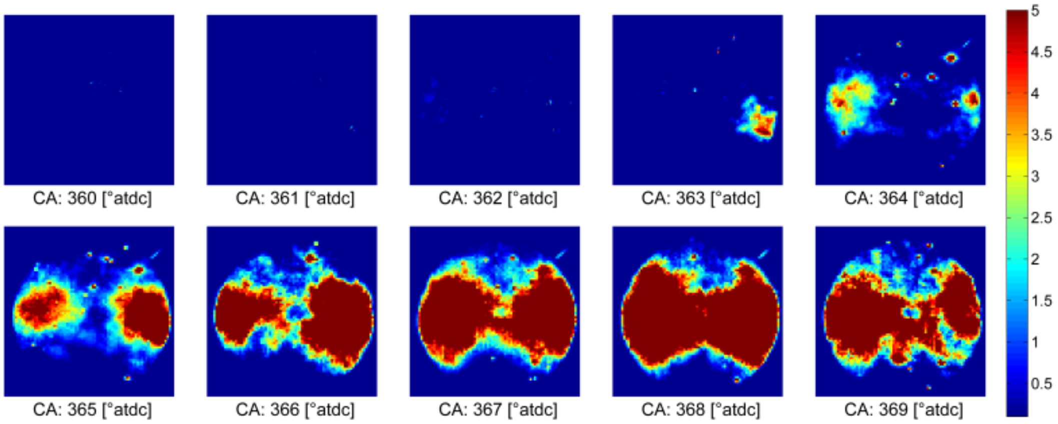

Figure 4-13. Results for average chemiluminescent intensity for E0 with SA at 40° bTDC and ϕ=0.40 at 700 RPM.

Figure 4-14 show the averaged chemiluminescence intensity between 351 and 365 °aTDC for E30 experiments at ϕ=0.45 with SA at 40 ° bTDC (same conditions as E0 experiment shown in Figure 4-12). The differences in the flame propagation between the E30 and the E0 fuels are remarkable and consistent with the individual cycle data presented above. The E30 flames were better defined (in part due to the higher in-cylinder densities) and advanced further into the combustion chamber for the E30 blend compared to the E0. In addition, the E30 flames were more consistent in the location and propagation rates compared to E0. The local autoignition sites prior to autoignition were also more consistent.

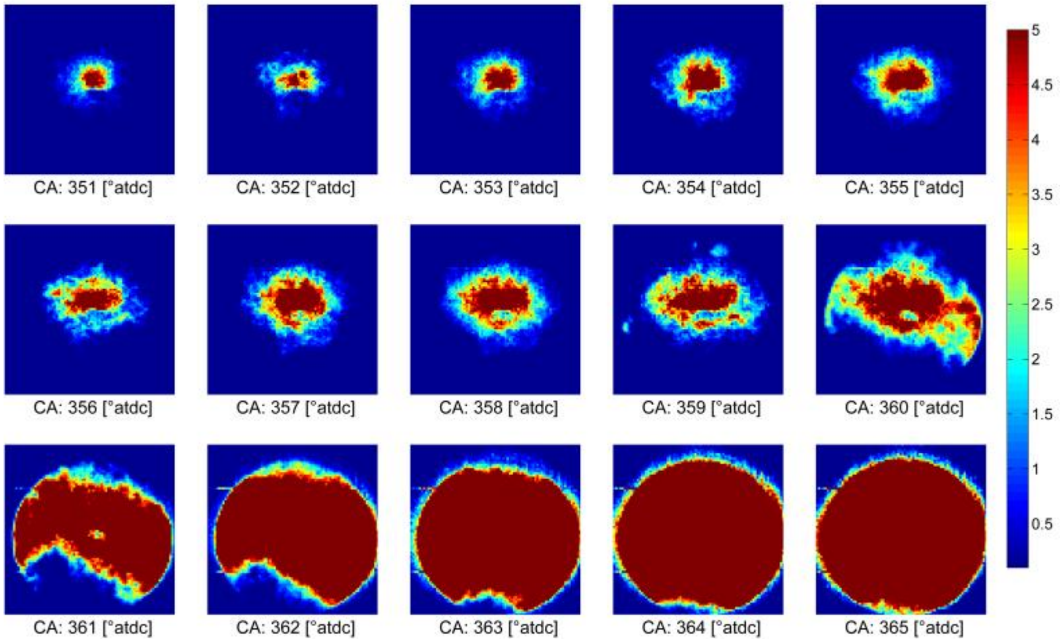

Figure 4-14. Results for average chemiluminescent intensity for E30 with SA at 40° bTDC and ϕ=0.45 at 700 RPM.

Mass Fraction Burned

The imaging and in-cylinder pressure data were used together to estimate how much mass was burned by flame propagation prior to autoignition. This information is valuable to quantify the impact of SA on combustion and to develop and validate models of SA-HCCI combustion. Such estimates can only be made using the combination of imaging and pressure data, as the presence of flames were not detectable from the HRR data alone, as shown in Figure 4-6. Moreover, the imaging data showed the rapid increase in heat release that occurred at the onset of autoignition was due to a combination of flame propagation and local autoignition.

The process to determine mass fraction burned by flame propagation was as follows. The imaging data were used to identify the onset of autoignition, defined as the time of the first observation of local autoignition sites. Then the in-cylinder pressure data were used to determine the amount of mass fraction burned (MFB) to that point in the cycle. This process was applied to each combustion cycle, and the average and standard deviation of the 30 cycles are reported in Table 4-3 for each spark assist condition at 700 RPM.

While the standard deviations are large for MFB for some conditions, several trends are apparent. Systematically less mass was burned by flame propagation for the ethanol blends compared to E0 for the same SA timing and equivalence ratio, whereas the images might indicate otherwise. The MFB ranged from 9.3%-18.7% for E0 and from 4.7%-15.5% for E30. Advancing spark assist timing, increased the mass burned prior to autoignition from SA20 to SA40 (almost doubling the MFB at some conditions); however, there was diminishing impact on advancing timing at SA60. Equivalence ratio effects appear small when the standard deviations in the data are considered. The average $IMEP_n$ values are included for comparison in Table 2, and no correlation appears between the results for MFB and $IMEP_n$, which is consistent with conclusion of the imaging data that phasing (which dictates IMEP) is not well correlated with the properties of flame propagation.

Table 4-3. Timing of autoignition (θ_{AI}) as determined from the SA-HCCI imaging data and corresponding MFB based on θ_{AI} and the in-cylinder pressure data. The standard deviations are reported for ~30 cycles of 700 RPM data.

Fuel	ϕ	SA	θ_{AI} [°aTDC]	$\sigma\theta_{AI}$	MFB @AI	σ_{MFB} @AI	$IMEP_n$ [bar]
E0	0.5	SA20	359.4	0.8	9.5%	0.04	1.67
E0	0.5	SA40	356.4	0.8	17.2%	0.07	1.24
E0	0.45	SA20	361.3	1.1	12.7%	0.06	1.15
E0	0.45	SA40	360.4	1.0	18.7%	0.07	1.29
E0	0.4	SA20	365.4	1.8	9.3%	0.05	1.35
E0	0.4	SA40	363.2	1.3	13.5%	0.06	1.47
E0	0.4	SA60	361.9	1.6	11.4%	0.05	1.41
E30	0.5	SA20	356.5	0.6	6.2%	0.03	1.94
E30	0.45	SA20	362.7	1.5	9.3%	0.05	1.68
E30	0.45	SA40	359.5	1.1	15.5%	0.05	1.68
E30	0.4	SA20	361.8	1.3	4.7%	0.03	1.51
E30	0.4	SA40	361.4	1.4	10.3%	0.04	1.50
E30	0.4	SA60	358.8	1.0	10.5%	0.04	1.49

Effects of Engine Speed

Higher engine speed experiments were performed to investigate the effects of increased turbulence associated with higher piston speeds. The preheating and charge compositions were kept the same as the conditions used at 700 RPM to maintain similar chemical reaction rates. Sjoberg and Dec [73] demonstrated the reactivity of neat ethanol was the same as the reactivity of gasoline for engine speeds of 1200 RPM and higher. Therefore, an engine speed of 1200 RPM was used in this work. The experimental results for 1200 RPM are reported in Table 4-4.

Table 4-4. Experimental results for engine and emission of HCCI and SA-HCCI data at 1200 RPM.

Fuel	HCCI/SA	ϕ	P_{max}	COV_{Pmax}	$IMEP_n$	COV_{IMEPn}	CA50	σ_{CA50}	NOx	UHC	CO
-	[°bTDC]	-	[bar]	[%]	[bar]	[%]	[°aTDC]	[°aTDC]	[ppm]	[ppm]	[%]
E30	HCCI	0.45	20.15	7.6	1.59	7.8	373.9	2.19	5	697	0.20
E30	SA20	0.45	19.62	6.3	1.37	12.8	373.9	2.27	4	685	0.20
E30	SA40	0.45	24.56	3.8	1.48	2.8	366.9	1.33	1	426	0.13
E30	SA60	0.45	28.03	4.2	1.36	3.1	362.6	1.70	0	377	0.10
E0	HCCI	0.48	20.17	8.2	1.40	8.0	373.2	2.67	4	594	0.19
E30	HCCI	0.48	21.89	7.1	1.45	4.4	371.3	1.93	1	506	0.15
E0	SA20	0.48	22.61	5.4	1.48	5.1	369.8	1.52	2	460	0.16
E30	SA20	0.48	22.31	5.0	1.37	2.6	369.7	1.46	3	496	0.14
E0	SA40	0.48	24.98	4.4	1.37	7.2	365.9	1.59	2	412	0.14
E30	SA40	0.48	27.19	3.1	1.46	2.6	364.3	1.08	2	376	0.11
E30	SA50	0.48	28.45	3.5	1.58	2.3	362.6	1.53	1	328	0.10
E0	HCCI	0.52	26.25	4.5	1.67	7.3	366.7	1.15	3	378	0.12
E30	HCCI	0.52	29.59	2.6	1.76	4.8	364.8	0.92	9	328	0.10
E0	SA20	0.52	27.93	8.5	1.60	13.6	364.3	0.92	3	343	0.11
E30	SA20	0.52	30.52	1.9	1.83	2.6	363.0	0.83	10	324	0.10
E0	SA40	0.52	29.97	1.9	1.69	2.2	361.8	0.76	3	320	0.10
E30	SA40	0.52	33.00	1.8	1.75	2.0	359.0	0.84	32	275	0.10

The lean limit for stable HCCI combustion shifted from $\phi = 0.40$ for 700 RPM to $\phi = 0.45$ for 1200 RPM and misfire occurred at conditions which had previously exhibited stable HCCI behavior at low speed. The increased engine speed decreased the time available for autoignition chemistry, so at the same pressure and temperatures, a higher ϕ was needed to decrease the ignition delay.

Figure 4-15 shows the combustion phasing, IMEP_n and the thermal efficiency results as a function of spark assist timing for 1200 RPM. The combustion phasing was retarded at the higher engine speed compared to the lower engine speed for the same ϕ. Spark assist advanced phasing at all conditions with a larger shift in advancing combustion phasing at the higher engine speeds. The same variation of combustion phasing was observed for both fuels at both engine speeds and spark assist improved the stability for E30 as with the lower speed cases. The thermal efficiencies for 1200 RPM and 700 RPM for E0 were comparable. However, E30 exhibited lower thermal efficiencies at the higher engine speed, to the extent that the efficiency benefit of E30 was no longer apparent at 1200 RPM.

The emissions data for the 1200 RPM experiments are provided in Table 4-4. The results were similar to the results of the low speed experiments. The improvements in the UHC and CO emissions were more sensitive to SA at lower ϕ. The most significant decrease in emissions was observed with the E30 experiments at the leanest condition with a decrease in UHC and CO emissions of approximately 50%. NO_X emissions were in the single digit [ppm] levels, except for the richest condition with the most advanced spark assist.

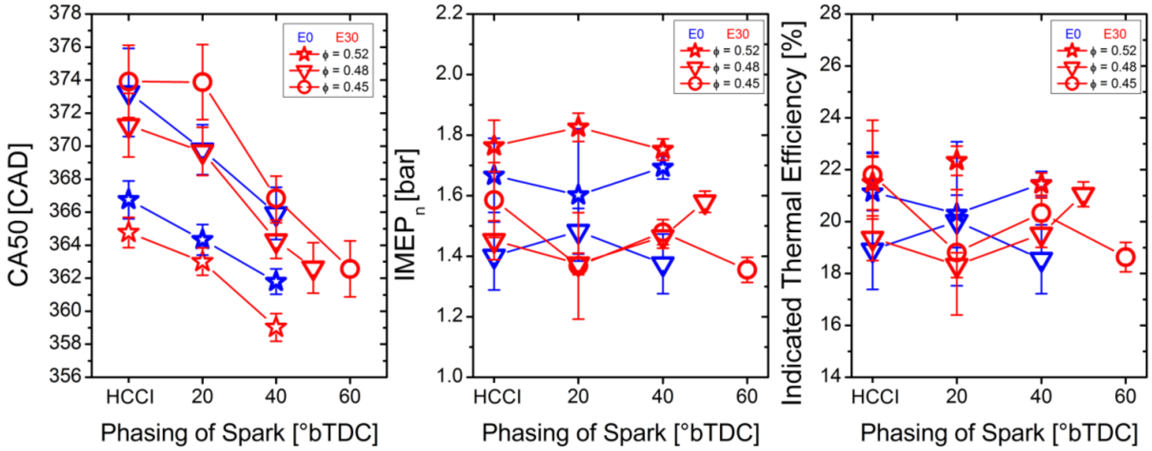

Figure 4-15. The effect of SA on CA50, IMEP$_n$ and indicated thermal efficiency for the two fuel blends at 1200 RPM. The error bars are the standard deviations for the cycle averaged data.

Imaging data of the 1200 RPM experiments exhibited similar behavior as observed with the 700 RPM results. As seen in Figure 4-16, HCCI showed similar preferential locations for local autoignition compared to 700 RPM. The image acquisition rate was increased to 5154 fps to maintain the same temporal resolution for the higher engine speed, and therefore the exposure time was decreased to 180 μs for these experiments.

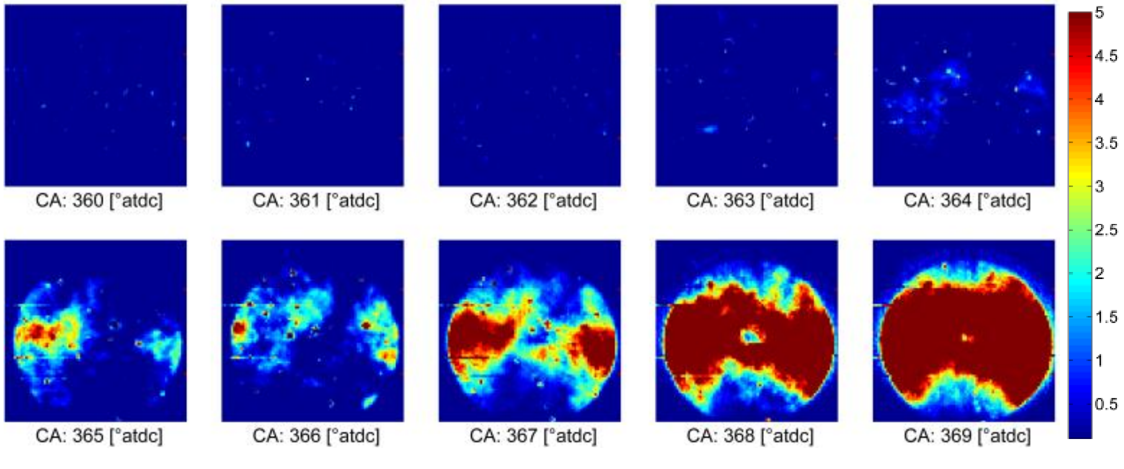

Figure 4-16. Results for average chemiluminescent intensity for E30 HCCI and ϕ=0.45 at 1200 RPM.

Figure 4-17 shows the averaged chemiluminescence intensity between 351 and 365° aTDC for E30 experiments at ϕ=0.45 with SA at 40° bTDC at 1200 RPM (the same conditions as the E30 experiment at 700 RPM shown in Figure 4-14). The general features were the same with well-defined flame structure and progress. The increased turbulence due to higher engine speed did not appear to affect the flame propagation rate, and the differences in flame growth between the two engine speeds were within the uncertainty bounds of cycle-to-cycle variation. One difference between the imaging data at the two engine speeds was the timing of the observation of the local autoignition zones was later at 362 °aTDC for 1200 RPM (~2° difference compared to 700 RPM) which resulted in later CA50 of 366.9 °aTDC and lower IMEP$_n$ of 1.48 bar.

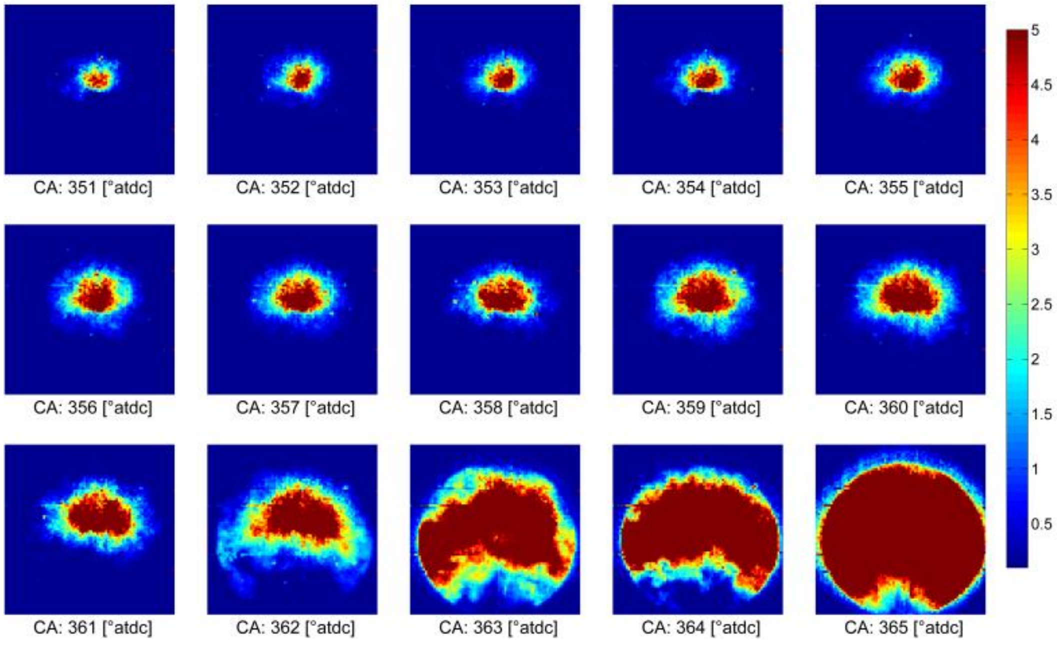

Figure 4-17. Results for average chemiluminescent intensity for E30 with SA at 40° bTDC and ϕ=0.45 at 1200 RPM.

The evaluation of the amount of MFB prior to the first local autoignition event showed the same trends as observed at 700 RPM, with approximately 10-13% of the heat release occurring before the autoignition event. The results are presented in Table 4-5. The primary difference between the lower speed data and the higher speed data was lower variation was observed at 1200 RPM.

Table 4-5. Timing of the autoignition (θ_{AI}) as determined from the imaging data, and the MFB prior to the first local autoignition event as determined using θ_{AI} and the in-cylinder pressure data. The standard deviations are reported for ~50 cycles of 1200 RPM data.

Fuel	ϕ	SA	θ_{AI} [°aTDC]	$\sigma\theta_{AI}$	MFB @AI	$\sigma_{MFB\ @AI}$	$IMEP_n$ [bar]
E0	0.48	SA20	363.1	1.1	6.2%	0.03	1.48
E0	0.48	SA40	361.6	1.4	15.3%	0.06	1.37
E0	0.48	SA60	355.9	1.3	14.3%	0.04	1.42
E0	0.52	SA20	360.0	1.1	7.6%	0.04	1.60
E0	0.52	SA40	357.5	1.0	9.5%	0.03	1.69
E30	0.45	SA20	364.7	1.5	4.2%	0.02	1.37
E30	0.45	SA40	361.9	1.0	11.1%	0.03	1.48
E30	0.45	SA60	358.8	1.3	14.9%	0.04	1.36
E30	0.48	SA20	363.5	0.07	7.2%	0.02	1.37
E30	0.48	SA50	359.1	0.15	14.6%	0.04	1.46
E30	0.52	SA20	358.5	0.04	4.1%	0.01	1.83
E30	0.52	SA40	355.7	0.13	12.9%	0.03	1.75

4.5 Conclusions

Spark assist effects were compared to baseline HCCI for a reference gasoline and a blend of 30% ethanol with 70% gasoline. A range of spark timings were considered at different fuel/air equivalence ratios ranging from $\phi = 0.4$ to $\phi = 0.5$. High speed imaging was used to identify connections between spark initiated flame propagation, autoignition, and engine performance including heat release rate, $IMEP_n$ and mass fraction burned. Cycle-to-cycle variations and time averaged data were evaluated. The combination of high-speed imaging and in-cylinder pressure data support the following conclusions.

- Ethanol generally improved performance (IMEPn, indicated thermal efficiency, and engine stability) compared to E0.
- Spark assist at 40° bTDC advanced combustion phasing compared to baseline HCCI for both fuels at all conditions studied, with greater response (~10 CAD) at 1200 RPM compared to 700 RPM (~5 CAD). Combustion stability improvement was also observed at lower equivalence ratios and higher engine speeds.
- The imaging data indicated the increase in HRR that occurred immediately prior to global autoignition (within 1-2 CAD) was due to a combination of autoignition of small parcels of fuel/air charge and flame propagation.
- Analysis of cycle-to-cycle variation in the features of the flames initiated by SA, including the flame speed and the start of flame propagation relative to the spark timing, indicated that the variation in flame features did not correlate well with the maximum rate of heat release, autoignition phasing, or IMEP.

- Combined analysis of the imaging and in-cylinder pressure data indicated less than 20% of the mass fraction was burned during flame propagation for E0 for both engine speeds and less than 16% mass fraction was burned during flame propagation for E30.

The data indicate global ignition of SA-HCCI is dominated by autoignition, and the compression heating caused by flame propagation primarily serves to accelerate autoignition of local sites which are already thermally preferred, which then accelerate global autoignition. The timing of SA is a tradeoff between advancing SA and initiating flames at colder bulk temperatures (potentially quenching the flame or slowing flame progress) and giving the flames more time to expand and heat the remaining unburned charge, and retarding SA and initiating flames at later times when bulk temperatures are higher (yielding higher flame speeds), but with less time for the flames to affect the unburned gases. Local conditions and fuel specific flame speeds will affect the range of useful SA timing. Regardless of spark timing, the charge must already be sufficiently close to autoignition that compression heating by small fractions of the fuel/air charge can have an impact.

Chapter 5

In-Cylinder Particulate Matter Emissions of DISI Engine

5.1 Objective

Experiments of ethanol/gasoline fuel blends were conducted to understand the fundamental effects of ethanol blends on fuel spray properties and in-cylinder soot formation using a direct fuel injection engine configuration. The optically accessible single cylinder DISI engine was used to acquire high speed in-cylinder imaging data of fuel spray and PM formation in the engine as a function of the ethanol content in the fuel, the fuel injection timing, and engine coolant temperature. These data provide insight into the physical mechanisms controlling in-cylinder PM formation in ethanol fuel blends in DISI engines.

The contents of this chapter have been published in SAE Int. J. Fuels Lubr. 2013 [57].

5.2 Experimental Approach

This study was conducted using the DISI single cylinder optical research engine facility of the University of Michigan, which is described in Section 2.2. The engine setup schematic is shown in Figure 5-1.

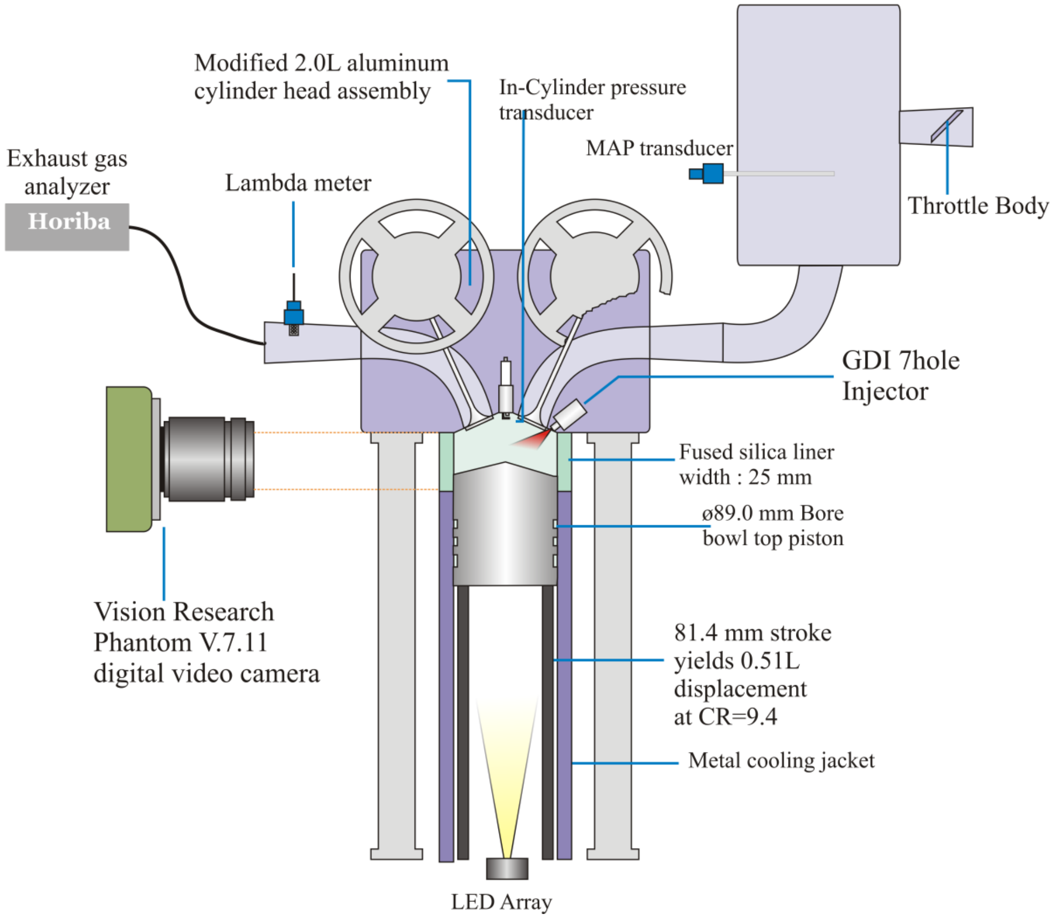

Figure 5-1. Optical DISI engine setup schematic.

The engine speed was set at 1500 RPM for this study. The engine control module for spark and fuel injection was integrated with the dynamometer control system. Stoichiometry was controlled by varying the fuel injector driver pulse width (PW) duration while setting a constant fuel rail pressure of 100 bar. All experiments in the study were operated at stoichiometric conditions and a load condition of approximately 5.5 bar $IMEP_n$, with a fixed intake manifold absolute pressure of 76 kPa. The spark timing was adjusted to maintain a fixed combustion phasing of CA50 ≈ 8° aTDC.

The combustion chamber was imaged through the fused silica cylinder liner using a high-speed color digital video camera with a widescreen CMOS array (Vision Research Phantom v7.11, color). The camera was positioned at the exhaust manifold side of the engine looking at the fuel injection pocket (see Figure 5-1). A macro 105 mm lens (af micro Nikkor 105mm f2.8 d) was used with the camera to adjust the focal length and f4.0 was selected to optimize the focal depth and light exposure. Two high intensity LED arrays (1 × 3 array of 3-watt cool white LEDs) were installed at the two sides of the engine (perpendicular to the fuel injection stream) to visualize the spray. In this study, the camera was focused at a plane coinciding with the spark plug ground electrode. The camera settings were fixed at 1280 × 552 pixels at 9000 frames per second (corresponding to 1 frame/CAD) with 100 μs exposure time. Non-filtered emission was recorded via the high-speed color digital camera and time-sequenced with the crank-angle resolved pressure data. The imaging data captured flame propagation (via chemiluminescence), soot formation (via incandescence/thermal emission of the soot particles) and scattering of the LED emission by the fuel spray.

Camera images were time sequenced to a common trigger with in-cylinder pressure data. The imaging data were synchronized with the pressure data with an uncertainty of ~0.1-0.2 ms or 1-2 CAD. The high speed imaging data were acquired for 11000 frames corresponding to 15 consecutive combustion cycles. The images were post-processed to extract temporal and spatial information. Color enhancement algorithms were applied to the images to isolate the soot incandescence and reduce interference from reflections and other stray features. Averages of the imaging data were generated using the data from the 15 combustion cycles.

Figure 5-2 presents the step-by-step processing of the imaging data. The upper left panel in the figure shows a frame from the original imaging file corresponding to 60° aTDC. The bottom left panel presents the results of converting the image to grey scale and after a threshold has been applied to reduce stray reflections and other interfering signals. The right panel shows the results of averaging the 15 frames corresponding to 60° aTDC from each of the combustion cycles. A false color scale has been applied to the data in the right panel.

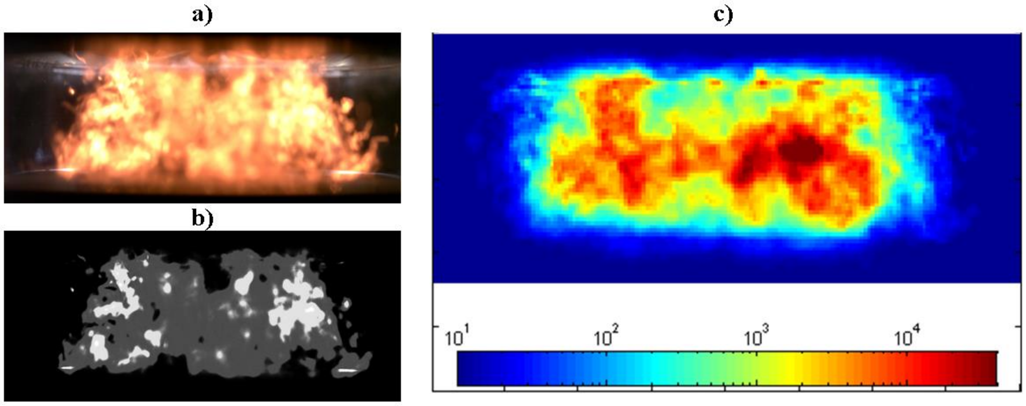

Figure 5-2. Image processing steps. a) original image, b) background elimination and conversion to grey scale, c) average intensity map of 15 cycles in false scale.

5.3 Experimental Results

Effects of Ethanol in Blends

The effects of ethanol concentration in the fuel blends were studied while keeping other operating parameters constant. Indolene was the baseline fuel and two blends of 50% and 85% ethanol/indolene were chosen for the study. E85 blends are relevant to production vehicles and the existing fueling infrastructure in the U.S., and fuel flexible vehicles will experience a range of ethanol concentrations depending on the fueling history of the vehicle. In addition, Kar et al. [74] found 30-50% ethanol blends experienced the maximum amount of cooling in a port fuel injected SI engine compared to other blend ratios. If the trends are similar for a DISI engine, the 50% ethanol blends may have the largest impact on PM and fuel spray characteristics in this study.

The coolant temperature for the experiments was set to 30 °C and the fuel injection timing (start of injection, SOI) was set to 250 °bTDC. The fuel injection duration increased from 1.75 ms for E0 to 2.42 ms for E85 to maintain the stoichiometry of the mixtures at the target of $\phi = 1.0$. Results for the maximum in-cylinder pressure (P_{max}), combustion phasing (CA50), net indicated mean effective pressure ($IMEP_n$) and engine stability (represented as the coefficient of variation, COV, of $IMEP_n$) as well as corresponding measurements of engine-out emissions are presented in Table 5-1. As seen in data, the IMEP, NOx and CO emissions improved (7-8% for IMEP and NOx, and 39% for CO), with increasing ethanol content in the fuel.

Table 5-1. Operating conditions and results of engine performance and engine-out emissions for different fuel blends

Fuel	**SOI**	**$T_{coolant}$**	**P_{max}**	**CA50**	**$IMEP_n$**	**COV $_{IMEPn}$**	**NO_X**	**UHC**	**CO**
-	[°bTDC]	[°C]	[bar]	[°aTDC]	[bar]	[%]	[ppm]	[ppm]	[%]
E0	250	29	28.88	8.64	5.34	1.6	1624	653	0.44
E50	250	28	29.27	8.71	5.49	1.2	1629	934	0.31
E85	250	32	29.15	10.19	5.73	1.4	1487	688	0.27

Figure 5-3 presents still images (original and unprocessed) and average results for processed imaging taken from the imaging sequences of the experiments listed in Tables 1 and 2. Images are presented for every 10 CAD. The effects of ethanol on reducing in-cylinder soot formation are significant and obvious. The soot formation is localized above the piston away from the cylinder walls for the E0 baseline case, compared to the E50 where soot formation is near the top of the imaging area as well as near the piston surface. Very little soot is evident for the E85 conditions.

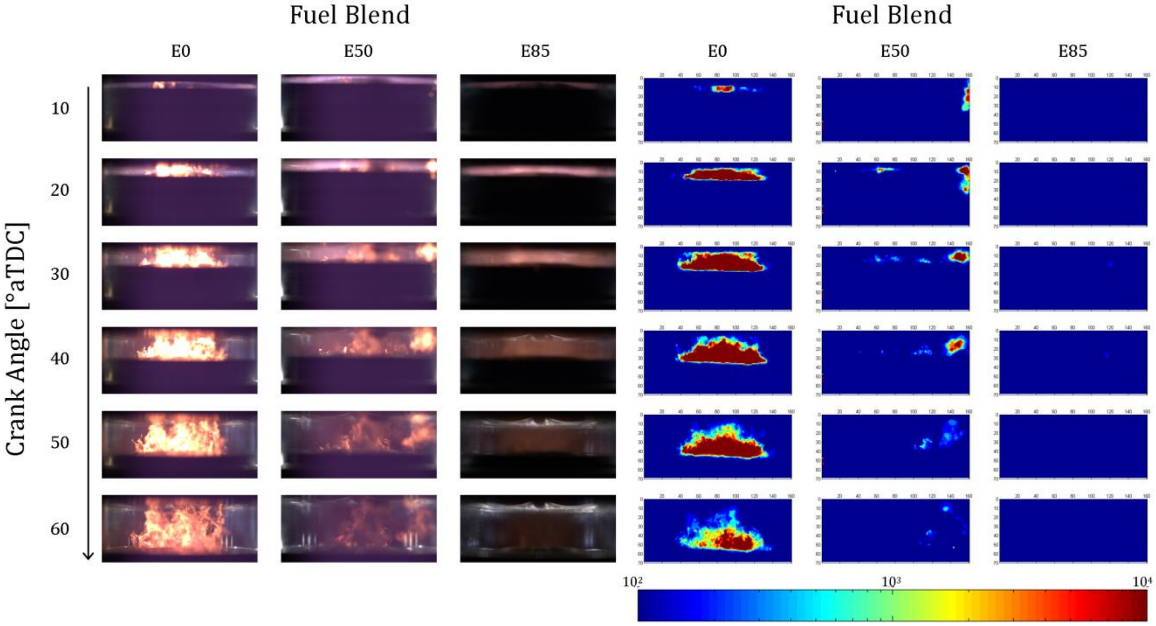

Figure 5-3. PM formation; left: typical image results (original and unprocessed); right: average results for processed imaging for fuel blends with the same SOI= 250 °bTDC and coolant temperature of 30 °C. Every 10th frame is shown.

The images were used to develop a quantitative measure of the PM as a function of time. The total intensity of the thermal radiation of the soot particles was spatially integrated for each image. This metric, the spatially integrated natural luminosity (SINL), is presented in Figure 5-4 for the three fuel blends as a crank angle degree. The error bars in the figure represent the standard deviation of the SINL for the 15 combustion cycles. As expected, the trends of high soot formation for E0 and less for the ethanol are well captured using the SINL. The SINL data also capture a maximum for the E0 fuel. The E50 results exhibit an approximately constant SINL within the standard deviation of the images for a large portion of the cycle (~15-40 °aTDC). 10^2

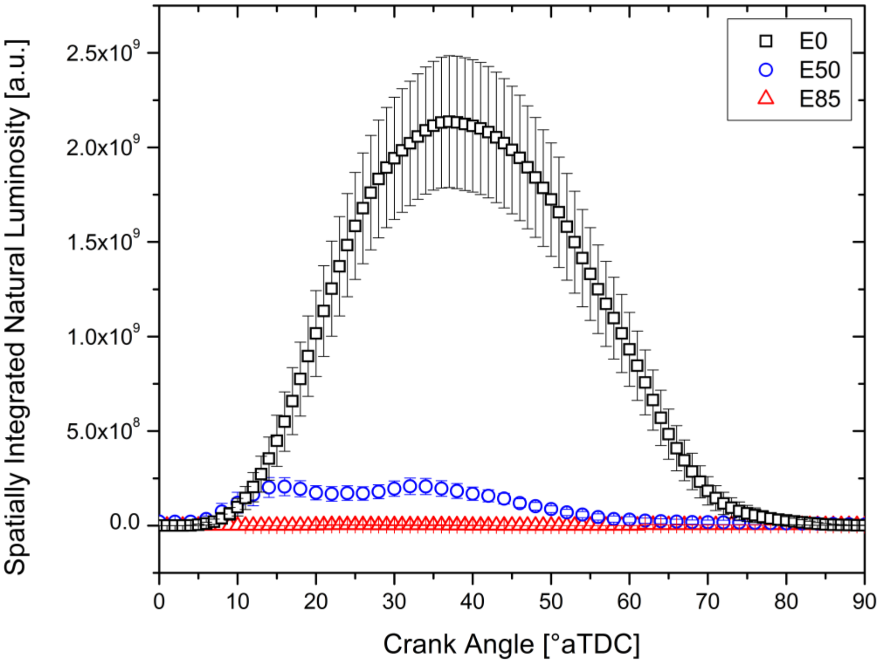

Figure 5-4. SINL for the fuel blends with the same SOI= 250 °bTDC and coolant temperature of 30 °C.

Effects of Fuel Injection Timing

The engine operating conditions and results of the effects of advancing fuel injection timing (reported as start of injection, SOI) are presented in Table 5-2. The IMEP$_n$ and NO$_X$ and CO emissions are also shown in Figure 5-5. For each fuel blend, the more retarded fuel timing led to higher peak pressures, earlier CA50 timing, higher IMEP and lower COV. The E85 blend produced the highest IMEP. The more retarded fuel timing also consistently demonstrated a tradeoff in CO and NOx emissions; reducing CO emissions and increasing NOx emissions for each fuel blend. The increase in NOx emissions are consistent with the increase in temperatures expected with the higher peak cylinder pressures.

Table 5-2. Operating conditions and results of engine performance and engine-out emissions for different fuel injection timing

Fuel	**SOI**	**$T_{coolant}$**	**P_{max}**	**CA50**	**$IMEP_n$**	**COV $IMEP_n$**	**NO_X**	**UHC**	**CO**
-	[°bTDC]	[°C]	[bar]	[°aTDC]	[bar]	[%]	[ppm]	[ppm]	[%]
E0	250	29	28.88	8.64	5.34	0.016	1624	653	0.44
E0	330	28	25.17	12.20	4.97	0.019	326	973	0.81
E50	250	28	29.27	8.71	5.49	0.012	1629	934	0.31
E50	330	25	26.68	11.45	5.16	0.015	556	814	0.83
E85	250	32	29.15	10.19	5.73	0.014	1487	688	0.27
E85	320	28	26.23	13.04	5.57	0.015	431	1026	1.01

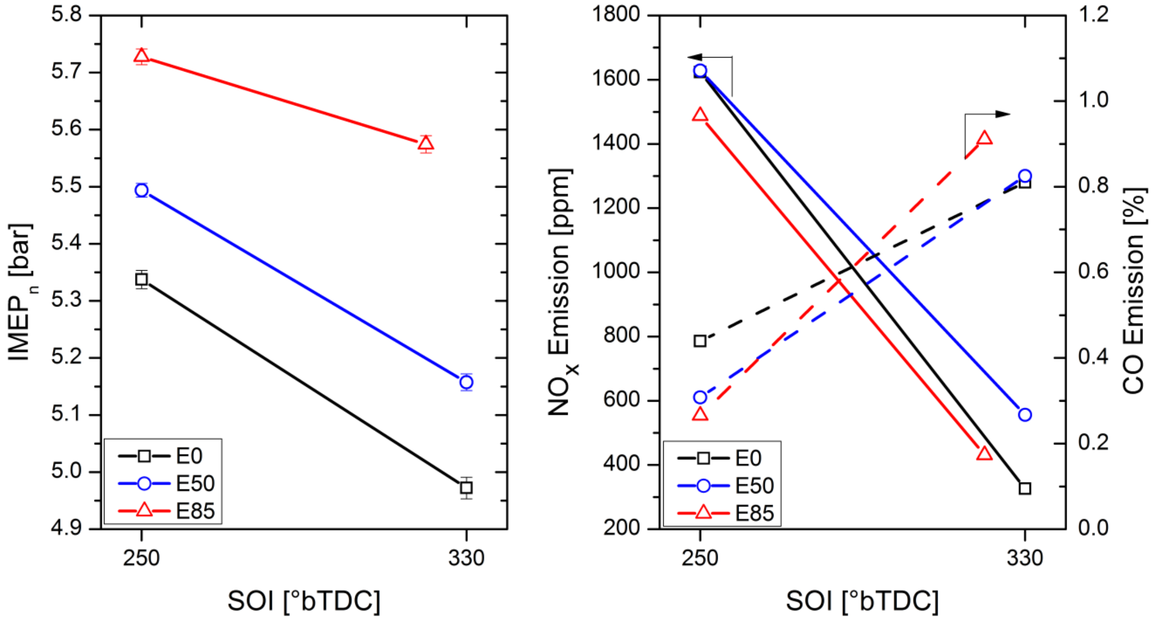

Figure 5-5. IMEP$_n$ (left) and NO$_x$/CO emissions (right) as a function of fuel injection timing for the different fuel blends.

The earlier SOI increases the fuel impingement on the piston bowl, increasing soot formation as seen in the imaging data presented in Figure 5-6. The imaging data indicate less soot is formed in the E50 and E85 blends; however, significant PM luminosity is observed for both ethanol blends at the earlier fuel injection timing. The imaging data show the PM signals are highest above the piston for all three fuels, which is an indication of a diffusion controlled combustion within localized fuel rich areas on the piston as a result of a liquid film of fuel (pool firing). Figure 5-7 presents the corresponding SINL data for the fuel blends. Significant reductions in the SINL were observed for all the fuels by retarding the start of fuel injection. The SINL data were also normalized to the maximum values for each fuel to demonstrate the sensitivity of the soot formation to fuel injection timing between the fuel blends. The results are presented in the right panel of Figure 5-7. E0 has lower sensitivity to fuel injection timing with respect to soot suppression. Complete elimination of PM luminosity was observed in the images of the ethanol blends; whereas, ~10% SINL remained even with the more retarded injection timing for E0.

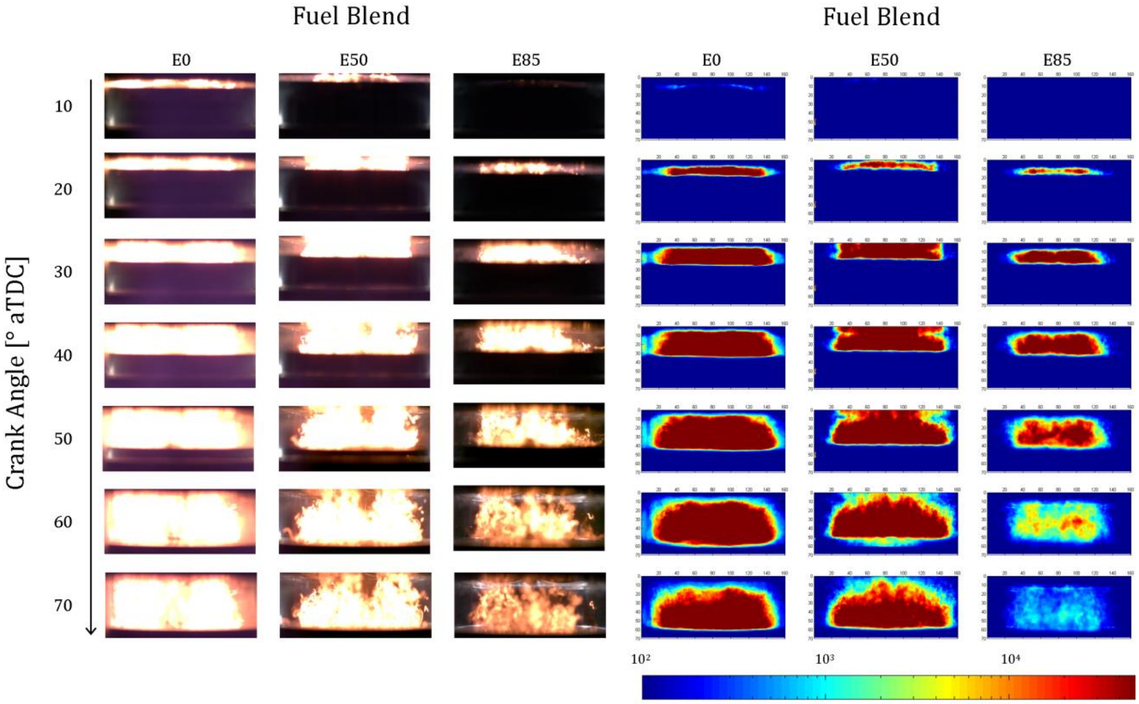

Figure 5-6. PM formation; left: typical image results (original and unprocessed); right: average results for processed imaging for fuel blends with SOI = 330° for E0 and E50 and SOI = 320° bTDC for E85, coolant temperature 25-32° C. Every 10th frame is shown.

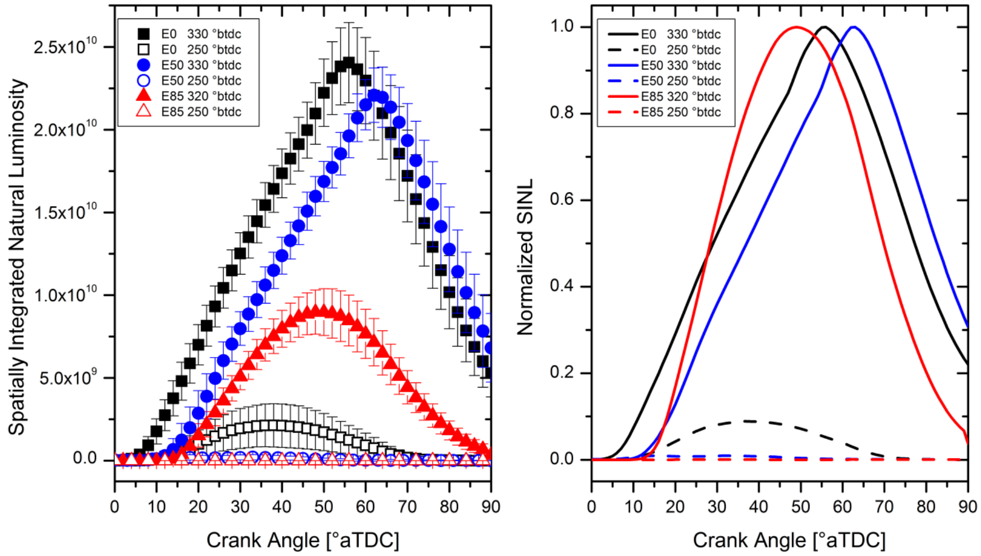

Figure 5-7. Effects of fuel injection timing on SINL (left) and sensitivity of normalized SINL (right) for fuel blends at a coolant temperature of ~30 °C.

Effects of Coolant Temperature

The temperature of the engine walls and piston surface has direct impact on the vaporization of the fuel [52], [75]. Consequently, engine coolant temperature is expected to have direct effect on PM formation. Experiments were performed to investigate coolant temperature effects for E0 and E50. E85 was not considered as the PM formation was generally low for the baseline operating conditions with the later SOI. For these experiments, the fuel injection timing and engine MAP were held constant at 250 °bTDC and 76 kPa. Engine operating conditions and results are shown in Table 5-3. Peak pressures, CA50, IMEP, and engine stability did not change significantly (<10%) for the different coolant temperatures. NOx emissions were high for all conditions.

Table 5-3. Operating conditions and results of engine performance and engine-out emissions for different fuel blends and different coolant temperatures

Fuel	**SOI**	**$T_{coolant}$**	**P_{max}**	**CA50**	**$IMEP_n$**	**COV $_{IMEPn}$**	**NO_X**	**UHC**	**CO**
-	[°bTDC]	[°C]	[bar]	[°aTDC]	[bar]	[%]	[ppm]	[ppm]	[%]
E0	250	29	28.88	8.64	5.34	0.016	1624	653	0.44
E0	250	92	28.44	9.57	5.15	0.016	2070	236	0.42
E50	250	28	29.27	8.71	5.49	0.012	1629	934	0.31
E50	250	90	27.80	9.80	5.07	0.013	1696	850	0.61

The effects of coolant temperature on PM were significant as seen in Figure 5-8 which compares SINL and normalized SINL for the fuels. The higher coolant temperatures suppressed PM formation by over 90% (based on normalized SINL signal) for both fuels. E0 was slightly more sensitive to the temperature increase, but E0 also exhibited much higher levels of PM for the base case ($T_{coolant}$ = 30° C).

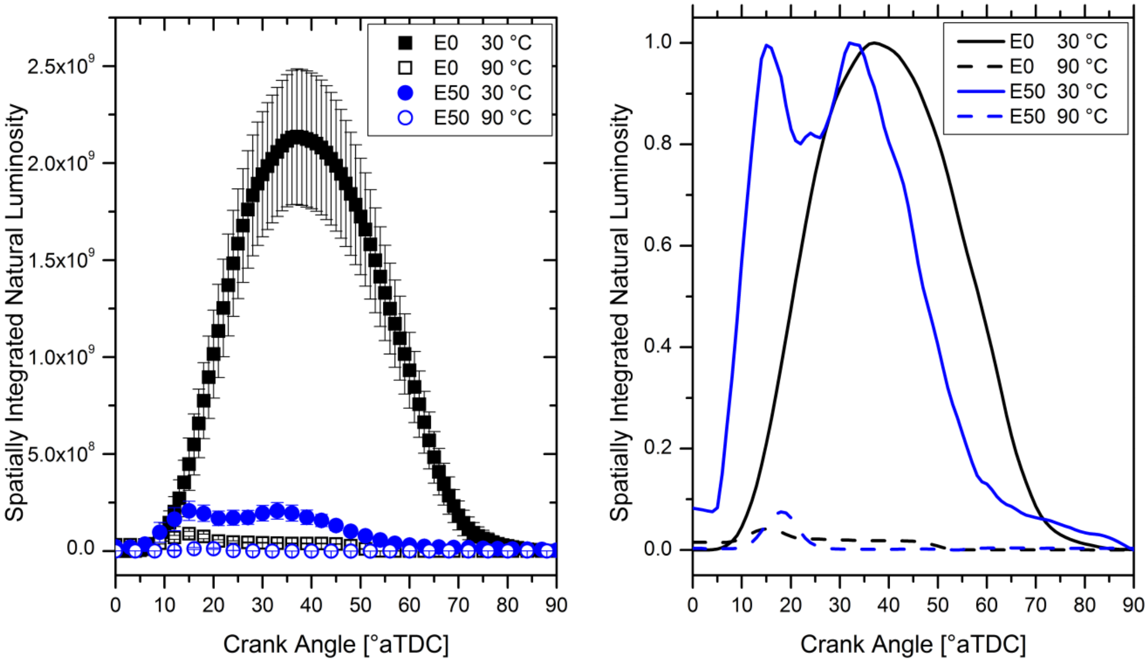

Figure 5-8. Effects of engine coolant temperature on SINL (left) and sensitivity of normalized SINL (right) for fuel blends with SOI of 250 °bTDC.

Spray Pattern Effects

The temperature of the cylinder head was controlled by heating the coolant to the desired temperature. The coolant temperature also affects the fuel temperature. Conduction heat transfer between the fuel injector and the cylinder head is expected to be high, the fuel is assumed to reach the same temperature as the cylinder head. Considering the distillation curve of the fuel, approximately 35% of E0 components are volatile at temperatures less than 90° C and the percentage of volatile component increases as the ethanol concentration in the blend increases [54], [55]. At different fuel injector temperatures, the volatile components of the fuel will vary and may impact the spray characteristics of the fuel. Spray images from the engine coolant experiments were acquired to investigate the effects on the fuel spray for the

E50 blend and to compare the fuel sprays for E0 and E50 at the same coolant temperature (90° C).

Figure 5-9 shows typical spray imaging sequences of the fuel sprays. E0 and E50 have the same rate of spray penetration, but E50 exhibits a wider spray cone angle compared to E0. The more narrow fuel distribution for E0 results in a more dense core that takes longer to evaporate even though the E0 has a lower enthalpy of vaporization compared to E50. All the fuel sprays show fuel impingement on the piston surface. Comparing the two coolant temperature cases of E50, it is notable that the penetration distance is longer and spray collapse happens later at the colder coolant condition. The evaporation of the E50 fuel also takes 4-5 CAD longer for the colder coolant conditions.

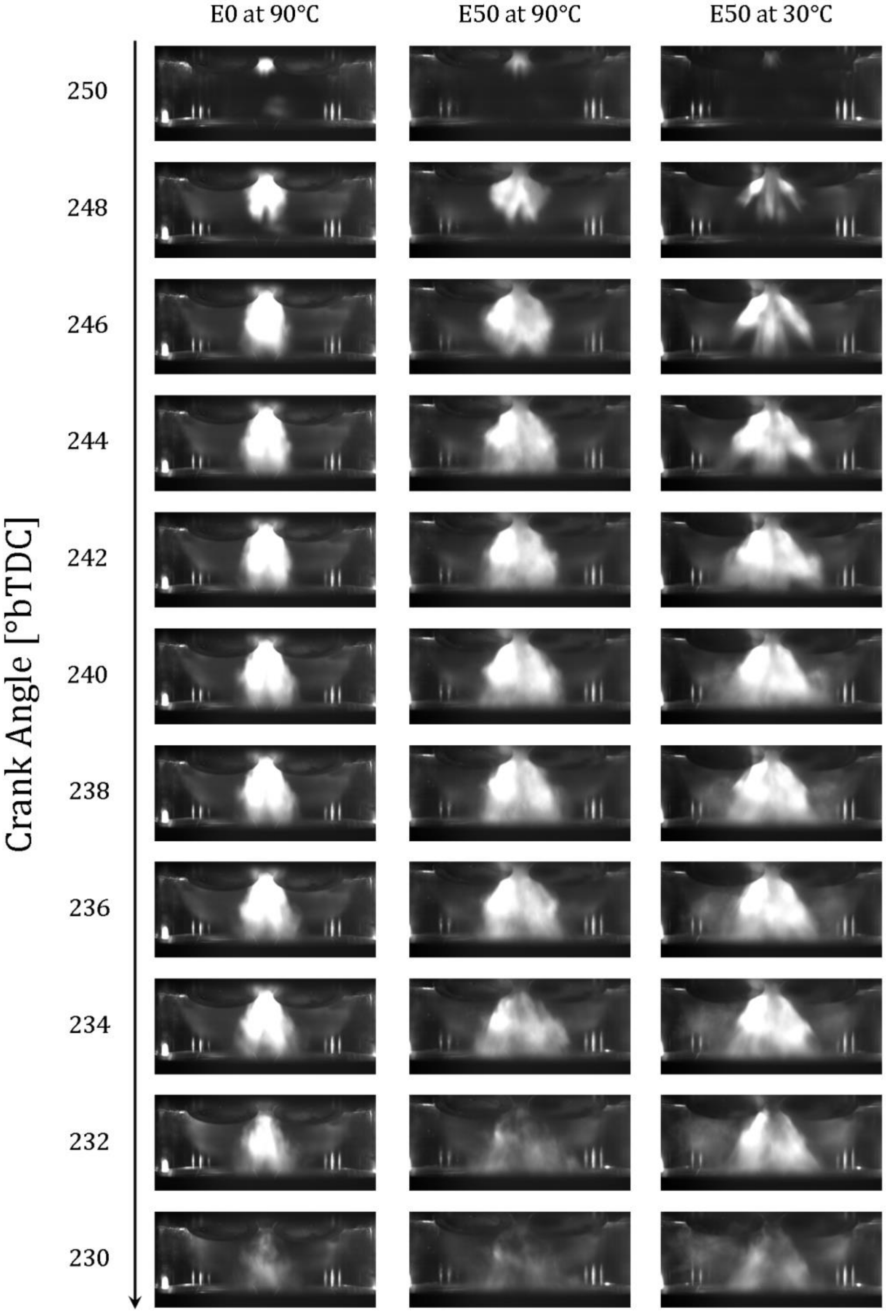

Figure 5-9. Typical image sequence of sprays comparing fuel blends with the same SOI= 250 °bTDC and comparing the effects of coolant temperature for E50. Every other frame is shown.

5.4 Conclusions

An experimental study investigated the effects of ethanol blends and engine operating conditions on the in-cylinder formation of soot in a DISI engine. The high speed imaging data were used to quantify effects on in-cylinder soot formation of fuel injection timing and coolant temperature for indolene, E50 and E85.

- Addition of ethanol to the fuel generally improved engine performance compared to E0 in terms of increasing IMEP_n and decreasing NOx exhaust emissions.
- Significant reduction of in-cylinder PM emission was observed as ethanol was added to the fuel blend, and visible soot incandescence was virtually eliminated using E85.
- E50 demonstrated an order of magnitude reduction in soot incandescence (as indicated by SINL) compared to E0.
- Soot formation largely correlated with conditions leading to high fuel impingement on the piston surface which generated a liquid film on the piston and resulting pool fires in which the soot was formed. Consequently, PM formation was significantly reduced by conditions that reduced fuel impingement on the piston, e.g. later fuel injection timing.
- The different fuel blends exhibited different levels of sensitivity of PM formation to changes in fuel injection timing and coolant temperature, e.g. the ethanol fuel blends exhibited higher sensitivity to retarding the injection timing compared to E0.
- The lower levels of soot formed by the ethanol blends may also be partially attributed to the spray characteristics, where the ethanol blends produced wider spray cone angles, improving mixing and

enhancing the vaporization; thus reducing the chance of piston wetting and diffusion flame on the piston.

The crank-angle-resolved imaging data presented in this study document in-cylinder PM formation of ethanol fuel blends. The results provide insight on how increasing the ethanol content of the fuel can be used to reduce DISI PM formation. The results provide a basis for developing general fuel injection strategies to minimize fuel impingement on the piston surface and cylinder walls. The data further provide quantitative sensitivity of in-cylinder PM formation to engine operating conditions which would be helpful in developing engine control strategies to avoid PM.

Chapter 6

Particulate Matter Emissions Study of Neat Fuel Performance in a DISI Engine

6.1 Objective

In the study presented in Chapter 5, pool fires of fuel films on piston surfaces were identified as a primary source of soot emissions in the DISI engine. This study builds on the previous work, by considering 100% anhydrous ethanol (the previous work considered only gasoline/ethanol blends) and by imaging from the direction orthogonal to the axis of the fuel injector. In Chapter 5 the imaging was performed from the exhaust side (parallel to the injection plane- looking into the fuel injector) and the in-cylinder soot formation was not preferential to one side of the cylinder (i.e. the soot incandescence was symmetrical with respect to the cylinder centerline). The change in imaging orientation presented in this chapter allows direct imaging of the fuel spray interaction with the piston surface, which was identified as critical to understanding the effects of ethanol on in-cylinder soot formation. The optically accessible single cylinder DISI engine was used to acquire the high speed imaging data of fuel spray and PM formation in the engine. The effects of the fuel injection timing and different engine coolant temperature on the fuel spray and soot formation were evaluated for the neat fuels. Engine-out smoke measurements were also performed to identify links between the in-cylinder PM imaging and the PM engine-out measurements.

6.2 Experimental Approach

This study was conducted using the DISI single cylinder optical research engine facility of the University of Michigan, which is described in section 2.2. The imaging and lighting directions were changed compared to the previous study. The engine setup schematic is shown in Figure 6-1.

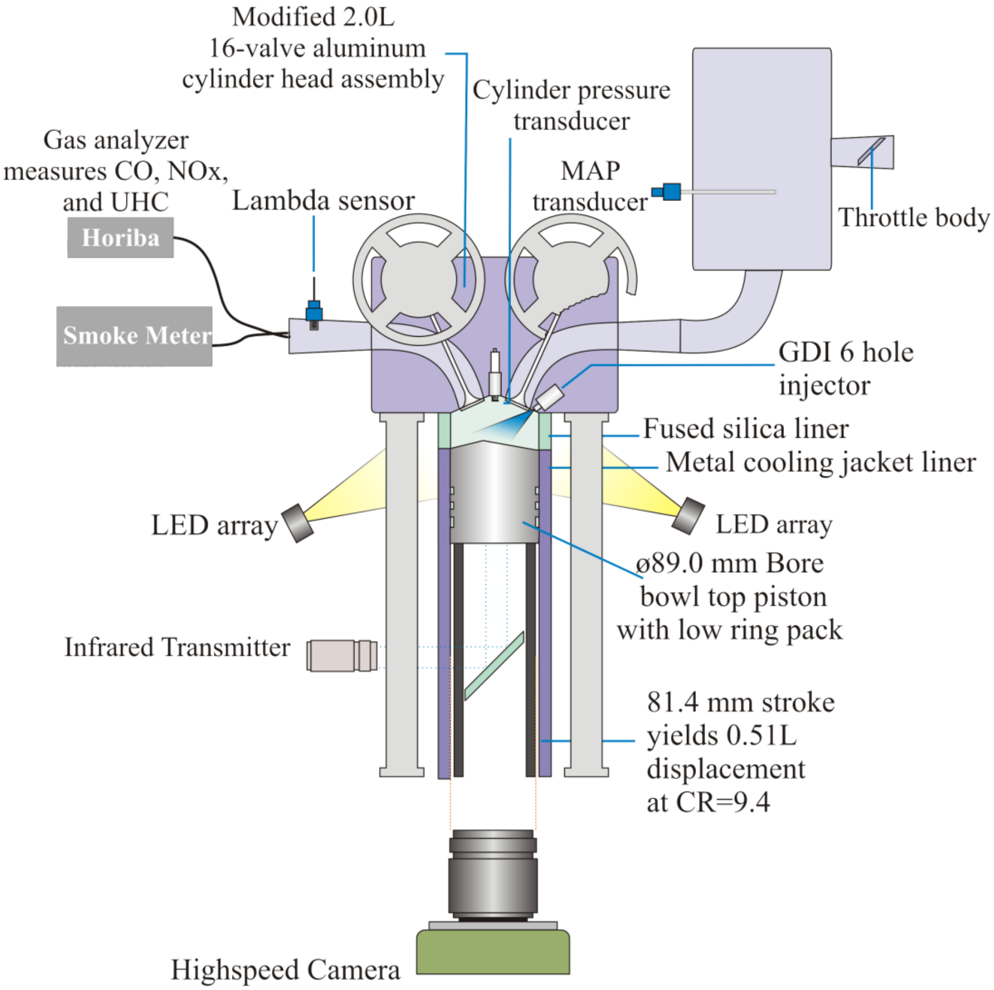

Figure 6-1. Schematic of optical DISI engine setup used for imaging orthogonal to the axis of the fuel injector.

The standard cylinder metal liner for the engine was 140 mm in height. Side-view imaging was achieved in this study by replacing the upper portion of the cylinder liner with a fused silica transparent insert 25 mm in height above a 115 mm metal liner. The combustion chamber imaging was performed from the flywheel side (orthogonal to the spray plane) through the 25 mm fused silica liner using a CMOS high speed camera (Vision Research Phantom v7.11, color). The camera was focused on the center of the combustion chamber using a 105 mm macro lens (Nikkor, 105 mm f2.8 d) at f4.0 to optimize the depth of field and light exposure to the sensor. Two LED lights (1x3 high intensity LED arrays) located on the intake and exhaust sides were used to light the combustion chamber to allow imaging of the fuel spray. A spatial resolution of 1280x656 pixels at 9000 frames per second and an exposure time of 100 μs were used for the study, resulting in 1 frame per CAD. The imaging data captured the fuel spray by scattering of the LED light, combustion by chemiluminescence, and soot formation by thermal incandescence of the soot particles. No additional spectral filters were used other than the inherent spectral characteristics of the camera sensor and the collection and focusing optics. The imaging data from the high speed camera were synchronized with the pressure data using a trigger signal. A total of 11000 frames were recorded for each experimental condition which corresponded to 15 consecutive combustion cycles.

Because engine surface temperatures and heat transfer effects are particularly important in this study (as discussed below), the piston surface temperature was measured to determine the thermal variation during the experiments. The results show an increase of ~20 °C in the bottom surface of the piston starting from the last motoring cycle until the last combustion cycle. The duration of each experiment was about 10 seconds, which consisted of adjusting the engine speed after the start of combustion, followed by data acquisition and engine-out emissions measurements. The imaging data were acquired immediately after the engine speed was stabilized for a time period of about 1.2 seconds (corresponding to 11000 frames at 9000 frames per second), and the increase in the piston temperature is estimated to be less than 4 °C during this time.

All experiments were designed to achieve the same engine load and combustion phasing at 1500 RPM. The manifold absolute pressure (MAP) was adjusted to 76 kPa using the throttle position while the engine was motoring at 1500 RPM. After stable motoring was achieved, firing signals were sent to the fuel injector and spark systems. Stoichiometric combustion was targeted for the experiments and the stoichiometry was controlled by adjusting the fuel injection duration (fuel injector driver pulse width) at a fixed fuel rail pressure of 100 bar. The spark timing was adjusted to maintain a fixed combustion phasing of CA50 ≈ 8 °aTDC. The dynamometer settings were adjusted to attenuate the engine transient response in ~ 2 seconds. Data acquisition was started after the engine had reached stable firing mode. At the same time, a trigger signal was sent to the smoke meter to start the sampling of engine-out PM emissions.

6.3 Experimental Results

The effects of fuel injection timing and coolant temperature on the in-cylinder combustion, soot formation, and fuel spray characteristics were investigated for both fuels. Three fuel injection timings of SOI=320, 300 and 250 °bTDC were studied for each fuel at coolant temperatures of 25°C and 90°C. The imaging results for combustion and soot formation are presented first, and compared with the engine-out measurements of PM. The imaging results for fuel spray are then presented and discussed in the context of the soot imaging data.

In-cylinder Combustion/Soot Imaging and Engine-out Emissions

Typical imaging results of the in-cylinder combustion and soot formation are presented in Figure 6-2. Four series of frames are shown of the two fuels for SOI of 300 and 320 °bTDC all at a coolant temperature of 25 °C. The unprocessed images are presented for every 10 CAD. Soot was formed at both fuel injection times for E0. However, soot formation was almost entirely eliminated for E100 by retarding the injection timing. The other key observation is the location of the soot particles. For E0 and SOI of 320 °bTDC, the soot incandescence spans the entire piston surface. The soot incandescence is more isolated to the left hand side of the images (opposite side of the fuel injector) for SOI of 300 °bTDC. This behavior is attributed to fuel spray impingement on the piston. The more advanced injection phasing leads to more fuel impingement on the piston surface, which is supported by the spray imaging data below.

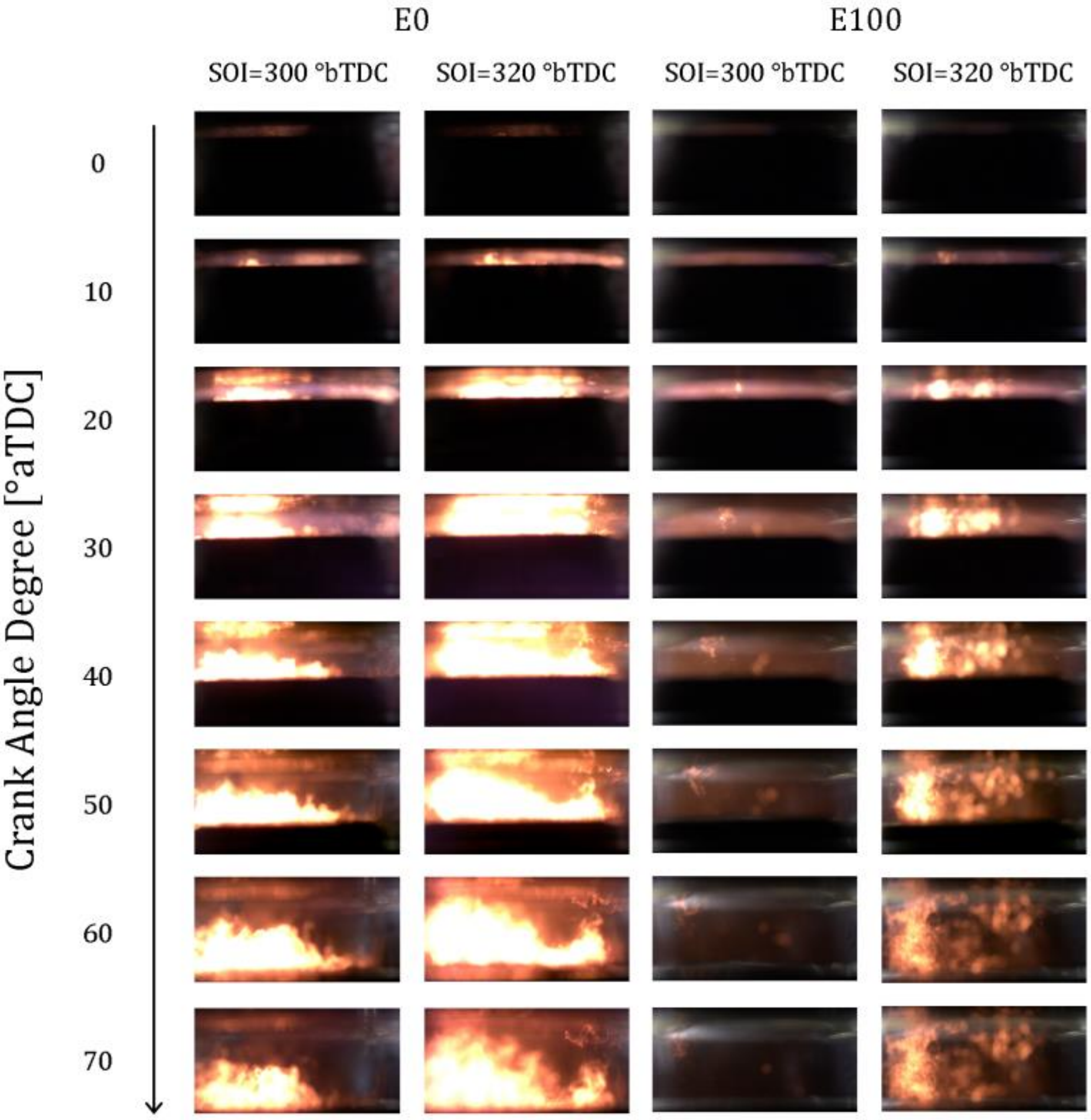

Figure 6-2. Typical in-cylinder imaging results of combustion and soot formation (unprocessed images) of single combustion cycles for E0 and E100 with SOI of 300 and 320 °bTDC at a coolant temperature of 25 °C. Every 10th frame of each imaging file is shown.

Figure 6-3 presents unprocessed images taken from the first imaging cycle of each fuel with the most retarded injection (250 °bTDC) at both coolant temperatures. At the cold coolant condition (25°C) of E0 the thermal incandescence is easily differentiable from the combustion chemiluminescence. There is no visible incandescence for E100 at this condition. The engine operation at the hotter coolant condition (90 °C) resulted in complete elimination of in-cylinder soot incandescence for both fuels. Consistent with the in-cylinder imaging, the engine-out opacity measurements indicated no soot (i.e. registered FSN of 0) for these cases as well.

For the SOI = 250 °bTDC conditions, the in-cylinder imaging recorded the visible chemiluminescence due to combustion. At the hot coolant condition, the emission from E0 is distinctly more blue in color compared to the visible emission from combustion of E100. Emission in the visible wavelength region from hydrocarbon and ethanol flames is generally attributed to chemiluminescence of C_2, CH, CHO, and OH [68]. The change in the spectral emission may be an indication of changes in the concentration of these excited species caused by changes in the fuel reaction pathways.

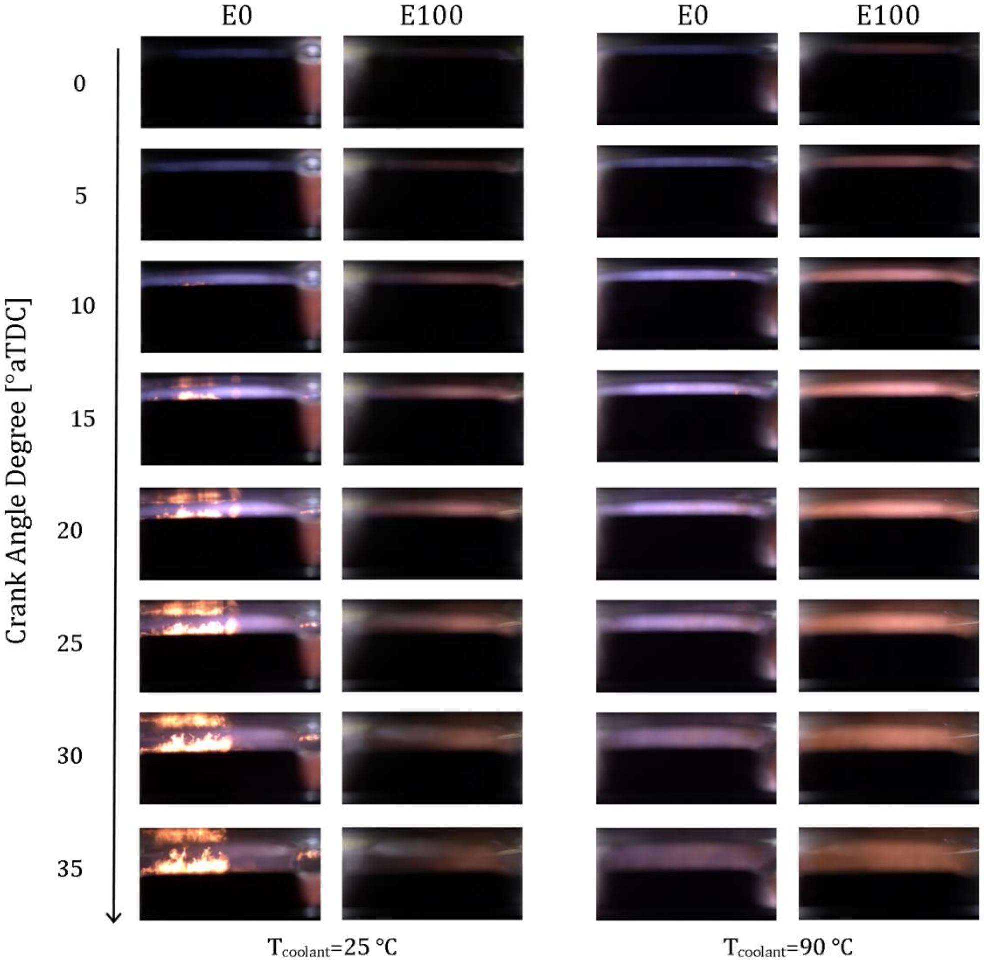

Figure 6-3. Typical combustion images (unprocessed) of single combustion cycles of E0 and E100 with SOI of 250 °bTDC. Coolant temperature of 25°C (left); Coolant temperature of 90°C (right). Every 5th frame is shown.

The results of the engine-out emissions are presented in Figure 6-4 as a function of fuel injection timing for both coolant temperatures. Higher coolant temperatures resulted in lower unburned hydrocarbon emissions and smoke numbers, but higher NO_x emissions. E100 exhibited systematically lower NO_x, UHC and soot emissions at each coolant temperature (when soot levels were measureable). The effect of the fuel injection timing on the emissions was not monotonic. The lowest NO_x emissions were at SOI = 300

°bTDC for both fuels, and UHC emissions were less sensitive than soot emissions to fuel injection timing, particularly at the colder coolant condition.

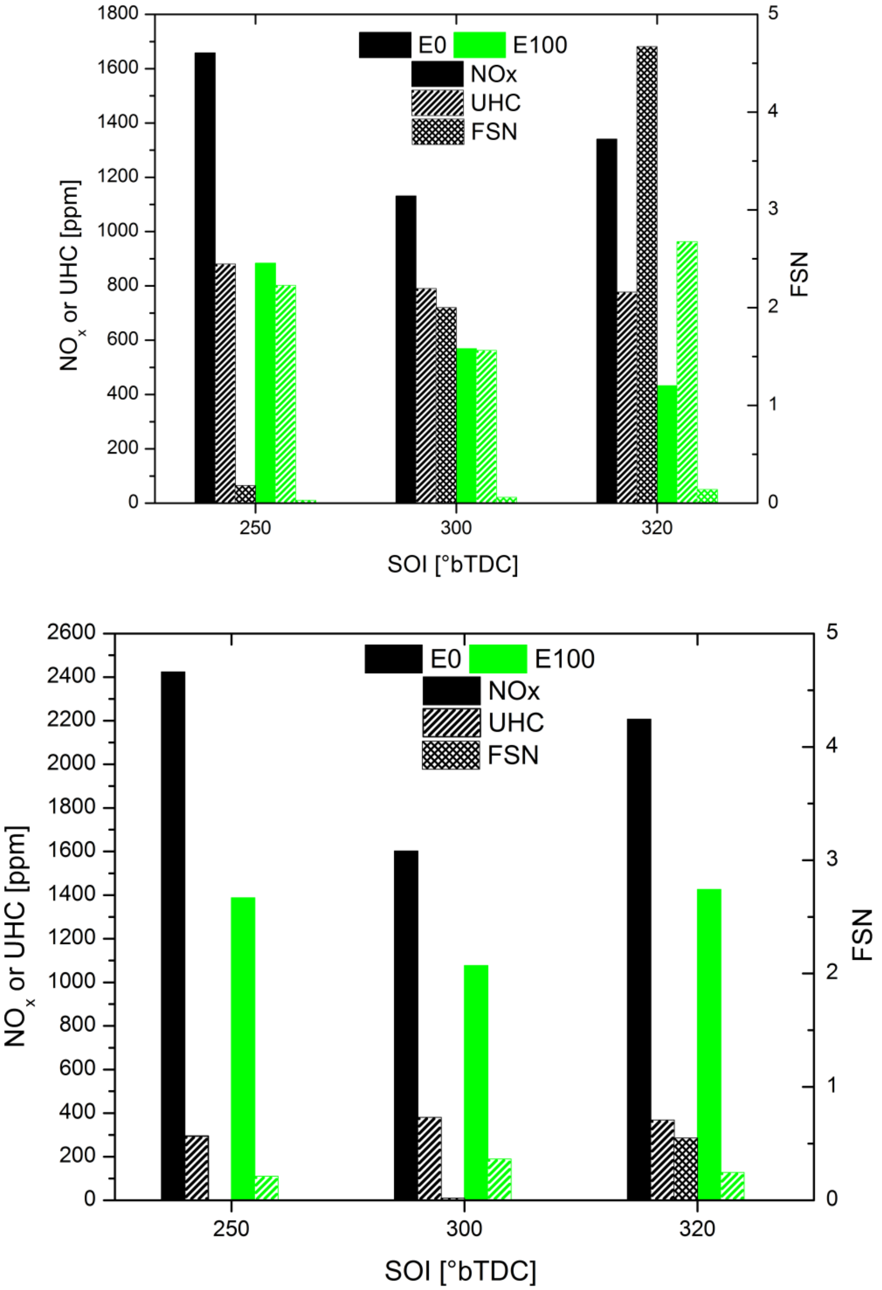

Figure 6-4. NOx, UHC and soot emissions (FSN) as a function of fuel injection timing and coolant temperature. Top panel: coolant temperature of 25° C; bottom panel: coolant temperature of 90° C.

Soot Imaging and Measurements

The images of in-cylinder soot formation were analyzed to quantify the soot formed and to determine the relationship between the in-cylinder data and the engine-out measurements of smoke number. The raw images were processed by applying a threshold to enhance the soot emission intensity. Background interference and stray reflections were eliminated by subtracting a reference frame with the piston at the same position. The resulting data were transformed to gray scale. An example of the outcome of the image processing is shown in Figure 6-5. The left panel of the figure shows the original frame corresponding to 50 °aTDC. The right panel shows the intensity map in false color scale of the image after subtracting the reference frame and applying the threshold. Intensity maps of approximately 15 cycles were averaged at the same crank angle position to represent the overall in-cylinder soot emissions at each experimental condition.

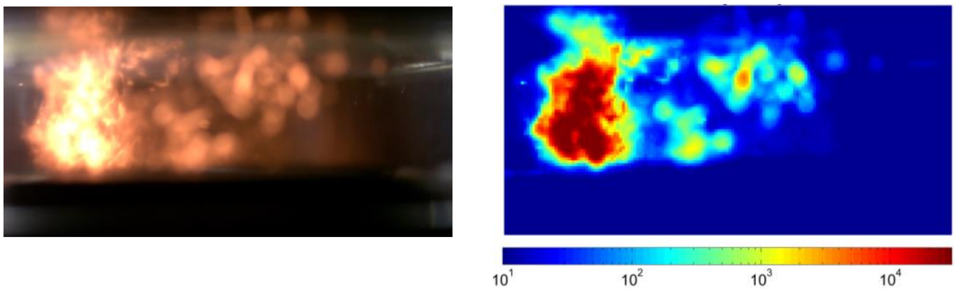

Figure 6-5. Example of the image processing method used, left) original image, right) processed image presented as an intensity map in false color. The engine operating conditions were E100, SOI = 320 °bTDC and the image corresponds to 50 °aTDC, taken with a camera exposure time of 0.9 CAD (100 μs).

The in-cylinder thermal emission of the soot particles were quantified by spatially integrating the natural luminosity (SINL) of each imaging frame. The SINL data from each cycle were then averaged at the same crank angle to provide overall data on the time history of the soot emissions. The SINL data are presented in Figure 6-6 for the three injection timings at 25°C. The error bars represent the standard deviation of the SINL data over the 15 combustion cycles. Note the SINL values below ~ 2×10^9 arbitrary units (a.u.) are attributed to spectral emission from combustion and not soot formation. The E0 data exhibit a distinctly different shape and phasing compared to the E100 data. The results for each fuel were also normalized to the maximum observed SINL for each fuel. On the normalized scale, it is apparent the maximum intensities for soot incandescence occur at later crank angles for E0 compared to E100. The decrease in signal intensity after the maximum is due to cooling of the soot particles and potentially due to soot oxidation.

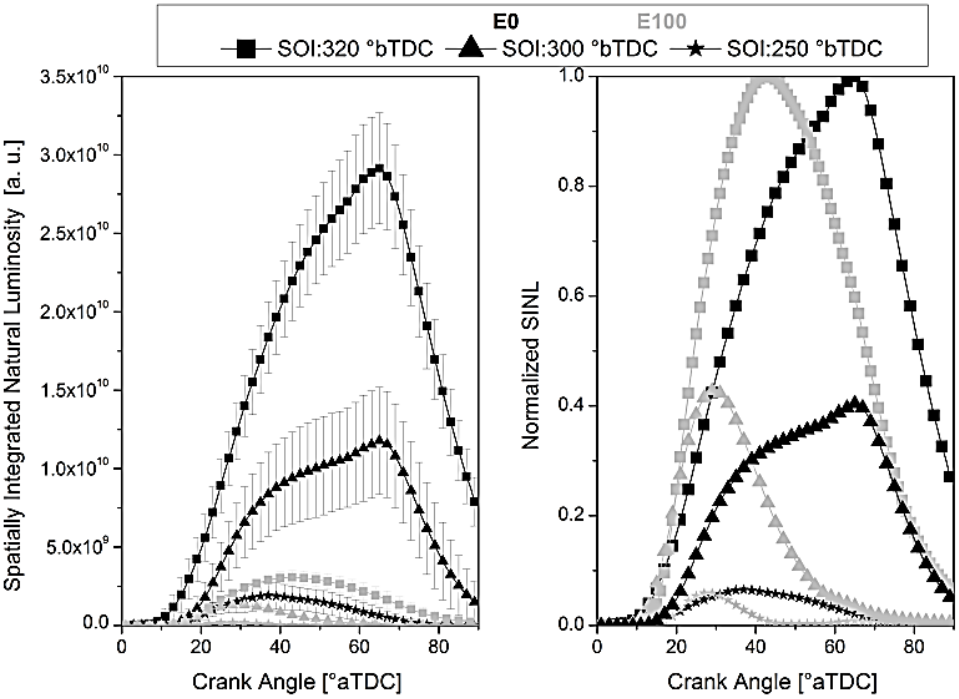

Figure 6-6. Spatially integrated image intensity data (SINL) for E0 and E100 with SOI of 250, 300 and 320 °bTDC and a coolant temperature of 25° C. SINL data above ~ 2×10^9 a.u. represent thermal emission from soot particles. SINL values below this level are attributed to spectral emission from combustion species.

The spatially integrated data were then time integrated to compare the in-cylinder soot imaging results with the exhaust gas measurements for smoke number. The spatially and time integrated imaging data are compared in Figure 6-7 for the two fuels at the different fuel injection timings and coolant temperatures. The error bars represent the standard deviation of the imaging data for the 15 combustion cycles. As presented above, at some engine conditions the image intensity is due to chemiluminescence from combustion gases with little or no intensity associated with soot incandescence, and the intensity values associated with these conditions were significantly lower than for conditions when soot was formed.

The threshold intensity for combustion chemiluminescence is marked in the figure and is ~5×10^{10} a.u. for the cases studied. This value was determined by evaluating the unprocessed images and the corresponding SINL data, and the cases below this threshold did not exhibit any thermal emission due to soot formation.

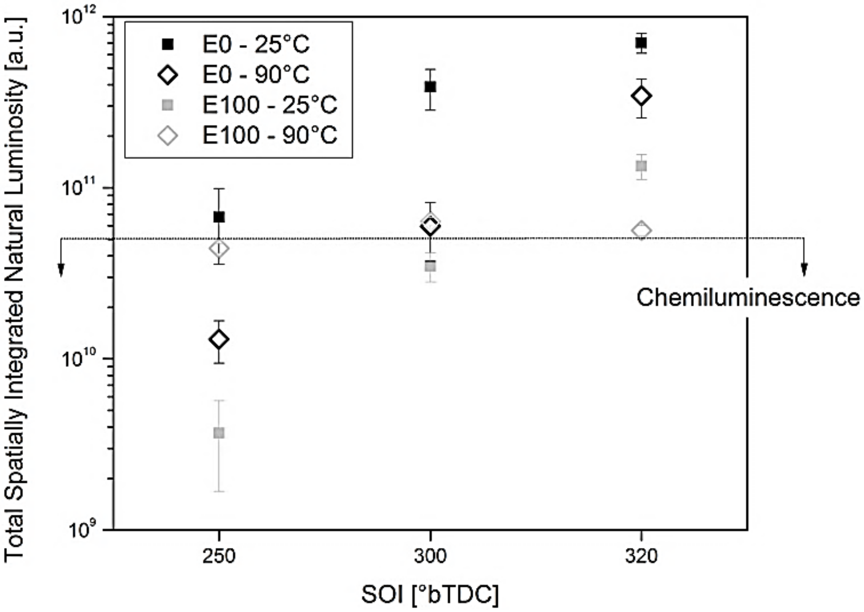

Figure 6-7. Time and spatially integrated image intensity data (total SINL) as a function of fuel injection timing and coolant temperature for E0 and E100. The data above the ~5×10^{11} limit represent in-cylinder soot formation. The data below this threshold are due to spectral emission from the combustion gases.

The total SINL data (spatially and time integrated imaging intensity) for the 15 combustion cycles are compared with the engine-out soot measurements (FSN values) in Figure 6-8. The results show a strong correlation between the in-cylinder imaging of soot and the engine-out PM measurements. Most of the operating conditions produced FSN values of less than 0.5. A second regression analysis was performed for the lower PM emissions data (shown as the inset of Figure 6-8). Although the slope changes compared to the full scale of measurements, a linear correlation is still accurate for the low sooting conditions.

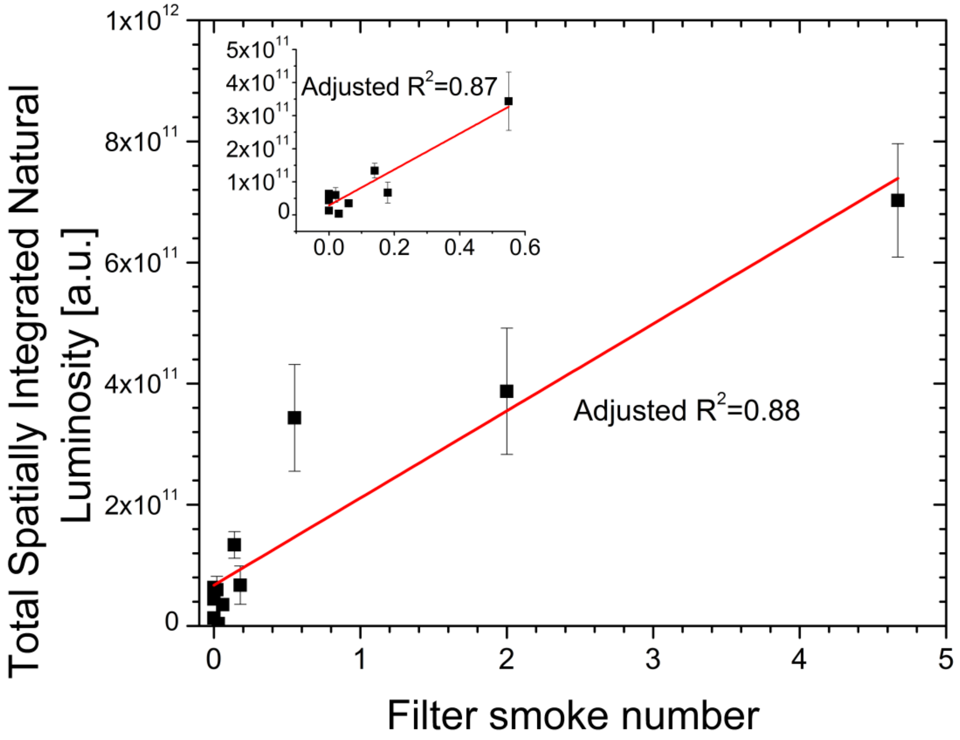

Figure 6-8. Comparison of the cumulative total (spatially and time integrated) SINL data for 15 combustion cycles with engine-out soot opacity measurements.

Cycle-averaged Results for Soot Imaging

The imaging data were averaged over the 15 combustion cycles at the same crank angle to generate average intensity maps of the combustion and soot formation processes. The results are shown in Figure 6-9 for E0 and E100 for the two coolant temperatures for SOI of 320 °bTDC. These conditions include the highest levels of soot observed in the study. It is well known that engine coolant temperature affects the PM emissions of the DISI engines [52], [75], and the images show the dramatic decrease in soot formation as the coolant temperature increased. The images also show soot formation is consistently associated with the region near the piston surface for both fuels, and in particular, the area of the piston opposite of the fuel injector. The E0 data show a larger area of the piston is involved in soot formation compared to E100, and this may be due to the formation of a larger pool of fuel on the piston surface for E0. The spray imaging data presented below show more information on spray impingement for these conditions.

Retarding the fuel injection timing decreased the amount of soot formed, as shown previously in Figure 6-2 and Figure 6-3. The average intensity data for SOI of 300 °bTDC (not presented here) showed similar trends for soot formation as those of Figure 6-9. The average intensity data for SOI of 250 °bTDC (not presented here), show little information on soot formation, as the particulate matter was reduced to negligible amounts for all SOI = 250 °bTDC conditions except E0 with coolant temperature of 25 °C.

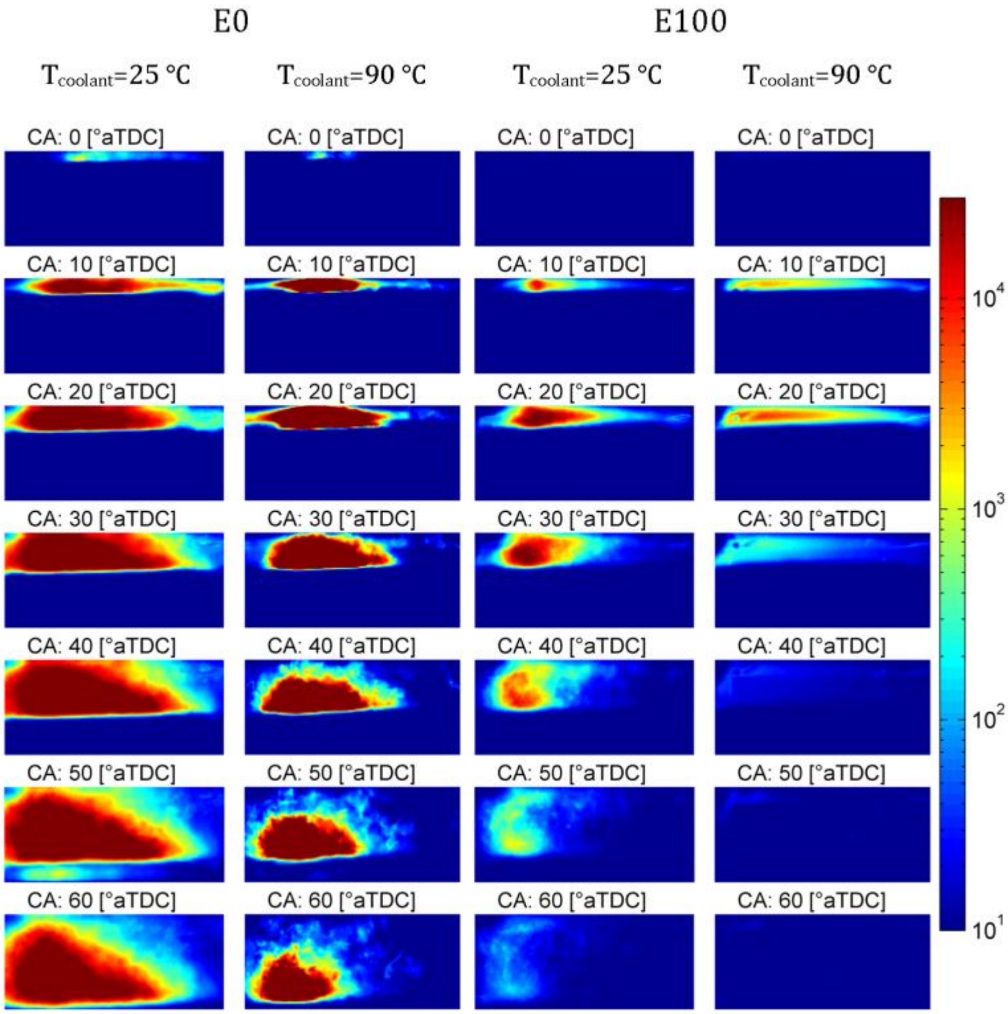

Figure 6-9. Results of combustion and soot imaging for SOI = 320 °bTDC. The false color images are averages of the intensities of 15 cycles. Every 10th CAD is shown.

Cycle-to-cycle Variation in Soot Imaging Data

All the experimental conditions yielded stable $IMEP_n$ with covariance of less than 2%; however, the in-cylinder soot imaging exhibited high cycle-to-cycle variability in some cases. The cycle-to-cycle variation of the spatially integrated soot intensity, maximum heat release rate, and $IMEP_n$ are presented in Figure 6-10 for the two fuels and the fuel injection times of 300 °bTDC and the coolant temperature of 25 °C.

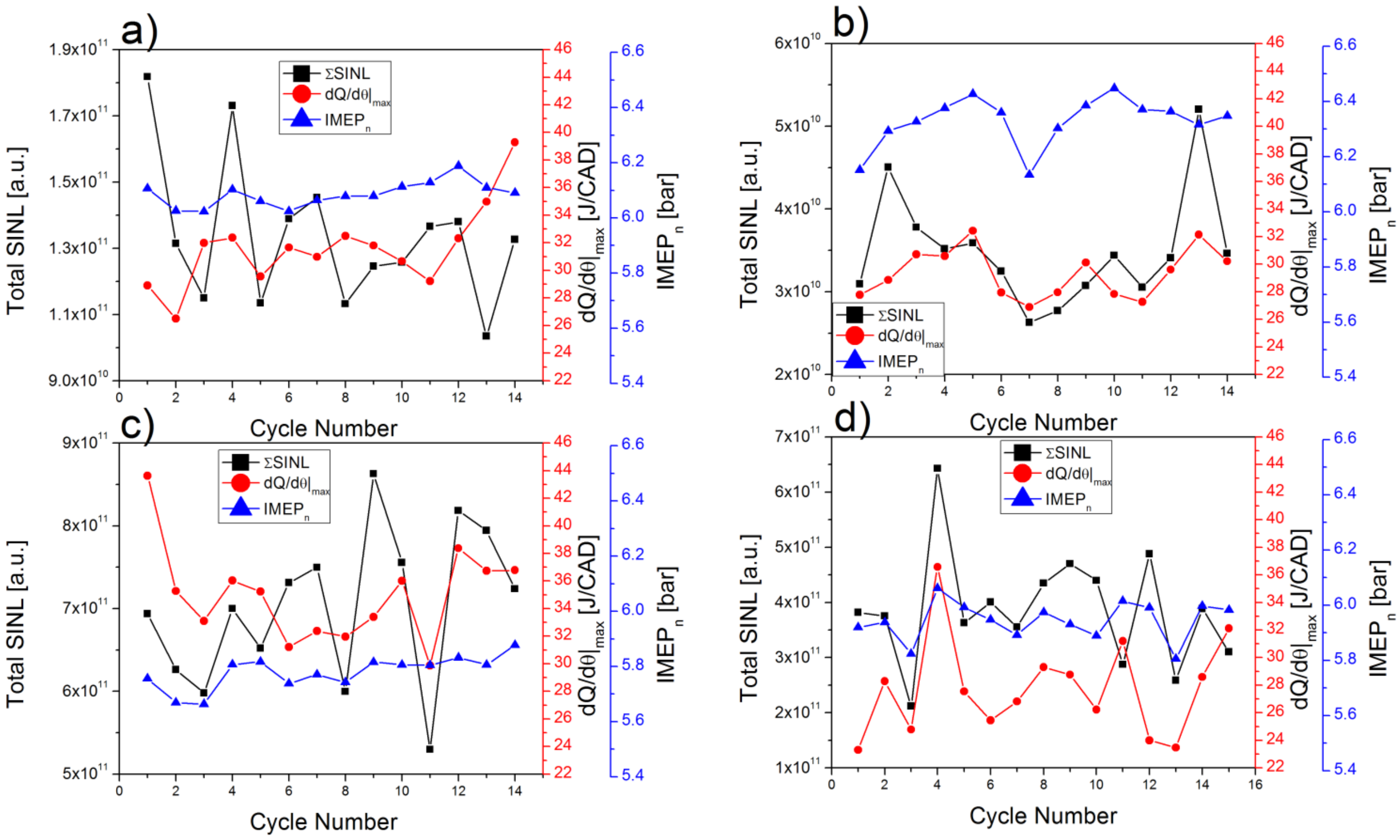

Figure 6-10. SINL, maximum heat release rate, and IMEPn of individual cycles for $T_{coolant}$ = 25 °C. a) E100 with SOI = 320 °bTDC; b) E100 with SOI = 300 °bTDC; c) E0 with SOI = 320 °bTDC; d) E0 with SOI = 300 °bTDC.

The cycle-to-cycle $IMEP_n$ data are very consistent for all conditions; however, the cycle-to-cycle SINL data show large variability (over a factor of 2 in some cases) that does not correlate with either the maximum heat release rate or $IMEP_n$, i.e. the sooting tendency does not correlate with the bulk power performance parameters of the engine. Also note the variation in the SINL is not systematic for any of the operating conditions, e.g. with a steady increase or decrease as a function of the cycle sequence.

In Figure 6-10d), cycles 3 and 4 have dramatically different soot intensity levels, and represent the lowest and highest intensity levels for E0 with SOI of 300 °bTDC and coolant temperature of 25 °C. Figure 6-11 presents the imaging results for these two consecutive cycles. The soot incandescence is distributed throughout the combustion chamber early in the cycle for cycle 4 compared to cycle 3, and cycle 4 shows a larger area of the piston surface is involved in soot formation. Given the soot formation mechanism is attributed to pool fires of fuel films on the piston surface, fuel spray imaging may be expected to provide insight into the cycle-to-cycle variability observed here. As will be shown below, the average spray imaging data do confirm trends in soot formation, but variations in cycle-to-cycle features of the spray could not be identified which might link to the cycle-to-cycle variations in the soot formation, as discussed below.

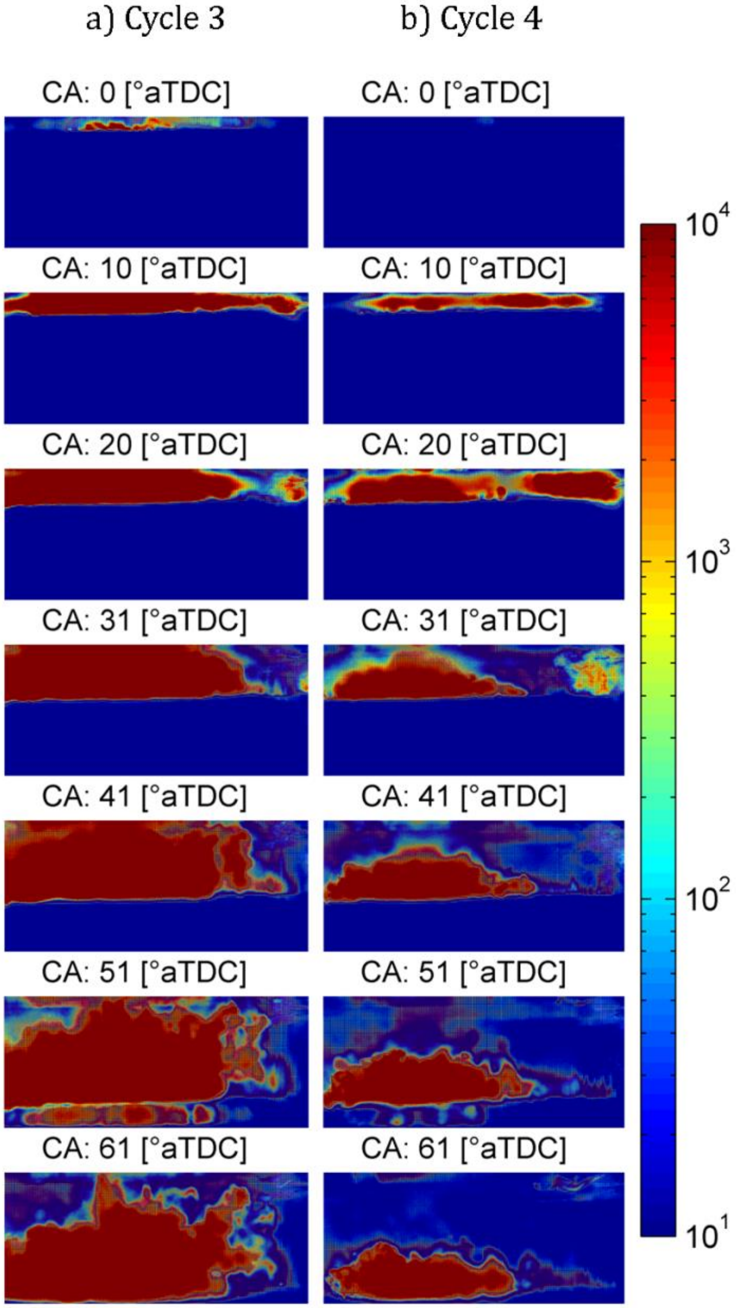

Figure 6-11. Results of imaging data for the two consecutive cycles exhibiting the highest and lowest total SINL for E0 with SOI at 300 °bTDC at 25 °C. a) cycle 3 with $IMEP_n$= 5.82 bar; b) cycle 4 with $IMEP_n$=6.08 bar.

Fuel Spray Imaging

The soot imaging data indicate the in-cylinder soot formation is due to pool fires caused by fuel wetting of the piston surface and possibly the cylinder walls. As noted earlier, 25 mm of the top portion of the cylinder liner is transparent, and the fuel spray impingement with the piston surface and cylinder walls could only be observed for the earliest fuel injection timing (SOI = 320 °bTDC) which was also the highest sooting condition. The images were enhanced to identify the liquid part of the spray and especially focus on the spray interaction with the piston surface. An example of the results for the fuel spray imaging is shown in Figure 6-12 for E100 with SOI at 320 °bTDC and $T_{coolant}$ = 90 °C. The image corresponds to a frame taken 10 CAD after the SOI. The dense liquid core of the spray is the saturated part of the image. The impingement and roll-up of the fuel spray from the piston surface is clearly visible in the image.

Figure 6-12. Unprocessed still image of the fuel spray at 310 °bTDC (10 CAD after SOI) for E100 with SOI = 320 °bTDC and $T_{coolant}$ = 90 °C.

The averaged imaging results for the fuel spray are shown in Figure 6-13 for SOI = 320 °bTDC at 25 °C and 90 °C for E100 and at 90 °C for E0. Note that because the heating value of indolene is higher than that of E100, the fuel injection duration was longer for E100 compared to E0, so the spray persists for a longer period of time in the E100 images. Imaging results for E0 at SOI = 320 °BTDC and a coolant temperature of 25 °C are not presented, because the soot deposition onto the transparent cylinder liner occurred so rapidly that the features of the fuel spray were obscured.

As seen in Figure 6-13, at the early fuel injection time of 320 °bTDC, there was significant fuel impingement on the piston for both fuels. Comparison of the spray imaging data with the soot formation data of Figure 6-9 indicate the difference in the spray roll-up is related to the pool fires on the top of the piston. At the colder coolant condition for E100, the amount of fuel visible bouncing off the piston top is significantly lower than for the hotter coolant condition for E100, indicating more liquid fuel remains on the piston top [76]. The lower piston temperature also delays the vaporization of fuel and therefore the possibility of localized fuel rich regions near the piston increases.

The angle of the spray roll-up for E100 is larger than that of E0 for $T_{coolant}$ = 90 °C. The larger roll up angle is expected to generate more mixing with the piston motion, thus suppressing soot formation for E100. The E0 spray data show the fuel stays close to the piston surface and covers a larger area of the piston surface. The E0 data also indicate the rebound of the fuel spray is on a trajectory where the liquid fuel may impinge on the cylinder wall, creating another potentially fuel rich zone.

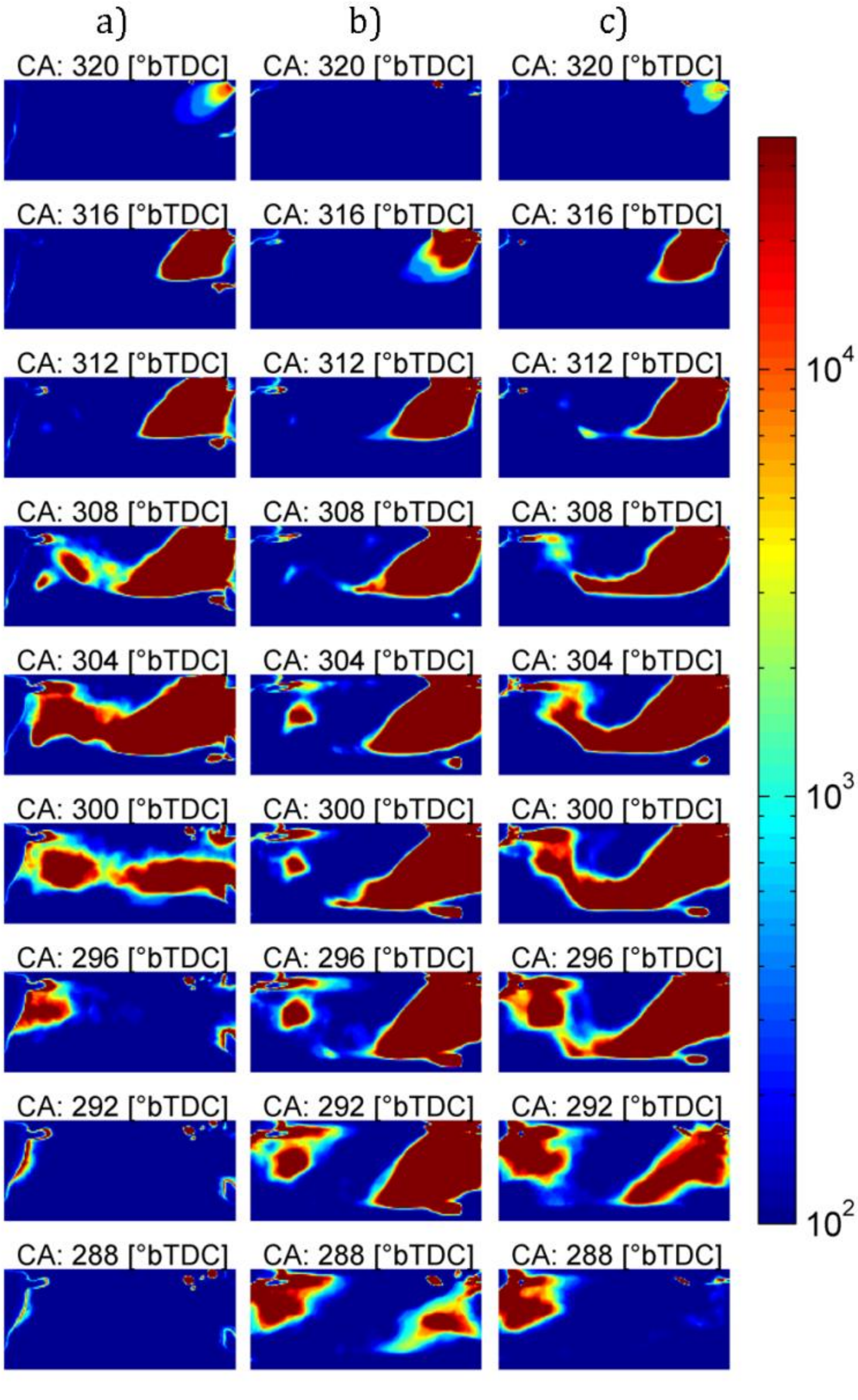

Figure 6-13. Results of spray imaging for SOI = 320 °bTDC. The false color images are averages of the intensities of 15 cycles: a) E0 with $T_{coolant}$ = 90 °C; b) E100 with $T_{coolant}$ = 25 °C; c) E100 $T_{coolant}$ = 90 °C. Every 4th CAD is shown. As shown earlier in Figure 6-9, the highest soot emissions correspond to a) and the lowest soot emissions (of these 3 conditions) correspond to c).

Examples of the cycle-to-cycle variation in the in-cylinder soot formation presented in Figure 6-10 and Figure 6-11 may be due to small variations in the fuel spray pattern and/or variations in spray impingement with the piston surface and cylinder walls. Unfortunately, while the bulk features of the fuel spray are apparent in the imaging data, variation in the detailed features are not well resolved by the Mie scattering approach used in this study. The spatial integrated luminosity of the spray frames were analyzed and the cycle-to-cycle variations seemed uncorrelated with the SINL of the combustion and soot data. Further work, which focuses on the near piston and near wall regions or direct measurements of the fuel films may yield more insight on the key fuel spray features leading to cycle-to-cycle variation in the soot formation.

6.4 Conclusions

The effects of fuel, coolant temperature and fuel injection timing on in-cylinder and engine-out gas particulate emissions in an optically accessible DISI engine were investigated. High speed imaging data were used to quantify the in-cylinder soot formation and features of the fuel spray, and soot opacity measurements were made to quantify particulate matter in the engine-out exhaust gases.

- The in-cylinder soot imaging data, obtained by spatially integrating the natural luminosity (SINL), correlated well with the engine-out smoke measurements.
- E100 produced over an order of magnitude less soot (based on quantitative imaging metrics of soot thermal incandescence) at all operating conditions compared to E0.
- E100 produced measureable in-cylinder soot and soot mass at cold coolant and early injection timing conditions.

- High coolant temperatures dramatically decreased in-cylinder soot formation at every fuel injection timing for both fuels.
- Retarding fuel injection timing decreased in-cylinder soot formation for both fuels at both coolant temperatures.
- In-cylinder soot formation was associated with fuel impingement on the piston surface, as indicated by the fuel spray imaging, and E0 showed a larger region of the piston was wetted by the fuel for a longer period of time compared to E100 for the most advanced fuel injection times studied.
- The features of the fuel spray roll-up, including the amount of fuel rebounded from the piston surface and the angle of the roll-up were identified as indicators of in-cylinder soot formation with higher rebound of fuel off the piston surface resulting in reduction of fuel film area and thickness on the piston surface.

Chapter 7

Spray Development and Cylinder and Piston Impingement in a DISI Engine

7.1 Objective

The reduction of soot observed with the ethanol blends (Chapter 5) and pure ethanol (Chapter 6) experiments may be due to the intrinsic chemistry effects of an alcohol. However, the effects may also be due to the spray characteristics and surface wetting of the fuels. The objective of this study was to investigate how the different fuels and operating conditions affect the spray development and fuel impingement with the cylinder wall. The experiments were conducted to capture the full view of the fuel spray interaction with the cylinder wall. The optically accessible single cylinder DISI engine was equipped with a full length transparent liner to acquire high speed imaging data of fuel spray and impingement as a function of fuel blend, the fuel rail pressure, and engine coolant temperature. The fuel injection timing was retarded to isolate the effects of wall impingement.

7.2 Experimental Approach

This study was conducted using the DISI single cylinder optical research engine facility of the University of Michigan, which is described in Section 2.2. Orthogonal imaging of the full combustion chamber imaging was performed to investigate the spray development and the impingement with the cylinder wall and piston. The engine setup schematic is shown in Figure 7-1.

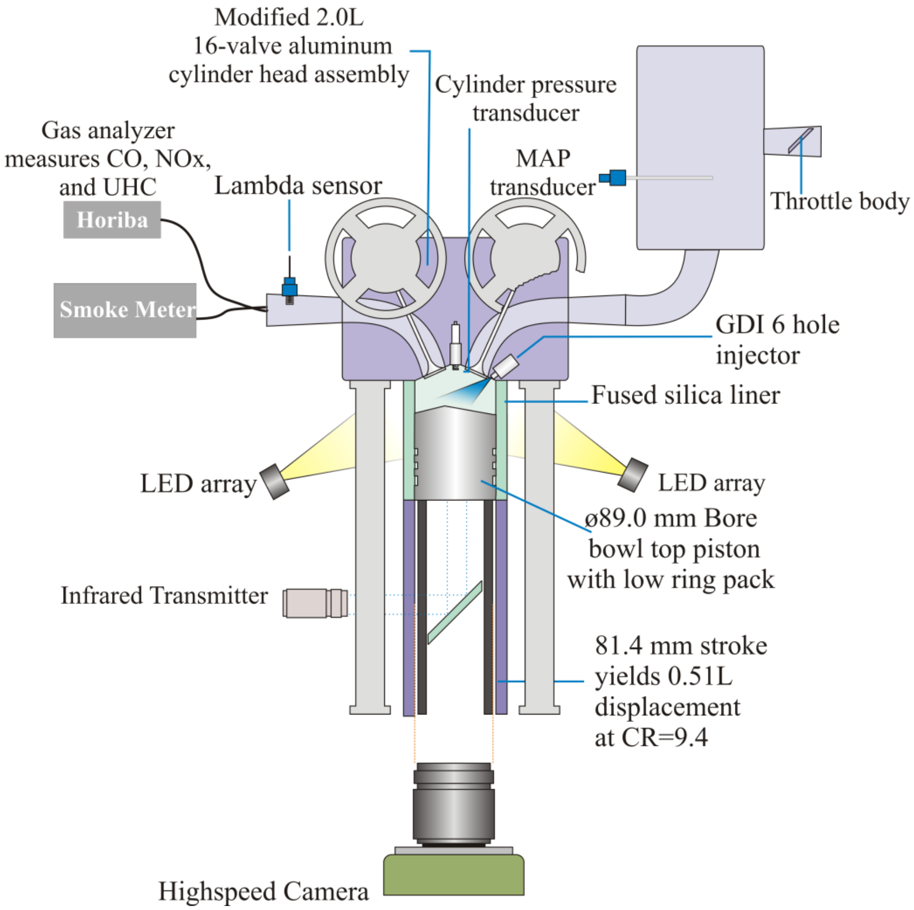

Figure 7-1. Schematic of the optical DISI engine setup configured for orthogonal imaging of the full combustion chamber.

The standard metal liner for the engine cylinder was replaced with a transparent fused silica liner which enabled side-view imaging of the whole combustion chamber. The imaging was performed from the flywheel side (orthogonal to the spray plane) through the fused silica liner using a CMOS high speed camera (Vision Research Phantom v7.11, color). The camera was focused on the center of the combustion chamber using a 105 mm macro lens (Nikkor, 105 mm f2.8 d) and a 14mm Nikon extension tube (PK-12) at f4.0 to optimize the depth of field and light exposure to the sensor. A spatial resolution of 912x800 pixels at 9000 frames per second and an exposure time of 100 μs were used for the study, resulting in 1 frame per CAD.

Two LED lights (1x3 high intensity LED arrays) located on the intake and exhaust sides were used to light the combustion chamber to allow imaging of the fuel spray. The imaging data captured the fuel spray by scattering of the LED light. No additional spectral filters were used other than the inherent spectral characteristics of the camera sensor and the collection and focusing optics. The imaging data from the high speed camera were synchronized with the pressure data using a trigger signal. A total of 11000 frames were recorded for each experimental condition which corresponded to 15 consecutive spray cycles.

Three coolant temperatures and two fuel rail pressures (FRP) were studied as part of this work. The piston surface temperature and the liner outer temperature were measured to determine the thermal variation during the experiments. The manifold absolute pressure was controlled at 57 kPa for all experiments at 1500 RPM. After stable motoring was achieved, firing signals were sent to the fuel injector and spark systems. In order to avoid soot deposition on the liner, lean combustion at an equivalence ratio of ϕ = 0.80 was targeted for the experiments with the coldest coolant conditions studied , and the spark timing and fuel injection duration were kept the same for the rest of the experiments. As the coolant temperature increased, the equivalence ratio increased to ϕ = 0.90 using the same fuel injection duration. This is due to an increase in injector discharge coefficient that occurs due to a decrease in fuel viscosity at higher temperatures [77], [78]. As will be shown below, the increase in equivalence ratio at higher coolant temperatures had a stabilizing effect on the engine.

Image Analysis

The in-cylinder spray images were analyzed to quantify the development of the spray as well as impingement of the spray with the cylinder wall. The raw images were processed by eliminating of the background and stray reflection and transforming the images to gray scale. The resulting intensity maps were used to investigate the spray development and atomization/vaporization of the spray plume. When interpreting the spray images, the following assumption were made.

- The imaging data are due to scattering of the LED light by fuel droplets only; therefore signal intensity correlates with the amount of liquid fuel present.
- The decrease in signal intensity in the immediate region surrounding the fuel spray is due to fuel vaporization.

The Spatially Integrated Luminosity (SIL) was defined to quantify the temporal changes in the spray intensity and was calculated based on spatial integration of the intensity maps over time ($\mathrm{SIL} = \iint I_{pix}(t)dx\,dy$). The SIL was used as an indication of liquid fuel.

The edge of the spray plume was detected using a Laplacian 5x5 transformation of the images and was used to quantify the spray cone angle and the spray tip penetration. An example of the outcome of the image processing is shown in Figure 7-2. The series of raw images shown in left column were from experiments with E100 at 25 °C coolant temperature with SOI=250 °aTDC. Every 5th frame is presented. The middle column shows the intensity map in false color scale of each frame after subtracting the background, and the right column shows the resulting edge detection transformation of the images.

In order to quantify the spray impingement with the cylinder wall, a column of pixels near the liner was chosen as a hypothetical boundary. High intensity signals that pass the hypothetical boundary are indications of fuel that will impinge on the cylinder liner. The rebound of fuel spray off the surface of the liner would artificially affect the results if a region closer to the liner surface was selected for this analysis. Therefore, the boundary column had to be away from the inner surface for the calculation of the fuel impingement.

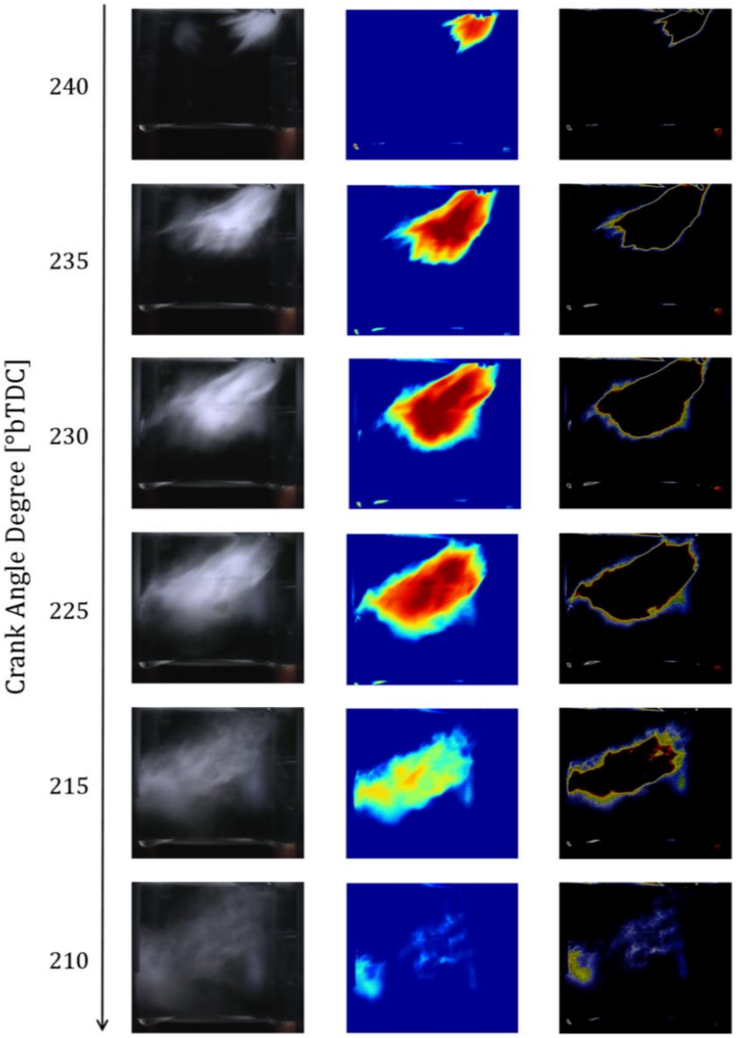

Figure 7-2. Example of the spray image processing: (left column) sequence of original images, as recorded; (middle column) background elimination and conversion to intensity map in false scale; (right column) edge detection of the fuel spray using a 5x5 Laplacian transformation. For each column, every 5th image is shown.

After performing a sensitivity analysis to the location of the boundary, 3.5 mm away from the inner surface of the liner was chosen for the calculations. The intensity values were integrated along this boundary over time to quantify the flux of fuel that impinges on the wall. The metric was called the Line Integrated Luminosity ($\mathrm{LIL} = \int I_{Boundary}(t)\, dy$). The assumptions used are:

- A constant fraction of fuel impinging on the surface wets the surface regardless of the angle of impingement.
- The boundary is far enough from the wall that the rebound of the droplets does not cross the boundary again.

Spray imaging from the exhaust side presented in Chapter 5 (parallel to the injection plane- looking into the fuel injector) indicated that the spray plumes were symmetrical with respect to the cylinder centerline. Therefore, the wetted surface of the cylinder wall was quantified as the projected height of the conic section of the spray intensity at the boundary (L_{wet}).

7.3 Experimental Results

The effects of fuel injection timing, coolant temperature and fuel rail pressure on the fuel spray development and impingement with the cylinder wall and piston top were investigated for E0, E50 and E100. The fuel injection timing of 250 °bTDC was studied for each fuel at coolant temperatures of 25°C, 60°C and 90°C. The effect of fuel rail pressure was investigated by performing the experiments with fuel rail pressures at 100 and 150 bar. The operating conditions and the experimental results are reported in Table 7-1 where the values are averaged over ~67 cycles at each operating condition. The UHC and CO emission results indicate that the combustion efficiency did not change significantly between the experiments and miss-firing cases were not observed; however, the variability in the combustion phasing and peak pressure data indicate significant cycle-to-cycle variation at the colder coolant condition. As discussed before, this is partially due to the stabilizing effect of increasing equivalence ratio that occurs at higher coolant temperatures.

The imaging data were averaged over the 15 spray cycles at the same crank angle to generate average intensity maps of spray development. The results are shown in Figure 7-3 for E0, E50 and E100 at coolant temperature of 25 °C, FRP = 100 bar and SOI of 250 °bTDC. Every 4th CAD is shown in the figure.

Table 7-1. Operating conditions and results of engine performance and engine-out emissions for different fuel blends, coolant temperatures and fuel rail pressures.

Fuel	$T_{coolant}$	FRP	PW	ϕ	P_{max}	σ_{Pmax}	$IMEP_n$	COV_{IMEPn}	CA50	σ_{CA50}	NOx	UHC	CO
-	[°C]	[bar]	[ms]	-	[bar]	[bar]	[bar]	[%]	[°aTDC]	[°aTDC]	[ppm]	[ppm]	[%]
E0	27	100	1.15	0.83	12.49	2.09	2.80	11.3	384.0	5.9	61	591	0.09
E0	63	100	1.15	0.87	16.71	2.43	3.06	3.4	374.3	5.5	349	640	0.09
E0	90	100	1.15	0.90	19.51	2.23	3.03	15.4	369.2	7.4	1157	537	0.12
E0	28	150	0.87	0.80	9.44	1.17	1.99	26.9	392.1	4.9	1	602	0.24
E0	60	150	0.87	0.80	10.70	1.86	2.25	22.4	387.6	6.6	9	581	0.10
E0	88	150	0.87	0.81	13.04	2.11	2.47	5.7	379.2	5.3	101	506	0.08
E50	23	100	1.40	0.82	12.08	2.10	2.68	24.1	385.2	8.6	9	616	0.06
E50	59	100	1.40	0.85	16.28	2.12	2.99	1.9	374.2	4.7	-	-	-
E50	89	100	1.40	0.87	17.23	1.81	3.05	2.1	372.6	3.9	391	460	0.07
E50	29	150	1.12	0.86	12.24	1.73	2.84	5.9	384.0	4.9	18	485	0.07
E50	60	150	1.12	0.90	15.91	1.61	2.96	2.0	374.7	3.4	142	381	0.09
E50	89	150	1.12	0.87	16.15	1.83	2.94	3.2	374.6	3.9	256	329	0.08
E100	26	100	1.80	0.85	11.61	2.04	2.86	10.5	387.1	6.0	0	701	0.08
E100	61	100	1.80	0.89	15.85	1.84	3.15	2.3	376.0	4.0	-	-	-
E100	89	100	1.80	0.89	19.78	1.58	3.25	1.6	368.8	3.0	285	389	0.09
E100	25	150	1.40	0.83	10.17	1.58	2.44	21.5	389.9	6.7	0	716	0.13
E100	58	150	1.40	0.86	14.64	1.73	3.00	2.6	377.8	4.0	0	392	0.10
E100	87	150	1.40	0.87	17.37	1.66	2.91	2.0	370.9	3.5	90	416	0.12

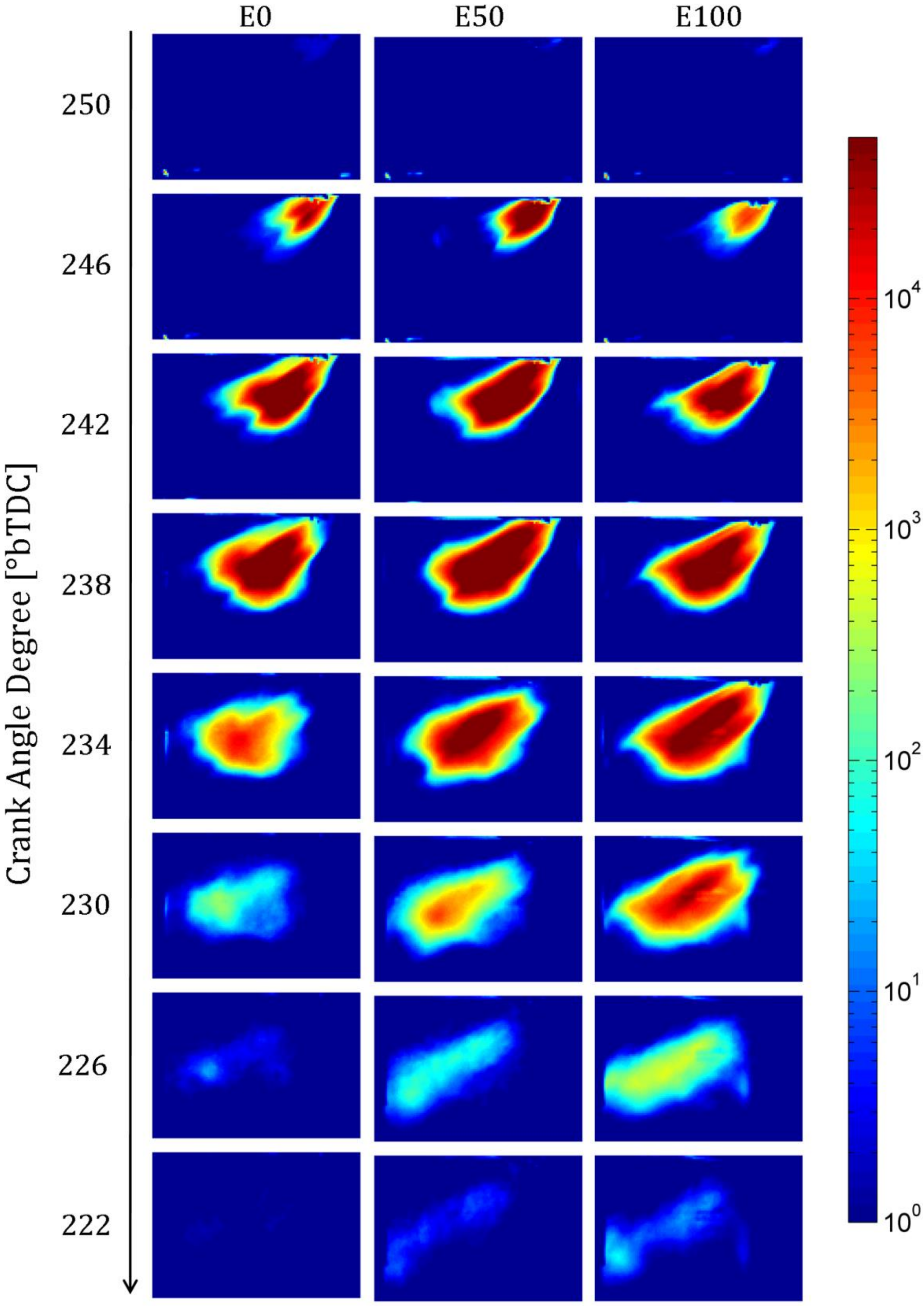

Figure 7-3. Results of fuel spray imaging for SOI = 250 °bTDC, $T_{coolant}$ = 25 °C, and FRP=100 bar. The false color images are averages of the intensities of 15 cycles. Every 4th CAD is shown.

The average intensity maps highlight the differences between the spray plumes. The fuel injection durations for the cases presented in Figure 7-3 correspond to E0:10.35 CAD, E50:12.6 CAD and E100:16.2 CAD. The penetration distance is similar for the fuels until the EOI, but the E0 fuel spray exhibited a wider cone angle compared to the ethanol blends. The wall impingement for the E0 is considerably less than the other fuels. To investigate these characteristics further, the results of the spatially integrated luminosity (SIL), the line integrated luminosity (LIL) at the boundary, and the length of the wetted surface (L_{wet}) are shown in Figure 7-4. The error bars represent the standard deviation of the cycle-to-cycle variation. The SIL values indicated much less cycle-to-cycle variation compared to the LIL and L_{wet} values, which shows the robustness of the bulk feature of the spray. Higher variability in the LIL values shows the sprays results in local changes in the spray features near the wall.

Comparing the intensity maps and SIL values indicate that the EOI (last frame with visible spray at the injector tip) coincide with the maximum SIL value. The vaporization of fuels after this point decreases the SIL to the background level. The duration of the fuel vaporization process was similar for E0 and E50, but E100 resulted in shorter vaporization time even though the E100 has a higher enthalpy of vaporization compared to E50 and E0.

The injector used in the experiments targeted two sprays on the spark plug area. The collapse timing of the sprays affects the wall impingement location. As the spray intensity maps in Figure 7-3 indicated, the E0 spray had a much wider spray tip and less impingement with the wall, which was quantified by the data LIL shown in Figure 7-4. The differences in the magnitude of the LIL data of the fuels is an indication of the spray flux through the boundary, and the LIL results show E0 had significantly less impingement with the wall. The wetted length, which is the projected length of the wetted area, is shown in the bottom panel of Figure 7-4.

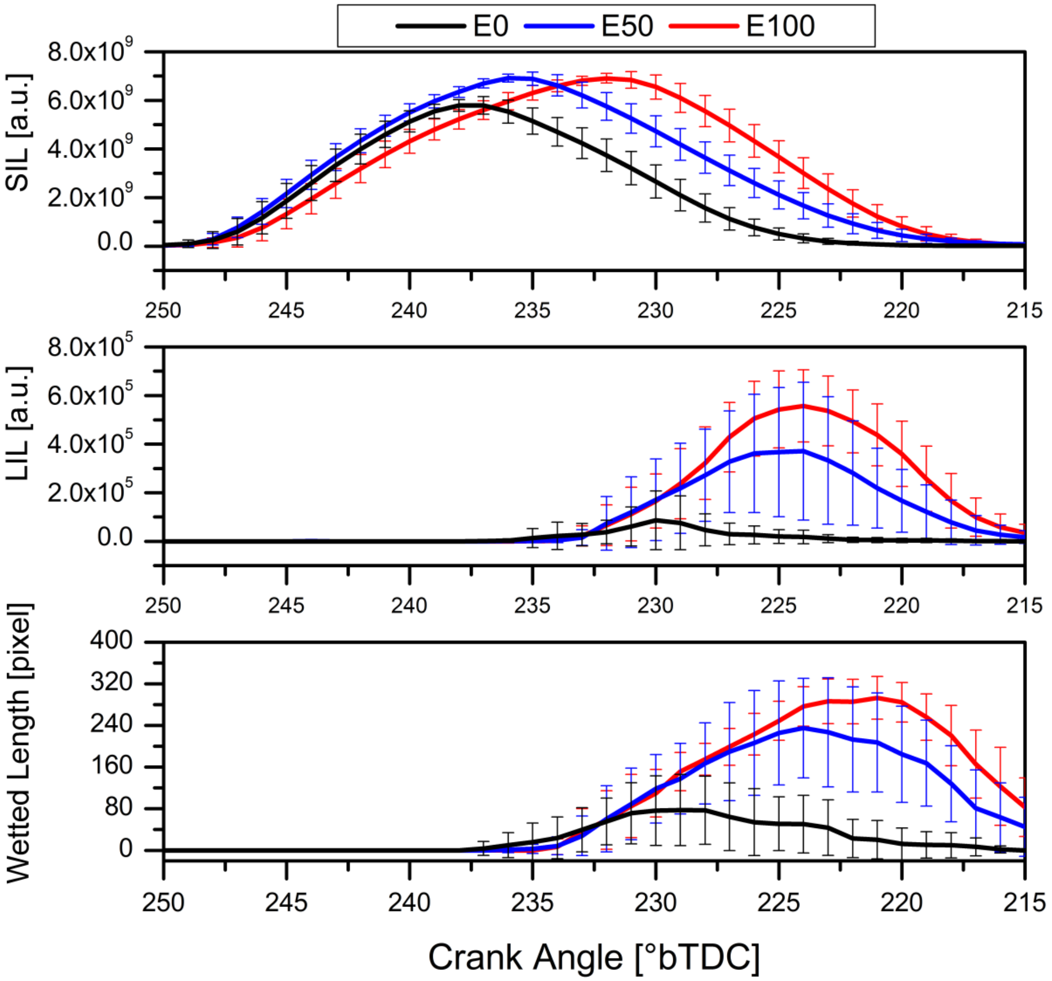

Figure 7-4. Results of average SIL (top); LIL (middle); wetted length (bottom) of the sprays with SOI = 250 °bTDC and $T_{coolant}$ = 25 °C at FRP=100 bar.

Effects of Coolant Temperature

The coolant temperature affects the fuel temperature. Because of the low thermal mass of the fuel in the injector and the high conductive heat transfer between the fuel injector and the cylinder head, the fuel was assumed to reach the same temperature as the cylinder head. Considering the distillation curve of the fuel, approximately 35% of E0 components are volatile at temperatures less than 90° C (see Table 2-1) and the percentage of volatile component increases as the ethanol concentration in the blend increases [54], [55]. Therefore different coolant temperatures change the volatile portion of the fuels and impact the spray characteristics of the fuel. The effect of coolant temperature on spray development is shown in Figure 7-5. The results show the spray average intensity maps for coolant temperatures of 60° C and 90° C with FRP = 100 bar and SOI of 250 °bTDC. The increase of coolant temperature from 60° C to 90° C changes the spray pattern of E0 significantly by narrowing the cone angle, which is attributed to increased vaporization of the fuel and reduced liquid portion of the spray. The increase in fuel temperature reduces the kinematic viscosity of the fuel and therefore reduces the viscous forces which resulted in higher rates of penetration and narrower cone angle. The same trend is observed for E50 with lower magnitude, but the cone angle for E100 seems largely unaffected. This is because the coolant temperature is below the boiling point of ethanol. The higher sensitivity of E0 to changes in coolant temperature was observed in the soot studies reported in Chapter 5 as well. The dominant factor in the soot formation was concluded to be the spray impingement with the piston surface. A narrower liquid portion of the spray indicates more fuel/air mixing and potentially wetting a smaller area of the wall and piston. Therefore the higher sensitivity of E0 to coolant temperature on soot formation may be attributed to the characteristics of the sprays, as opposed to the fuel chemistry.

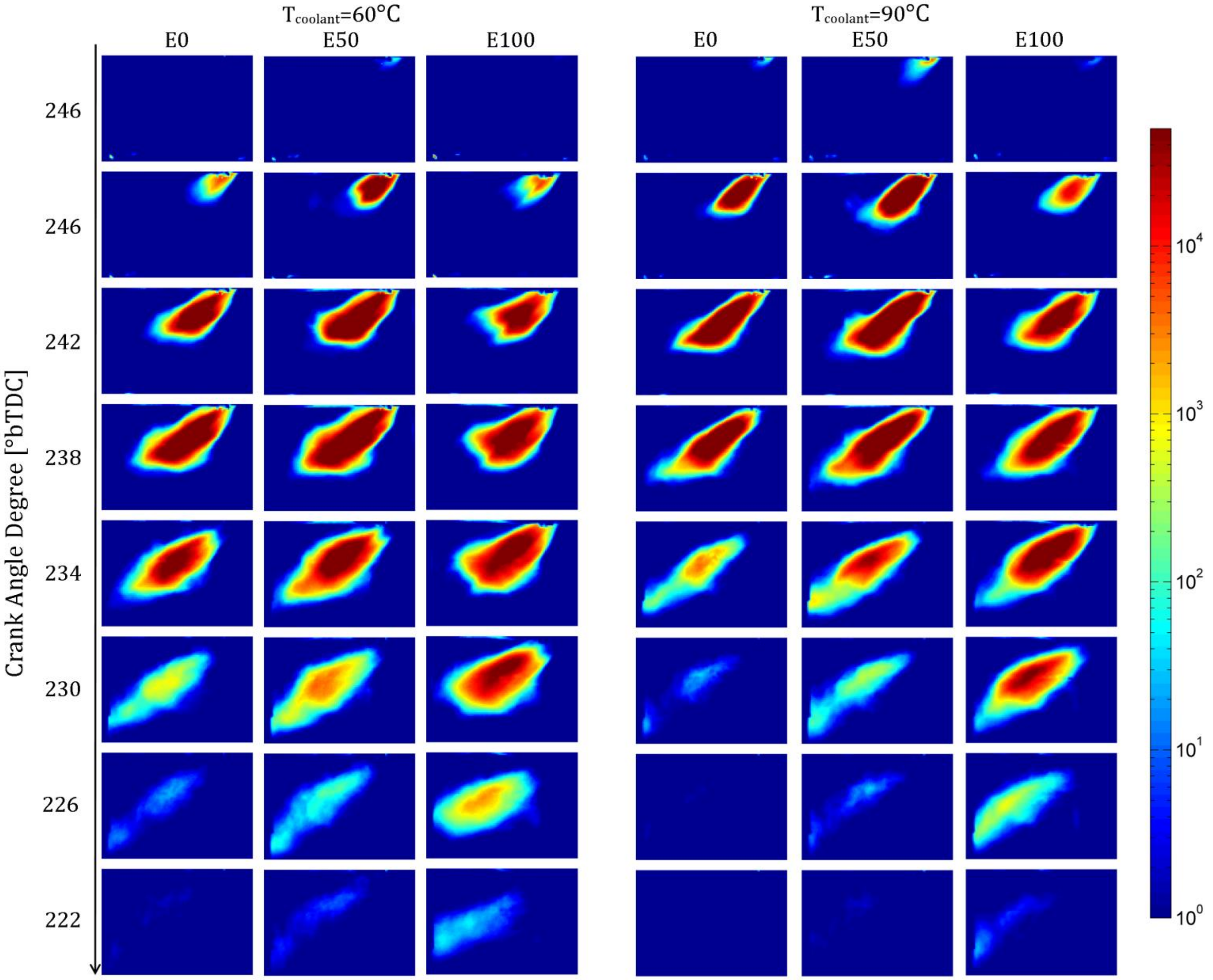

Figure 7-5. Results of spray imaging for the fuels at coolant temperature of 60 °C (left) and 95 °C (right) with SOI = 250 °bTDC and FRP=100 bar. The false color images are averages of the intensities of 15 cycles. Every 4th CAD is shown.

The results for average SIL, LIL and wetted length of the sprays for different coolant temperatures are shown in Figure 7-6. The magnitude of SIL was reduced slightly as the coolant temperature increased which was a result of less liquid fuel. The impingement quantified by LIL indicates that the spray reaches the boundary approximately 5-7 CAD earlier at conditions with $T_{coolant}$=90° C. While the impingement and wetted length increase significantly for E0, the changes were not significant for E100.

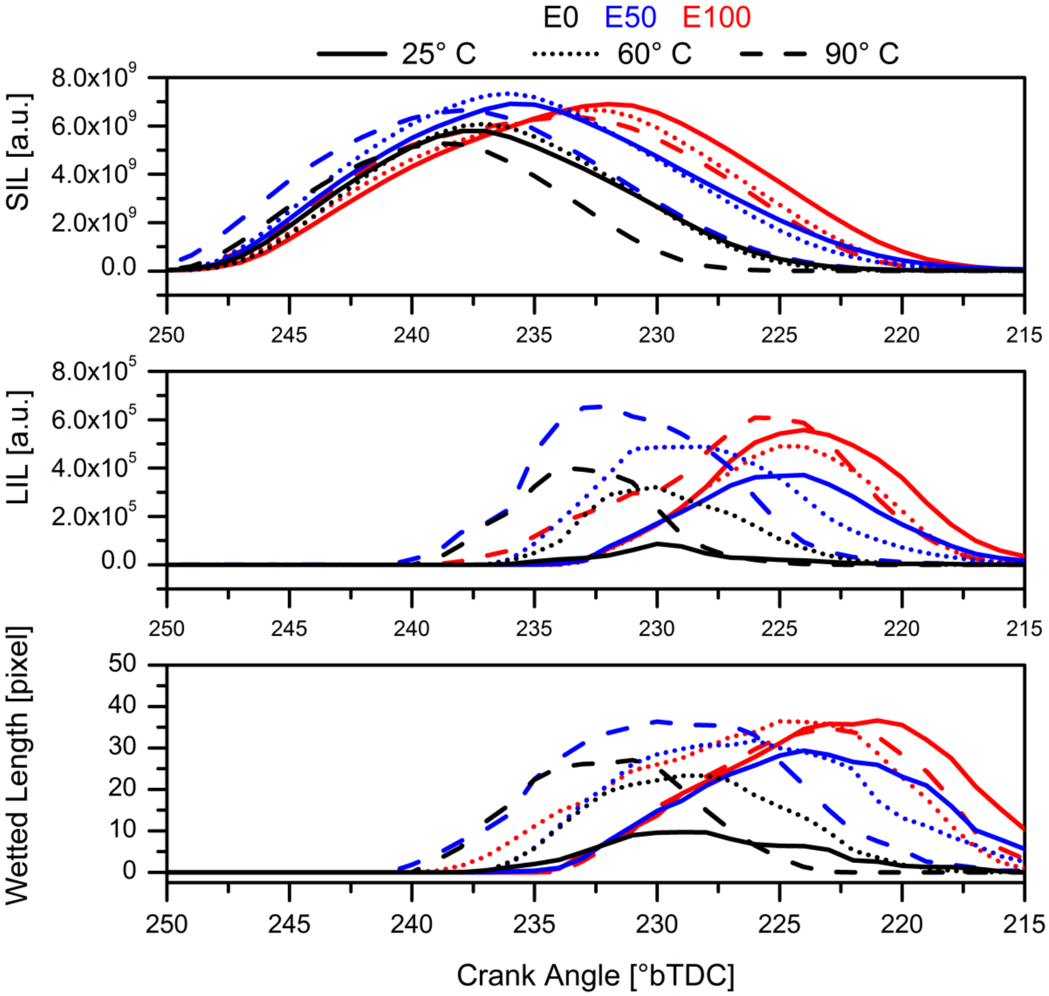

Figure 7-6. Results of average SIL (top); LIL (middle); wetted length (bottom) of the sprays for different coolant temperatures with SOI = 250 °bTDC at FRP=100 bar.

While the changes in SIL due to changes in coolant temperature were small for a particular fuel, the intensity maps indicated significant changes in the spatially resolved features of the sprays and the resulting impingement. The scattering signal intensity at the virtual boundary used to measure the fuel flux to the combustion chamber wall is presented in Figure 7-7 as a function of crank angle after SOI. The results show the effect of coolant temperature on the fuel flux as a function of time for E0 and E100. The same intensity contour lines are applied to all panels. The earliest impingement for the 25° C coolant condition for both fuels happens at the top half of the liner (although the intensity of E0 impingement is low), which is an indication of faster penetration of the sprays from the top two nozzle holes. At the 90° C coolant condition, the individual sprays collapse into a denser and narrower plume along with the injector centerline and the earliest impingement location is physically lower on the cylinder wall.

Fuel temperature effect on the in-nozzle cavitation of the injector has been identified to be an important parameter in the spray formation. Aleiferis et al. [79] observed cavitaion in a real size optical injector, which affected the high volatility components of the fuel mixture by creating nucleation sites for vaporization of the low boiling point fraction of the fuel. The nonlinear effect of temperature on viscosity, surface tension and vapor pressure of each fuel creates a very complex phenomena of cavitation, spray break-up and rate off vaporization of sprays.

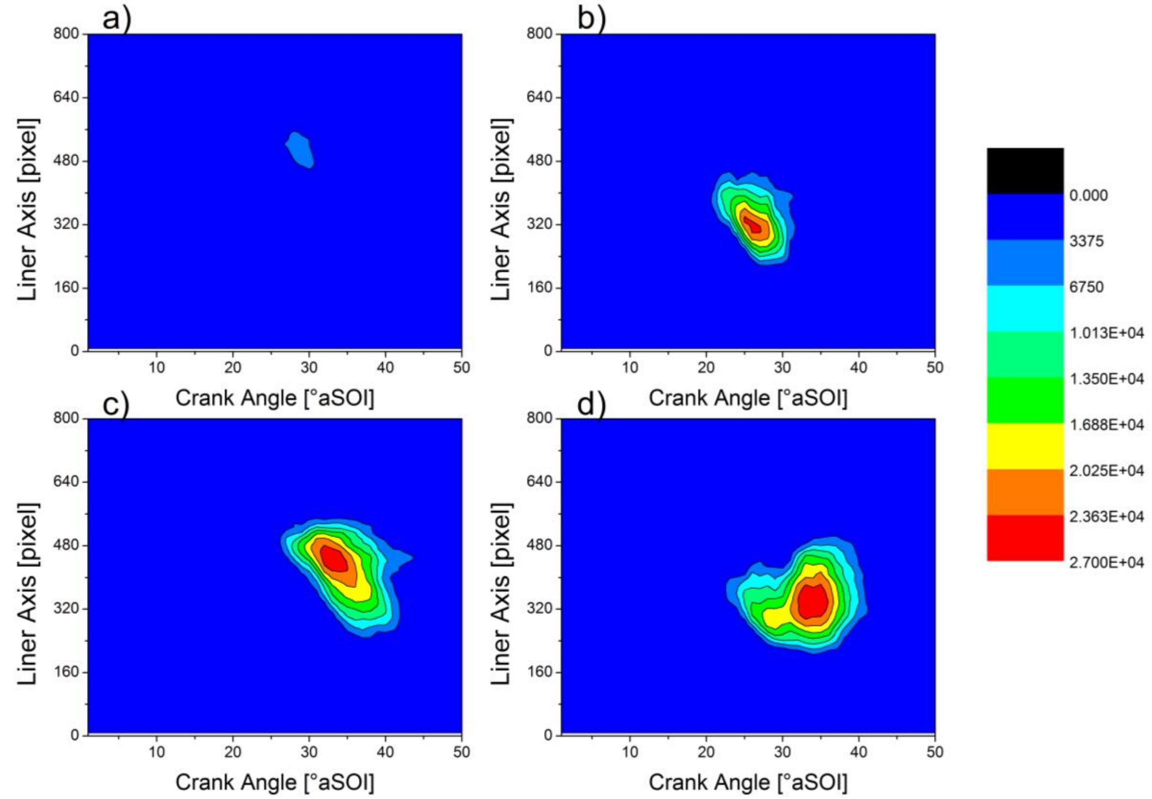

Figure 7-7. Scattering signal intensity at the virtual boundary used to measure fuel flux to the combustion chamber wall as a function of crank angle after SOI. a) E0-25° C; b) E0-90° C; c) E100-25° C; d)E100-90° C with SOI = 250 °bTDC at FRP = 100 bar.

Effects of Fuel Rail Pressure

The fuel rail pressure affects the discharge rate of the fuel and atomization. To investigate the effects of fuel pressure on spray development and wall impingement, the fuel rail pressure was increased to 150 bar and the targeted stoichiometry was kept constant, which resulted in reduced injection duration. The decrease in injection duration was linear for all the fuels (see Table 7-1). Figure 7-8 shows the results of the intensity maps for E0 and E100 with FRP of 100 bar and 150 bar at coolant temperatures of 25° C. Every 4th CAD is shown and the same color scale is applied to each image.

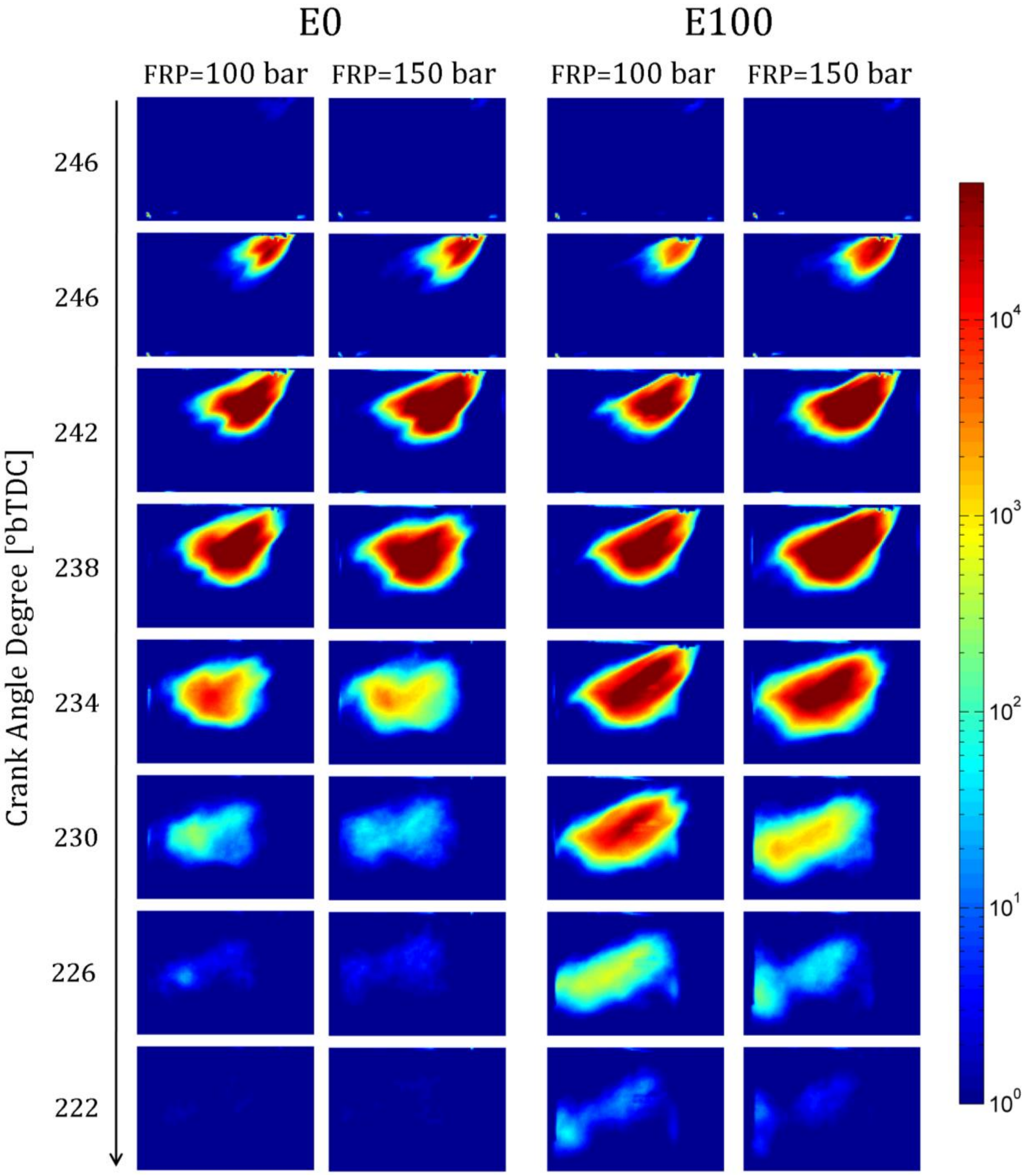

Figure 7-8. Results of spray imaging for E0 (left) and E100 (right) as a function of FRP. Coolant temperatures at 25°C with SOI = 250 °bTDC. The false color images are averages of the intensities of 15 cycles. Every 4th CAD is shown.

The increase of FRP resulted in wider spray cone angles for both fuels, especially at the colder coolant condition. The flash boiling of the smaller droplets at higher temperature narrows the plume angle. The results for average SIL, LIL and wetted length of the sprays at 25 °C with FRP = 100 bar and 150 bar are shown in Figure 7-9. Given the same equivalence ratio, the same amount of fuel was being injected in a shorter period of injection, which is being indicated by an increase in the peak SIL values. Although the peaks of SIL occur earlier (indication of EOI) at the high FRP, the overall vaporization times do not change for either of the fuels and the impingement increases significantly both in terms of flux across the boundary as well as the wetted length as FRP increases. An increase in the coolant temperature exhibited the same effects regardless of the FRP for both fuels.

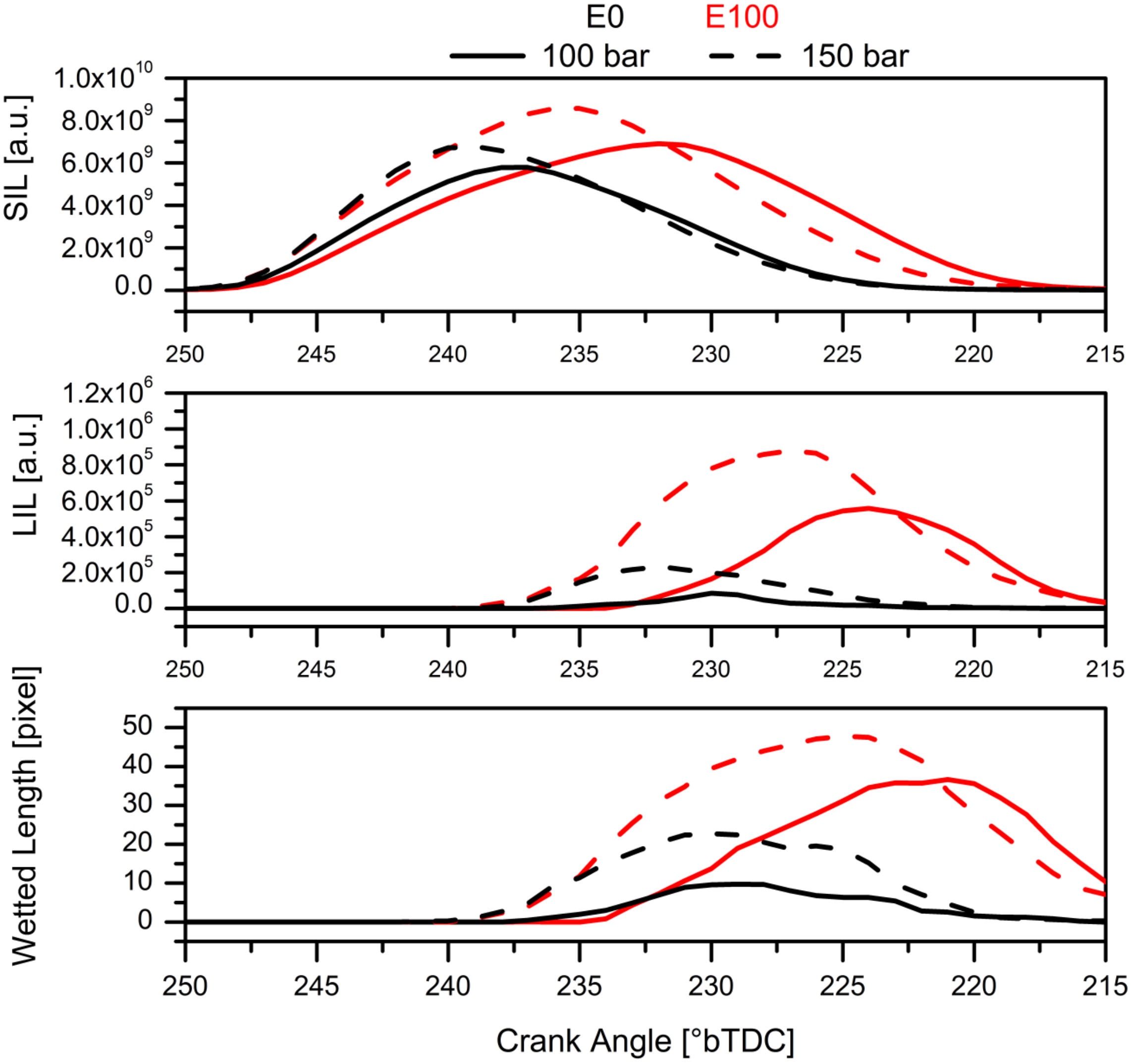

Figure 7-9. Results of average SIL (top); LIL (middle); wetted length (bottom) of the sprays at FPR of 100bar and 150bar for E0 and E100 with SOI = 250 °bTDC.

The scattering signal intensity at the virtual boundary used to measure the fuel flux to the combustion chamber wall is presented in Figure 7-10 as a function of crank angle after SOI. The same color scale used in Figure 7-7 is used in Figure 7-10. The location of the impingement does not change, but the projected length of wetted surface increased compared to lower FRP conditions. The overal intensity of impingement and the duration of high intensity flux through the boundary increased at high FRP conditions. The total amount of liquid fuel across the boundary increased for higher FRP but the fuels did not exhibit different sensitivities to FRP, despite significantly higher kinematic viscosity of E100 compared to E0.

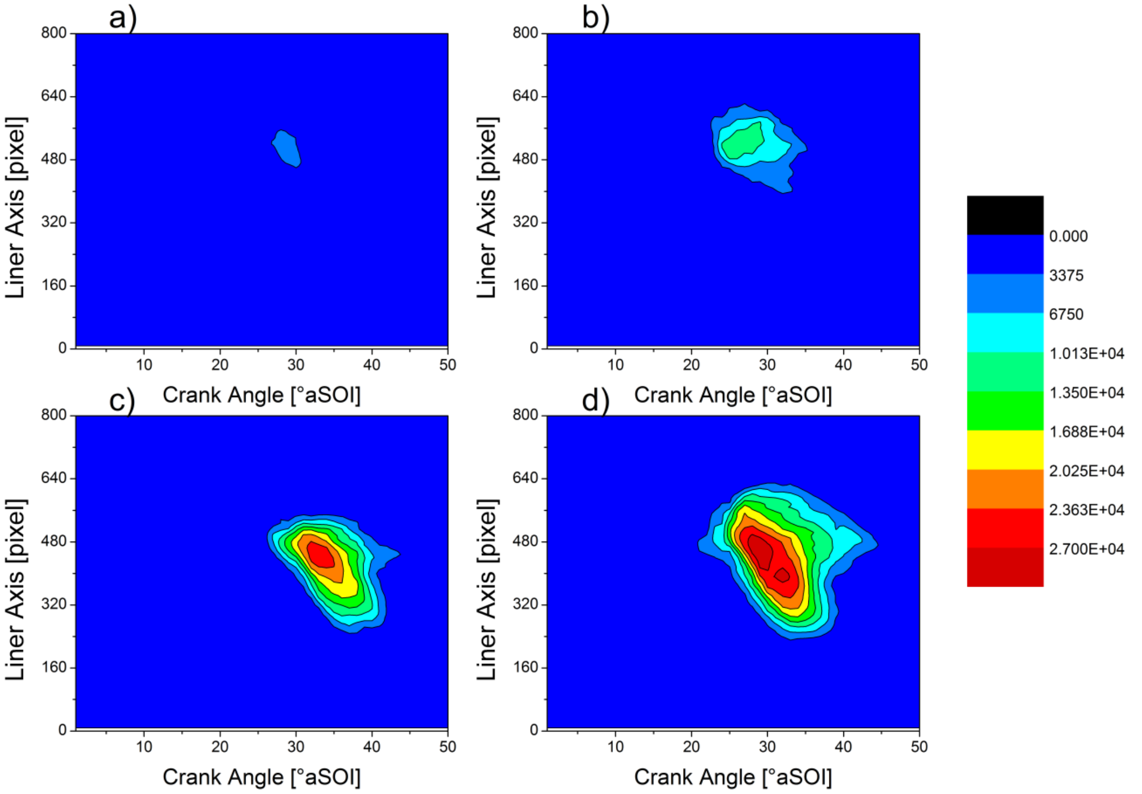

Figure 7-10. . Scattering signal intensity at the virtual boundary used to measure fuel flux to the combustion chamber wall as a function of crank angle after SOI.. a) E0-100 bar; b) E0-150 bar; c) E100-100 bar; d) E100-150 bar. Coolant temperature at 25° C and SOI = 250 °bTDC.

7.4 Conclusions

Spray development and fuel impingement with the cylinder wall were a strong function of the fuel type, coolant temperature and fuel rail pressure. The high speed imaging data were used to quantify the effects on the key spray features for E0, E50 and E100.

- E0 sprays exhibited higher sensitivity to coolant temperature compared to E100 in terms of spray cone angle and wall impingement, which is attributed to the effect of temperature on the volatile components of the fuel. Higher coolant temperature caused earlier spray collapse and narrower spray therefore less piston surface wetting. On the other hand the effect of higher temperature on reducing the viscosity of the fuel enhanced the spray rebound off the piston.
- The location of the spray impingement on the wall is related to fuel mixing and volatilization and spray collapse, which is sensitive to coolant temperature.
- The vaporization time after the EOI for E100 was not longer than the vaporization time for E0 despite the significantly higher enthalpy of vaporization of ethanol compared to gasoline.
- Higher fuel rail pressure decreased the injection duration, but the overall fuel vaporization remained constant for all fuels. The higher FRP also increased the spray tip penetration rate and fuel impingement with the wall, despite creating wider cone angles of the fuel sprays.

Chapter 8

Conclusions and Recommendations for Future Work

8.1 Conclusions

This thesis focused on understanding the impact of ethanol and ethanol/gasoline blends on advanced IC engine strategies and on understanding which of the fundamental properties of ethanol and ethanol blends control engine performance. The technical approach leveraged high speed imaging to study the fuel spray, combustion, ignition, and sooting (where appropriate) properties of the fuels using different optically accessible engine hardware, including HCCI and GDI configurations. The major findings of this research are listed below.

- Because of the kinetically controlled nature of HCCI, the high sensitivity of chemistry to temperature magnified the importance of the thermal effects of ethanol on charge preparation, and the chemical effects were not as significant at the conditions studied. The differences in charge cooling due to fuel vaporization and compression heating due to γ effects dominated the stability of HCCI operation at low load and low engine speed conditions. If not compensated, significantly higher enthalpy of vaporization and slightly lower γ of ethanol would decrease the end of compression temperatures and increase the ignition delay leading to less stable operation.

- SA-HCCI was successfully applied to expand the stability limits of low load and low engine speed conditions, but the technique is still dominated by autoignition, not spark-initiated flame propagation. The compression heating caused by flame propagation stabilized and accelerated autoignition of thermally preferred local sites, which affected the timing and stability of the global autoignition. The timing of SA was a tradeoff between the early initiation of flames at colder conditions with more time to propagate, but more risk of quenching, and the late initiation of flames at high temperatures with higher flame speeds, but less time to propagate. Wider flammability limits and higher flame speeds of ethanol resulted in improving the SA-HCCI performance and expanding the stable limit; however, the effects of ethanol were still dominated by thermal stratification, and not ethanol-specific chemistry even at SA-HCCI conditions

- Soot formation in DISI engines is highly dependent on the charge preparation. The in-cylinder soot formation was significantly correlated with conditions leading to high fuel impingement on the piston and combustion chamber surfaces. Therefore, PM formation was significantly reduced by conditions that reduced fuel impingement on the piston, e.g. later fuel injection timing for all the fuels. The in-cylinder trends were linked to engine-out emissions.

- Reduced PM formation using ethanol or ethanol blends was due to both ethanol combustion chemistry, which is intrinsically less likely to produce PM, and the spray characteristics of ethanol. E100 produced over an order of magnitude less soot (based on quantitative imaging metrics of soot thermal incandescence) at all operating conditions compared to E0. Spray cone angle, collapse and impingement changes in spray plumes were all dominated by the distillation properties of the gasoline-ethanol blends. Cases with narrower liquid spray resulted in less impingement with the piston and consecutively less soot. Higher levels of spray roll-up after the impingement enhanced the mixing and resulted in less liquid fuel on the piston and smaller pool fires. Sensitivity to enthalpy of vaporization of fuels was not observed for the DISI engine studies.

8.2 Recommendations for Future Work

This thesis focused on in-cylinder imaging studies of the combustion chamber to gain insight into the charge formation, flame initiation and propagation, combustion and thermal emission of soot in different engine operating modes. Temperature and charge stratification were identified as paramount characteristics controlling performance in the HCCI engine. Quantitative measurement of the stratification in the combustion chamber, would significantly improve the understanding of the cycle-to-cycle variation of autoignition as well as the instability of the spark initiate flame propagation during SA-HCCI.

The cycle-to-cycle variation in soot formation could not be related to the variation in spray features with the available diagnostic tools, although it is anticipated that the fuel spray plays a large role in the cycle-to-cycle dynamics. The high dependence of soot formation on piston impingement indicates that the formation of a fuel film on the piston yields locally high equivalence ratios and therefore the film properties are important to understanding and mitigating soot formation. Methods of analyzing the thickness of the fuel film on the piston, as well as the wetted area, would contribute significantly to the understanding of the overall and cycle-to-cycle soot emissions.

The effects of coolant temperature on the spray development and soot formation were described and demonstrated that soot formation can be eliminated by optimal fuel injection timing for a hot engine, but the practical problem for DISI engines remains at cold conditions. Efforts were made to measure/control the piston temperature (bottom surface temperature). Direct measurement of the engine component temperatures and spray temperature in the combustion chamber would result in better understanding of the vaporization of the fuels and formation of soot.

Bibliography

1. "International Energy Outlook: World Energy Demand and Economic Outlook," *U.S. Energy Information Administration*, 2013. http://www.eia.gov/forecasts/ieo/world.cfm.

2. W. Moomaw, F. Yamba, M. Kamimoto, L. Maurice, J. Nyboer, K. Urama, and T. Weir, *Renewable Energy Sources and Climate Change Mitigation: Special Report of the Intergovernmental Panel on Climate Change*. Cambridge, United Kingdom and New York, NY, USA: Cambridge University Press, 2011.

3. "Energy Improvement and Extension Act of 2008: Summary of Provisions," *U.S. Energy Information Association*, 2008. http://www.eia.gov/oiaf/aeo/otheranalysis/aeo_2009analysispapers/eiea.html.

4. "Energy Independence and Security Act of 2007," *U.S. Department of Energy*, 2007. http://www.afdc.energy.gov/afdc/laws/eisa.

5. "Energy Policy Act of 2005," *U.S. Department of Energy*, 2005. http://www.afdc.energy.gov/afdc/laws/epact_2005.

6. "2008 Farm Bill Side-By-Side," *U.S. Department of Agriculture*, 2008. http://www.ers.usda.gov/FarmBill/2008/Titles/TitleIXEnergy.htm.

7. “U.S. ethanol production and the Renewable Fuel Standard RIN bank,” *U.S. Energy Information Administration*, 2013. http://www.eia.gov/todayinenergy/detail.cfm?id=11551.

8. J. Hill, S. Polasky, E. Nelson, D. Tilman, H. Huo, L. Ludwig, J. Neumann, H. Zheng, and D. Bonta, “Climate change and health costs of air emissions from biofuels and gasoline.,” *Proc. Natl. Acad. Sci. U. S. A.*, vol. 106, no. 6, pp. 2077–82, Feb. 2009, doi: 10.1073/pnas.0812835106.

9. Ö. L. Gülder, “Burning Velocities of Ethanol-Isooctane Blends,” *Combust. Flame*, vol. 56, pp. 261–268, 1984, doi: http://dx.doi.org/10.1016/0010-2180(84)90060-9.

10. G. Broustail, P. Seers, F. Halter, G. Moréac, and C. Mounaim-Rousselle, “Experimental determination of laminar burning velocity for butanol and ethanol iso-octane blends,” *Fuel*, vol. 90, no. 1, pp. 1–6, Jan. 2011, doi: 10.1016/j.fuel.2010.09.021.

11. O. Röhl, S. Jerzembeck, J. Beeckmann, and N. Peters, “Numerical Investigation of Laminar Burning Velocities of High Octane Fuel Blends Containing Ethanol,” *SAE Tech. Pap.*, no. 2009–01–0935, 2009, doi: 10.4271/2009-01-0935.

12. J. A. Caton, “A Thermodynamic Evaluation of the Use of Alcohol Fuels in a Spark-Ignition Engine,” *SAE Int. J. Fuels Lubr.*, vol. 2, no. 2, pp. 1–19, 2009, doi: 10.4271/2009-01-2621.

13. J. P. Szybist, K. Chakravathy, and C. S. Daw, “Analysis of the Impact of Selected Fuel Thermochemical Properties,” *Energy & Fuels*, vol. 26, no. 5, pp. 2798–2810, 2012, doi: 10.1021/ef2019879.

14. K. Nakata, S. Utsumi, A. Ota, K. Kawatake, T. Kawai, and T. Tsunooka, “The Effect of Ethanol Fuel on a Spark Ignition Engine,” *SAE Tech. Pap.*, no. 2006–01–3380, 2006, doi: 10.4271/2006-01-3380.

15. A. A. Al-farayedhi, A. M. Al-Dawood, and P. Gandhidasan, “Effects of Blending Crude Ethanol with Unleaded Gasoline on Exhaust Emissions of SI Engine,” *SAE Tech. Pap.*, no. 2000–01–2857, 2000, doi: 10.4271/2000-01-2857.

16. R. H. Stanglmaier and C. E. Roberts, “Homogeneous Charge Compression Ignition (HCCI): Benefits , Compromises , and Future Engine Applications,” *SAE Tech. Pap.*, no. 1999–01–3682, 1999, doi: 10.4271/1999-01-3682.

17. K. Epping, S. Aceves, R. Bechtold, and J. E. Dec, “The Potential of HCCI Combustion for High Efficiency and Low Emissions,” *SAE Tech. Pap.*, no. 2002–01–1923, 2002, doi: 10.4271/2002-01-1923.

18. M. Christensen, B. Johansson, and P. Einewall, “Homogeneous Charge Compression Ignition (HCCI) Using Isooctane, Ethanol and Natural Gas - A Comparison with Spark Ignition Operation,” *SAE Tech. Pap.*, 1997, doi: 10.4271/972874.

19. T. Aroonsrisopon, V. Sohm, P. Werner, D. E. Foster, T. Morikawa, and M. Lida, “An Investigation Into the Effect of Fuel Composition on HCCI Combustion Characteristics,” *SAE Tech. Pap.*, no. 2002–01–2830, 2002, doi: 10.4271/2002-01-2830.

20. H. Liu, M. Yao, B. Zhang, and Z. Zheng, “Influence of Fuel and Operating Conditions on Combustion Characteristics of a Homogeneous Charge Compression Ignition Engine,” *Energy*, vol. 23, pp. 1422–1430, 2009, doi: 10.1021/ef800950c.

21. J. C. G. Andrae and R. a. Head, “HCCI experiments with gasoline surrogate fuels modeled by a semidetailed chemical kinetic model,” *Combust. Flame*, vol. 156, no. 4, pp. 842–851, Apr. 2009, doi: 10.1016/j.combustflame.2008.10.002.

22. V. H. Rapp, W. J. Cannella, J.-Y. Chen, and R. W. Dibble, “Predicting Fuel Performance for Future HCCI Engines,” *Combust. Sci. Technol.*, vol. 185, no. 5, pp. 735–748, May 2013, doi: 10.1080/00102202.2012.750309.

23. I. Truedsson, M. Tuner, B. Johansson, and W. Cannella, “Pressure Sensitivity of HCCI Auto-Ignition Temperature for Primary Reference Fuels,” *SAE Int. J. Engines*, vol. 5, no. 3, pp. 1089–1108, 2012, doi: 10.4271/2012-01-1128.

24. P. L. Kelly-zion and J. E. Dec, “A Computational Study of the Effect of Fuel Type on Ignition Time in Homogeneous Charge Compression Ignition Engines,” *Proc. Combust. Inst.*, vol. 28, pp. 1187–1194, 2000, doi: 10.1016/S0082-0784(00)80329-X.

25. M. Sjöberg and J. E. Dec, “Comparing late-cycle autoignition stability for single- and two-stage ignition fuels in HCCI engines,” *Proc. Combust. Inst.*, vol. 31, no. 2, pp. 2895–2902, Jan. 2007, doi: 10.1016/j.proci.2006.08.010.

26. Y. Zhang, B. He, H. Xie, and H. Zhao, “The Combustion and Emission Characteristics of Ethanol on a Port Fuel Injection HCCI Engine,” *SAE Tech. Pap.*, no. 2006–01–0631, 2006, doi: 10.4271/2006-01-0631.

27. G. Gnanam, A. Sobiesiak, G. Reader, and C. Zhang, “An HCCI Engine Fuelled with Iso-octane and Ethanol,” *SAE Tech. Pap.*, no. 2006–01–3246, 2006, doi: 10.4271/2006-01-3246.

28. H. Xie, Z. Wei, B. He, and H. Zhao, “Comparison of HCCI Combustion Respectively Fueled with Gasoline , Ethanol and Methanol through the Trapped Residual Gas Strategy,” *SAE Tech. Pap.*, no. 2006–01–0635, 2006, doi: 10.4271/2006-01-0635.

29. J. Hyvönen, G. Haraldsson, and B. Johansson, “Operating Conditions Using Spark Assisted HCCI Combustion During Combustion Mode Transfer to SI in a Multi-Cylinder VCR-HCCI Engine,” *SAE Tech. Pap.*, no. 2005–01–0109, 2005, doi: 10.4271/2005-01-0109.

30. A. Berntsson and I. Denbratt, “Spark Assisted HCCI Combustion Using a Stratified Spark Assisted HCCI Combustion Using a Stratified Hydrogen,” *SAE Tech. Pap.*, no. 2005–24–039, 2005, doi: 10.4271/2005-24-039.

31. M. Weinrotter, E. Wintner, K. Iskara, T. Neger, J. Olofsson, H. Seyfried, M. Aldén, M. Lackner, F. Winter, A. Vressner, A. Hultqvist, and B. Johansson, “Optical Diagnostics of Laser-Induced and Spark Plug-Assisted HCCI Combustion,” *SAE Tech. Pap.*, no. 2005–01–0129, 2005, doi: 10.4271/2005-01-0129.

32. B. T. Zigler, P. E. Keros, K. B. Helleberg, M. Fatouraie, D. Assanis, and M. S. Wooldridge, “An experimental investigation of the sensitivity of the ignition and combustion properties of a single-cylinder research engine to spark-assisted HCCI,” *Int. J. Engine Res.*, vol. 12, no. 4, pp. 353–375, Aug. 2011, doi: 10.1177/1468087410401286.

33. A. W. Berntsson and I. Denbratt, “Optical study of HCCI Combustion using NVO and an SI Stratified Charge Optical study of HCCI Combustion using NVO and an SI Stratified Charge,” *SAE Tech. Pap.*, no. 2007–14–0012, 2007, doi: 10.4271/2007-24-0012.

34. P. G. Aleiferis, A. G. Charalambides, Y. Hardalupas, and A. M. K. P. Taylor, “Autoignition Initiation and Development of n-heptane HCCI Combustion Assisted by Inlet Air Heating , Internal EGR or Spark Discharge : An Optical Investigation,” *SAE Tech. Pap.*, no. 2006–01–3273, 2006, doi: 10.4271/2006-01-3273.

35. B. T. Zigler, “An experimental investigation of the ignition properties of low temperature combustion in an optical engine by,” University of Michigan, 2008.

36. B. T. Zigler, S. M. Walton, D. Assanis, E. Perez, M. S. Wooldridge, and S. T. Wooldridge, “An Imaging Study of Compression Ignition Phenomena of Iso-Octane, Indolene, and Gasoline Fuels in a Single-Cylinder Research Engine,” *J. Eng. Gas Turbines Power*, vol. 130, no. 5, pp. 052803–052803–11, 2008, doi: 10.1115/1.2898720.

37. B. T. Zigler, S. M. Walton, D. M. Karwat, D. Assanis, M. S. Wooldridge, and S. T. Wooldridge, “A Multi-Axis Imaging Study Of Spark-Assisted Homogeneous Charge Compression Ignition Phenomena In A Single-Cylinder Research Engine,” in *ASME I.C. Engine*, 2007.

38. S. Zhang and W. McMahon, “Particulate Emissions for LEV II Light-Duty Gasoline Direct Injection Vehicles,” *SAE Int. J. Fuels Lubr.*, vol. 5, no. 2, pp. 637–646, Apr. 2012, doi: 10.4271/2012-01-0442.

39. N. Fraser, H. Blaxill, G. Lumsden, and M. Bassett, “Challenges for Increased Efficiency through Gasoline Engine Downsizing,” *SAE Int. J. Engines*, vol. 2, no. 2009–01–1053, pp. 991–1008, 2008, doi: 10.4271/2009-01-1053.

40. P. Ericsson, M. Holmström, A. Amberntsson-carlsson, C. Ohlson, M. Skoglundh, B. Andersson, and P. Carlsson, “Characterization of

Particulate Emissions and Methodology for Oxidation of Particulates from Non-Diesel Combustion Systems," *SAE Tech. Pap.*, no. 2008–01–1746, 2008, doi: 10.4271/2008-01-1746.

41. P. Price, R. Stone, T. Collier, and M. Davies, "Particulate Matter and Hydrocarbon Emissions Measurements : Comparing First and Second Generation DISI with PFI in Single Cylinder Optical Engines," *SAE Tech. Pap.*, no. 2006–01–1263, 2006, doi: 10.4271/2006-01-1263.

42. M. Braisher, R. Stone, and P. Price, "Particle Number Emissions from a Range of European Vehicles," *SAE Tech. Pap.*, no. 2010–01–0786, 2010, doi: 10.4271/2010-01-0786.

43. S. Hemdal, M. Andersson, P. Dahlander, R. Ochoterena, and I. Denbratt, "In-cylinder soot imaging and emissions of stratified combustion in a spark-ignited spray-guided direct-injection gasoline engine," *Int. J. Engine Res.*, vol. 12, no. 6, pp. 549–563, Sep. 2011, doi: 10.1177/1468087411418167.

44. T. Kasper, P. Oswald, M. Kamphus, and K. Kohsehoinghaus, "Ethanol flame structure investigated by molecular beam mass spectrometry," *Combust. Flame*, vol. 150, no. 3, pp. 220–231, Aug. 2007, doi: 10.1016/j.combustflame.2006.12.022.

45. E. J. Barrientos, M. Lapuerta, and A. L. Boehman, "Group additivity in soot formation for the example of C-5 oxygenated hydrocarbon fuels," *Combust. Flame*, pp. 1–15, Mar. 2013, doi: 10.1016/j.combustflame.2013.02.024.

46. D. C. Rakopoulos, C. D. Rakopoulos, E. C. Kakaras, and E. G. Giakoumis, "Effects of ethanol–diesel fuel blends on the performance and exhaust emissions of heavy duty DI diesel engine," *Energy Convers.*

Manag., vol. 49, no. 11, pp. 3155–3162, Nov. 2008, doi: 10.1016/j.enconman.2008.05.023.

47. H. Kim and B. Choi, “Effect of ethanol–diesel blend fuels on emission and particle size distribution in a common-rail direct injection diesel engine with warm-up catalytic converter,” *Renew. Energy*, vol. 33, no. 10, pp. 2222–2228, Oct. 2008, doi: 10.1016/j.renene.2008.01.002.

48. L. Chen, R. Stone, and D. Richardson, “A study of mixture preparation and PM emissions using a direct injection engine fuelled with stoichiometric gasoline / ethanol blends,” *Fuel*, vol. 96, pp. 120–130, 2012, doi: 10.1016/j.fuel.2011.12.070.

49. L. De Francqueville, “Effects of Ethanol Addition in RON 95 Gasoline on GDI Stratified Combustion,” *SAE Tech. Pap.*, no. 2011–24–0055, 2011, doi: 10.4271/2011-24-0055.

50. J. M. Storey, T. Barone, K. Norman, and S. Lewis, “Ethanol Blend Effects On Direct Injection Spark- Ignition Gasoline Vehicle Particulate Matter Emissions,” *SAE Tech. Pap.*, no. 2010–01–2129, 2010, doi: 10.4271/2010-01-2129.

51. X. He, J. C. Ireland, B. T. Zigler, M. A. Ratcliff, K. E. Knoll, T. L. Alleman, and J. T. Tester, “The Impacts of Mid-level Biofuel Content in Gasoline on SIDI Engine-out and Tailpipe Particulate Matter Emissions,” *SAE Tech. Pap.*, no. 2010–01–2125, 2010, doi: 10.4271/2010-01-2125.

52. X. He, M. a. Ratcliff, and B. T. Zigler, “Effects of Gasoline Direct Injection Engine Operating Parameters on Particle Number Emissions,” *Energy & Fuels*, p. 120313094034009, Mar. 2012, doi: 10.1021/ef201917p.

53. S. H. Park, H. J. Kim, H. K. Suh, and C. S. Lee, "Atomization and spray characteristics of bioethanol and bioethanol blended gasoline fuel injected through a direct injection gasoline injector," *Int. J. Heat Fluid Flow*, vol. 30, no. 6, pp. 1183–1192, Dec. 2009, doi: 10.1016/j.ijheatfluidflow.2009.07.002.

54. V. F. Andersen, J. E. Anderson, T. J. Wallington, S. a. Mueller, and O. J. Nielsen, "Distillation Curves for Alcohol−Gasoline Blends," *Energy & Fuels*, vol. 24, no. 4, pp. 2683–2691, Apr. 2010, doi: 10.1021/ef9014795.

55. R. L. Furey and K. L. Perry, "Vapor Pressures of Mixtures of Gasolines and Gasoline-Alcohol Blends," *SAE Tech. Pap.*, no. 861557, 1986, doi: 10.4271/861557.

56. P. G. Aleiferis, D. Richardson, and S. Wallace, "Characteristics of Ethanol , Butanol , Iso-Octane and Gasoline Sprays and Combustion from a Multi-Hole Injector in a DISI Engine," *SAE Tech. Pap.*, no. 2008–01–1591, 2008, doi: 10.4271/2008-01-1591.

57. M. Fatouraie, M. Wooldridge, and S. Wooldridge, "In-Cylinder Particulate Matter and Spray Imaging of Ethanol / Gasoline Blends in a Direct Injection Spark Ignition Engine," *SAE Int. J. Fuels Lubr.*, vol. 6, no. 1, pp. 1–10, 2013, doi: 10.4271/2013-01-0259.

58. E. Stevens and R. Steeper, "Piston Wetting in an Optical DISI Engine : Fuel Films , Pool Fires , and Soot Generation," *SAE Tech. Pap.*, no. 2001–01–1203, 2001, doi: 10.4271/2001-01-1203.

59. T. L. Barone, J. M. E. Storey, A. D. Youngquist, and J. P. Szybist, "An analysis of direct-injection spark-ignition (DISI) soot morphology," *Atmos. Environ.*, vol. 49, pp. 268–274, Mar. 2011, doi: 10.1016/j.atmosenv.2011.11.047.

60. AVL, “Smoke Value Measurements with the Filter-Paper-Method,” Graz, Austria, 2005.

61. R. R. Steeper and E. J. Stevens, “Characterization of Combustion , Piston Temperatures , Fuel Sprays , and Fuel- Air Mixing in a DISI Optical Engine,” *SAE Tech. Pap.*, no. 2000–01–2900, 2000, doi: 10.4271/2000-01-2900.

62. M. Fatouraie, P. Keros, and M. Wooldridge, “A Comparative Study of the Ignition and Combustion Properties of Ethanol-Indolene Blends During HCCI Operation of a Single Cylinder Engine,” *SAE Tech. Pap.*, no. 2012–01–1124, 2012, doi: 10.4271/2012-01-1124.

63. K. Chang, A. Babajimopoulos, G. A. Lavoie, Z. S. Filipi, and D. N. Assanis, “Analysis of Load and Speed Transitions in an HCCI Engine Using 1-D Cycle Simulation and Thermal Networks,” *SAE Tech. Pap.*, no. 2006–01–1087, 2006, doi: 10.4271/2006-01-1087.

64. E. Kasseris and J. Heywood, “Charge Cooling Effects on Knock Limits in SI DI Engines Using Gasoline / Ethanol Blends : Part 2-Effective Octane Numbers,” *SAE Int. J. Fuels Lubr.*, vol. 5, no. 2, pp. 844–854, 2012, doi: 10.4271/2012-01-1284.

65. R. A. Stein, D. Polovina, K. Roth, M. Foster, M. Lynskey, T. Whiting, J. E. Anderson, M. H. Shelby, T. G. Leone, and S. Vandergriend, “Effect of Heat of Vaporization , Chemical Octane , and Sensitivity on Knock Limit for Ethanol - Gasoline Blends,” *SAE Int. J. Fuels Lubr.*, vol. 5, no. 2012–01–1277, pp. 823–843, 2012, doi: 10.4271/2012-01-1277.

66. M. Fatouraie and M. S. Wooldridge, “Optical Investigation of the Effects of Ethanol/Gasoline Blends on Spark-Assisted HCCI,” in *ASME*

2013 Internal Combustion Engine Division Fall Technical Conference, 2013, pp. 1–18.

67. M. G. Zabetakis, "Flammability characteristics of combustible gases and vapors," US Dept. of the Interiror, Bureau of Mines, 1965.

68. A. G. Gaydon, *The Spectroscopy of Flames*, First. New York: John Wiley & Sons Inc., 1957.

69. P. Keros, "Emissions and imaging studies of spark assisted HCCI," University of Michigan, 2011.

70. P. E. Keros, D. Assanis, J. Schlechtweg, and M. S. Wooldridge, "Fast Methods to Analyze High-Speed Images of HCCI and Spark-Assisted HCCI Ignition Events," *ASME 2010 Intern. Combust. Engine Div. Fall Tech. Conf.*, pp. 441–455, 2010, doi: 10.1115/ICEF2010-35143.

71. L. Manofsky, D. Assanis, and A. Babajimopoulos, "Bridging the Gap between HCCI and SI : Spark- Assisted Compression Ignition," *SAE Tech. Pap.*, no. 2011–01–1179, 2011, doi: 10.4271/2011-01-1179.

72. L. R. Cancino, M. Fikri, A. a. M. Oliveira, and C. Schulz, "Ignition delay times of ethanol-containing multi-component gasoline surrogates: Shock-tube experiments and detailed modeling," *Fuel*, vol. 90, no. 3, pp. 1238–1244, Mar. 2011, doi: 10.1016/j.fuel.2010.11.003.

73. M. Sjoberg and J. E. Dec, "Ethanol Autoignition Characteristics and HCCI Performance for Wide Ranges of Engine Speed , Load and Boost," *SAE Int. J. Engines*, vol. 3, no. 1, pp. 84–106, 2010, doi: 10.4271/2010-01-0338.

74. K. Kar, T. Last, C. Haywood, and R. Raine, “Measurement of Vapor Pressures and Enthalpies of Vaporization of Gasoline and Ethanol Blends and Their Effects on Mixture Preparation in an SI Engine,” *SAE Tech. Pap.*, no. 2008–01–0317, 2008, doi: 10.4271/2008-01-0317.

75. S. Malaguti, S. Fontanesi, and E. Severi, “Numerical Analysis of GDI Engine Cold-Start at Low Ambient Temperatures,” *SAE Tech. Pap.*, no. 2010–01–2123, 2010, doi: 10.4271/2010-01-2123.

76. R. Lindgren and I. Denbratt, “Modelling Gasoline Spray-wall Interaction - A Review of Current Models,” *SAE Tech. Pap.*, no. 2000–01–2808, 2000, doi: 10.4271/2000-01-2808.

77. F. Ullmann, *Ullmann’s Chemical Engineering and Plant Design*. John Wiley & Sons Inc., 2005, p. 576.

78. J. Dernotte, C. Hespel, F. Foucher, S. Houillé, and C. Mounaïm-Rousselle, “Influence of physical fuel properties on the injection rate in a Diesel injector,” *Fuel*, vol. 96, pp. 153–160, Jun. 2012, doi: 10.1016/j.fuel.2011.11.073.

79. P. G. Aleiferis, J. Serras-Pereira, a. Augoye, T. J. Davies, R. F. Cracknell, and D. Richardson, “Effect of fuel temperature on in-nozzle cavitation and spray formation of liquid hydrocarbons and alcohols from a real-size optical injector for direct-injection spark-ignition engines,” *Int. J. Heat Mass Transf.*, vol. 53, no. 21–22, pp. 4588–4606, Oct. 2010, doi: 10.1016/j.ijheatmasstransfer.2010.06.033.